Scanning Tunneling Microscopy in Micromechanics Investigations

Thesis by

Guillaume Vendroux

In Partial Fulfillment of the Requirements

for the Degree of

Doctor of Philosophy

California Institute of Technology

Pasadena, California

1994

(Submitted December 16, 1993)

A mes parents.

Acknowlegdgments

I would like to thank the National Science Foundation for providing the funds to construct the Scanning Tunneling Microscope under grant MSS 9109973. Also, additional assistance through the Office of Naval Research under contract N00014-91-5-1427 with Dr. Peter Schmidt as the technical monitor is gratefully acknowledged.

I must offer special thanks to Motorola for the generous donations of electronic equipment.

This project could not have carried out without the precious help of the Galcit machine shop staff, Joe Haggerty, Phil Wood and Larry Frazier , thanks to all of you.

I would also like to thank my friends and collegues Hugh Bruck, John Lambros Mark Walter and Dr Guillermo Pulos for many helpful and enlightening discussions.

Finally, I would like to thank my advisor Professor Knauss for his trust and patience. I am deeply grateful for the opportunity he gave me to spend these years at GALCIT.

Abstract

A new experimental method is proposed for studying deformations of micromechanical material systems at the submicron scale. To that end, a Scanning Tunneling Microscope (STM) was designed and built to allow placement on a mechanically deforming specimen. Operating in constant current mode, this digitally controlled STM records detailed topographies of specimen surfaces with a resolution of 10.15 nm in-plane and 6.6×10^{-2} nm out-of-plane, over a 10 $\mu m \times 10$ μm area.

A pattern recognition type algorithm was written to extract the 3-D displacement field from topographies of a given specimen area but under different loading conditions. This Digital Image Correlation (DIC) scheme was found to have very robust convergence characteristics and a higher resolution than that of the images it compares. The accuracy of the DIC code on STM scans was assessed by measuring displacement fields resulting from a translation of the specimen under the microscope. Two major causes of noise were identified, namely drifting of the specimen during scan acquisition and hysteresis distortion of the scan grid. An experimental procedure was devised to limit the occurrence of such perturbations and under these guidelines the resolution of the DIC scheme was found to be 4.8 nm for in-plane displacement measurements and 1.5 nm for out-of-plane's.

A micromechanical study of the deformation mechanism of PolyVinylChloride (PVC) was undertaken. Analysis of STM scans revealed that, upon first loading the surface of PVC specimens is deformed irreversibly even at low strain levels. The size of the strain induced topographic changes suggests that, at the scale of 0.1 μm, a continuum type constitutive modeling of PVC may not be appropriate. This investigation also uncovered the present limitations of the STM-DIC scheme in measuring displacement fields consistently at the nanometer scale.

Table of Contents

List of Figures

Introduction

During the past decade, a new discipline known as "mechanics of material" has evolved which adresses material-related problems from a viewpoint of (continuum) mechanics. One class of problems under this topic which is very important deals with interfaces and their mechanical response under load. These problems arise typically in adhesion science and adhesive bonding as exemplified by structural bonds, by fiber-matrix interaction in composite materials and by the joining of small components in electronic devices, to name a few.

Common to these applications or areas of investigation is the structural integrity of interfaces under load, where the latter may be derived from a need to transmit loads across an interface (adhesive bonding and composites) or be the result of residual or thermally induced stresses, as in the case of electronic devices. From a (continuum) mechanics point of view, it is of interest to develop criteria for interfacial failure, which task requires a knowledge of properties of the materials bordering on the interface. It is common practice that mechanics analyses are conducted under the assumption that the interface is a sharply defined plane or surface which separates two solids of distinctly different properties. In fact it is recognized that there should be a very thin region, possibly measured in tens or hundreds of nanometers, within which the properties vary as one approaches an interface. Such a domain is often referred to as an interphase.

It is established that whenever machanics provides a theoretical basis for failure analysis or prediction of an interface, that analysis should account for the variable properties in the interphase region; otherwise the true physical characteristics of the bonds

can neither be assessed, *e.g.*, in a laboratory environment, nor should one expect that a truly valid theory can be constructed which ignores the surface-near variation of physical properties.

While these concepts and current limitations of failure analyses for interphases are widely accepted, and the need for detailed characterization of the materials at appropriately small size scale are desired, it is less clear how to provide the requisite experimental methods and techniques to determine either the properties such as (anisotropic) stiffness or "interphase strength," or even the size scale at which such property variations occur and/or at which level continuum concepts need to be seriously questioned.

The traditional experimental solution addressing this need for micromechanical investigations is twofold. On the one hand, qualitative and *post-mortem* observations are performed through high magnification microscopes, usually SEM or TEM while, on the other hand, experiments are devised which would reflect macroscopically the effect of a theorized submicron phenomenon or behavior. Only very rarely is it possible to undertake direct quantitative micromechanical studies at the nanometer scale which in many cases could bring a definitive answer to a problem at hand.

In the early eighties, a new kind of microscope was introduced, the Scanning Tunneling Microscope (STM). Based on the quantum tunneling effect, STMs record surface topographies with a spatial resolution ranging from an unprecedented 0.01Å to tens or even hundreds of nanometers. During the same time period, pattern recognition type algorithms were proposed to measure in-plane displacement fields from digital photographs of specimens being deformed. If this latter method could be modified to accommodate three-dimensional topographies rather than two-dimensional images and to compute three-dimensional displacement fields rather than two-dimensional ones, then the combination of STM and Digital Image Correlation would allow for a new style of systematic mechanical investigations at a very small scale. The main objective of this thesis is,

therefore, to investigate how well STMs are suited for micromechanical studies and in particular, how accurately three-dimensional displacement fields can be extracted from the comparison between surface topographies before and after *in-situ* deformation.

Because STMs are usually dedicated to the studies of the surface structure of small samples rather than the measurement of displacement fields over minute areas of large specimens, it was necessary to design and built the apparatus in accordance with the specific requirements for such micromechanical investigations. Since the ultimate goal of this research is to perform qualitative as well as quantitative observations, a thorough calibration and error assessment of the STM needed to be undertaken. The displacement measurement capabilities of this system were provided by a custom Digital Image Correlation (DIC) code tailored so as to accommodate surface topographies and extract not only the in-plane displacement components but those for out-of-plane motion as well. The performance of the scheme was evaluated by employing Digital Image Correlation on STM scans reflecting a simple translation of the specimen under the microscope. Finally, and as a first test case, the deformation of PolyVinylChloride at the micron and submicron scale was investigated.

This dissertation is divided into six chapters. Chapter 1 describes the various building blocks of the STM. The calibration of the apparatus as well as the error assessment of the topographic records are presented in chapter 2. Chapter 3 focuses on the Digital Image Correlation code while chapter 4 evaluates, through translation experiments, the resolution of the STM-DIC scheme in full field displacement measurements. Chapter 5 is dedicated to the micromechanical investigation of PolyVinylChloride under tensile loading.

CHAPTER 1

Scanning Tunneling Microscope

1.1 Working Principle

Scanning Tunneling Microscopy is based on the tunneling of electrons between an electrically charged surface and a conductive tip. This phenomenon, known since the introduction of quantum mechanics in the 1920's,[1] has been first applied successfully by Binnig *et al.*[2-4] to measure surface topographies with atomistic resolution. If a sharp conductive probe is brought very close to a conductive surface (see Figure 1.1) and given a voltage bias between the tip and the specimen, electrons will jump across the potential barrier from one conductor to the other depending on the sign of the potential difference. Using the approximation of one-dimensional planar tunneling to describe this phenomenon,[5] the current I_t resulting from tunneling electrons (the tunneling current) can be written as

$$I_t = \frac{c}{d^2}\{(\overline{\phi}-\frac{eV_b}{2})exp[-A(\overline{\phi}-\frac{eV_b}{2})^{\frac{1}{2}}]-(\overline{\phi}+\frac{eV_b}{2})exp[-A(\overline{\phi}+\frac{eV_b}{2})^{\frac{1}{2}}]\}, \quad (1.1.1)$$

where

$A = 1.025\,(eV)^{-\frac{1}{2}}\text{Å}^{-1}$,

$\overline{\phi}$ = average of the barrier height between the two electrodes,

V_b = bias voltage,

c = positive constant,

d = gap distance.

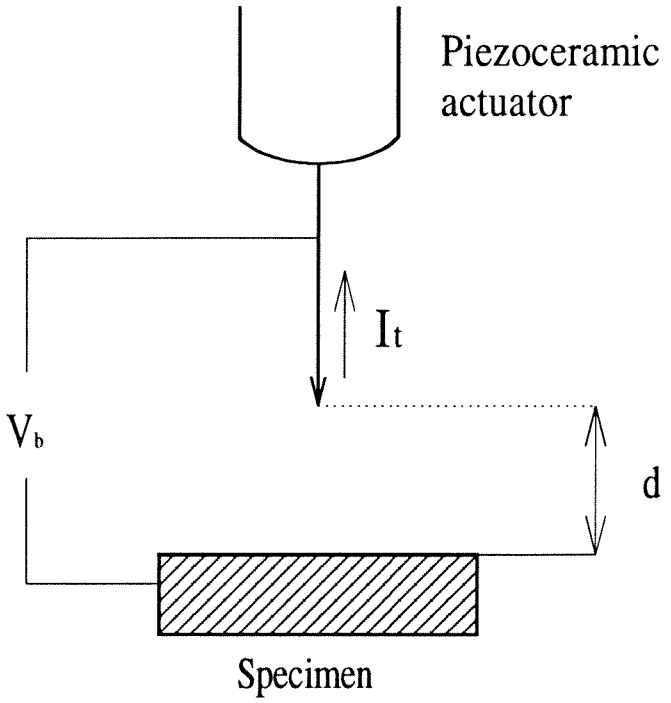

FIGURE 1.1 STM Working Principle.

When the gap distance d as well as the bias voltage V_b are small, equation (1.1.1) can be rewritten as

$$I_t \propto \frac{V_b}{d} exp\left[-A\bar{\phi}^{\frac{1}{2}} d\right]. \tag{1.1.2}$$

For a typical gap distance of 1 nm and a bias Voltage of 0.1 V, the resulting tunneling current I_t is on the order of 1 nA.

Because of relation (1.1.2) between I_t and d, a direct measurement of the tunneling current would yield the gap distance only through a very delicate calibration which would depend on the tip and specimen surface constitutive materials. This calibration can be avoided by setting up a feedback loop over I_t. Controlling the position of the tip with respect to the sample by a high accuracy actuator, a steady-state set point I_0 is defined for the tunneling current : if $I_t < I_0$ the actuator brings the probe closer to the specimen surface and inversely if $I_t > I_0$. The set point I_0 actually corresponds to a set gap distance, say d_0. The amount of correction required from the actuator to reach d_0 at two different locations over the specimen surface is then a direct measurement of the height

difference between these two points as illustrated in Figure 1.2.

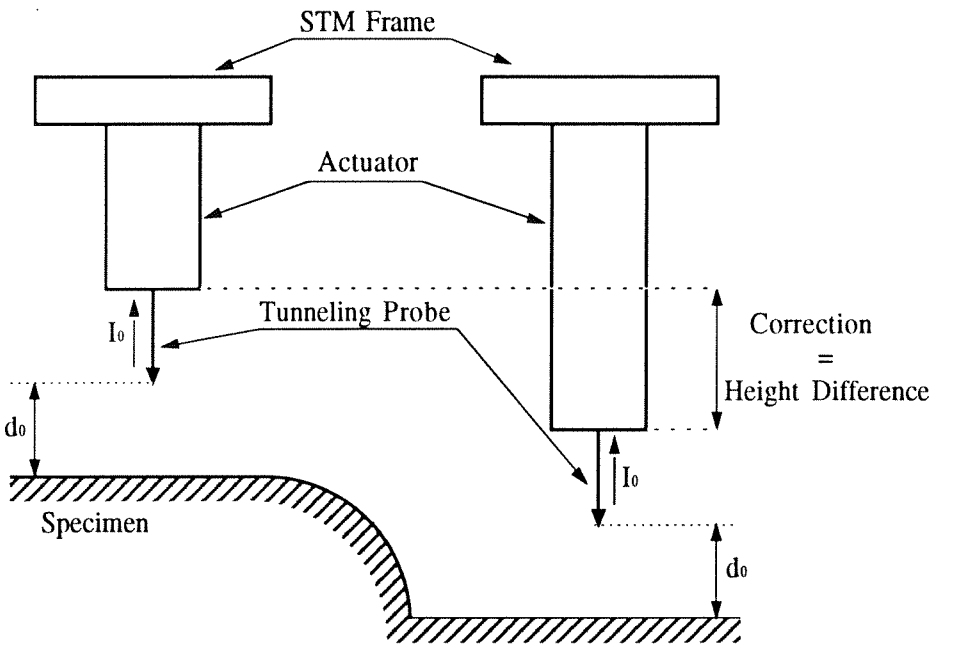

FIGURE 1.2 Height Measurement in STM Feedback Loop Mode.

Figure 1.3 shows a schematic diagram of the Scanning Tunneling Microscope (STM) which was designed and build for this project. The tunneling current is sensed via a current-to-voltage converter, digitized on 12 bits and acquired by a Digital Signal Processing board (DSP board). This board then computes the correction required to bring I_t to the pre-selected set point I_0, outputs it through a 16 bit Digital-to-Analog converter and high voltage amplifier to a piezoceramic actuator which contracts or expands under the given signal, therefore regulating the gap distance. During data acquisition, a Personal Computer (PC) controls the in-plane position of the tip and moves it over predetermined grid points. At each of these points, the DSP dumps the height correction data to the PC screen which displays it as colored pixel, every discrete color corresponding to a different elevation.

Extensive literature exists about all the design considerations for STMs[6-12] and it is beyond the scope of this work to detail them all. The next sections present and describe

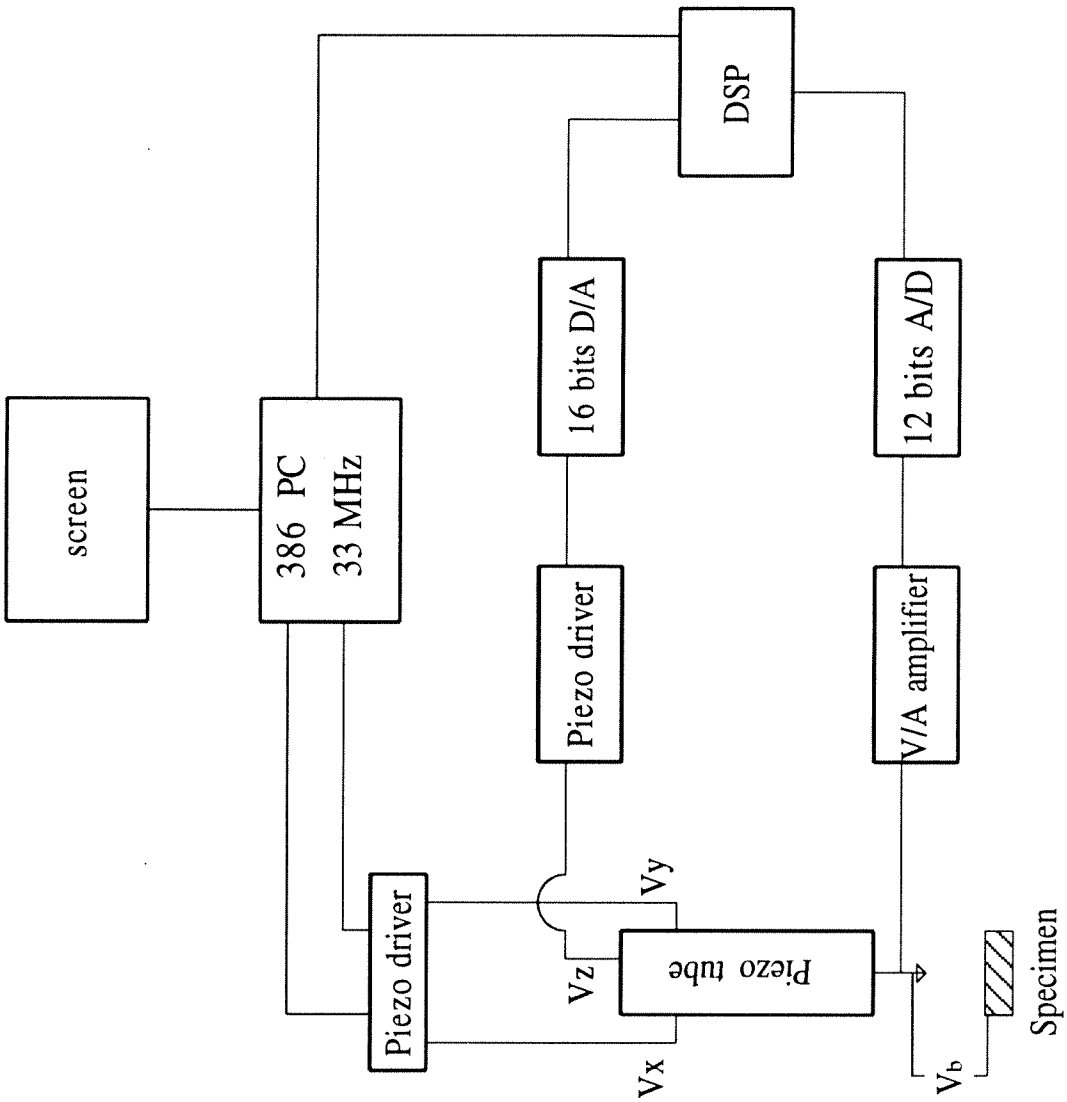

FIGURE 1.3 STM Architecture.

only the criterion and design constraints relevant to this specific apparatus as well as its final drafts, electronic schematics and computer softwares.

1.2 STM Hardware

The various components constituting the microscope can be classified into four categories. The first involves the devices responsible for the motion of the STM tip along the three axes. The second set includes the different electronic circuits required to establish the feedback loop for the tunneling current. The third category comprises what is necessary to acquire and store an STM scan. Finally the fourth group contains the mechanical parts of the microscope. The following sections describe in detail the various elements in each of these categories. In addition, the design of the loadframe which fits under the STM is presented.

1.2.1 Piezoceramic Actuator

The key to Scanning Tunneling Microscopy is the control of the position of the tip with respect to the specimen surface. To that purpose, one needs a highly accurate actuator that can move the tunneling probe along the three axes as defined in Figure 1.4.

Along the Z axis, the gap distance is on the order of 1 nm. Consequently the resolution of the actuator over the vertical axis was chosen to be around 10^{-2} nm so as to regulate the tunneling distance to within 1%. In the X-Y plane, the relevant size scale of the mechanical systems which will be under investigation is approximately 1 μm. To capture such features accurately, the minimum spacing between measurement points was chosen to be 10 nm.

In addition to the fine resolution, the actuator should respond linearly with respect to its input signal (voltage), so that the position of the tunneling tip in space can be easily deduced. Finally the whole assembly should be stiff enough not to let vibrations affect the gap distance.

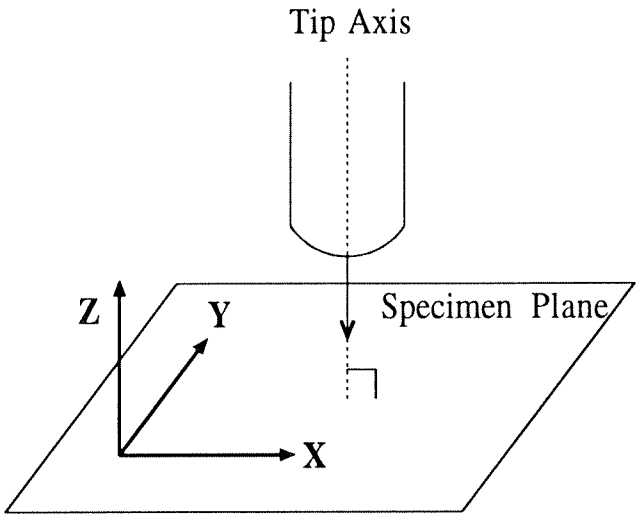

FIGURE 1.4 STM Axis System.

The common solution to this engineering problem resides in piezoelectric or piezoceramic actuators. Such materials have the properties to expand or contract when subjected to an electric field, with a sensitivity of a few nanometers per volts. There exist many different designs for such devices but the stiffer and more compact of these is the tube scanner[7] presented in Figure 1.5. It consists of a hollow piezoceramic tube coated with Nickel so as to provide four separate quadrant electrodes on the outside surface of the tube and one continuous electrode on the inside surface of the tube. A potential difference V between the outside and inside electrodes will contract or expand the whole tube along its axis, thus providing the degree of freedom in the Z direction. Biasing one quadrant electrode to a voltage V, its opposite to $-V$ and grounding all other electrodes will cause one of the tube quadrants to expand while its opposite contracts. That will, in effect, bend the tube and move the centerline of the actuator in-plane. The resulting X-Y motion is not entirely orthogonal to the Z axis but coupling is small as will be assessed during calibration (chapter 2).

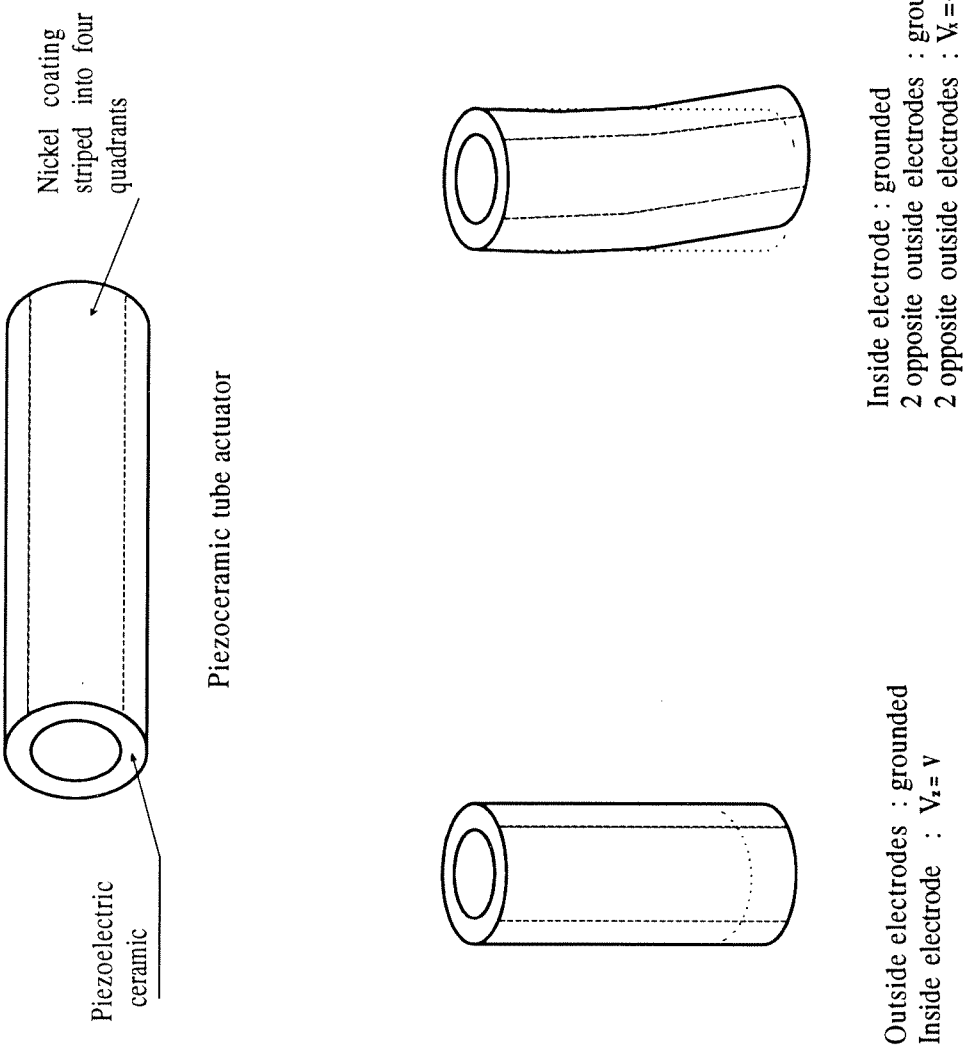

FIGURE 1.5 Piezoceramic Actuator.

Mathematically, this behavior can be expressed as follows; the motion in the Z direction is described by[13]

$$\Delta Z = 2d_{31}V\frac{L}{(OD - ID)} , \tag{1.2.1}$$

where

L = Length of the tube,

OD = Outside diameter of the tube,

ID = Inside diameter of the tube,

V = Voltage applied to the Z electrode,

d_{31} = Piezo-electric charge constant ($\approx 250 \times 10^{-12}\ m/V$).

The X-Y motion of the tube centerline as a function of applied voltage can be approximated from beam theory as

$$\left.\begin{matrix}\Delta X \\ \Delta Y\end{matrix}\right\} = 4d_{31}V\frac{L^2}{OD(OD - ID)} . \tag{1.2.2}$$

The specific application contemplated here requires a "wide" scan area so as to be able to image "large" micromechanical systems, *i.e.*, $\Delta X, \Delta Y \approx 50\ \mu m$, as well as an out-of-plane range on the order of 1 μm. To simplify the design of the electronics controlling the tube, these ranges of motion should be attained for a reasonably small input voltage ($\approx 200\ V$). Considering equations (1.2.1) and (1.2.2), these requirements command the length of the tube L to be maximized while keeping OD and ID small with d_{31} as large as possible. These criteria together with manufacturing limitations determined the final dimensions of the piezoceramic tube as

- Material : Lead Zirconate Titanate (EBL3, Staveley Sensor[14]),
- $d_{31} \approx 250 \times 10^{-12}\ m/V$,
- Length : $L = 2$",
- Outside diameter : $OD = 0.5$",

- Inside diameter : $ID = 0.44$".

1.2.2 Feedback Loop

As described previously, the whole concept of STM operation revolves around the feedback loop which maintains the tunneling current, and thus the gap distance, constant. The following sections describe the various electronic components which are part of this regulating loop, namely, the current-to-voltage converter which transforms the tunneling current to a "tunneling" voltage, the 12 bit Analog-to-Digital converter sensing the tunneling voltage, the Digital Signal Processing board (DSP Board) computing the feedback loop correction, the 16 bit Digital-to-Analog converter translating that correction into a voltage signal and finally the voltage amplifier that provides the tube with the excitation signal, therefore regulating the loop.

a. *Current-to-Voltage Converter*

A current-to-voltage converter is used to sense the current resulting from the electron tunneling phenomena. The design opted for the measurement of I_t at the tip rather than on the specimen surface. Consequently, a positive bias voltage, $\Delta V = V_{spec.} - V_{tip} > 0$, yields a positive tunneling current in the tip. [a] The role of the current-to-voltage converter is to transform the tunneling current into a "tunneling" voltage. Several electronic designs exist for such purposes. The simpler and more compact circuit was chosen in order to physically locate the detector as close as possible to the tip; the signal being so small, long wiring would increase noise pick-up. The elected design contains only one component as shown in Figure 1.6 and its working equation is

$$V = -RI_t \ , \tag{1.2.3}$$

[a] The sign convention for the current is such that a current is positive when flowing from high to low potentials whereas electrons go from low to high potentials.

where

V = Output Voltage,

I_t = Tunneling Current,

R = Feedback Resistor (1% Metal Film $100 \times 10^6 \Omega$).

The operational amplifier in this circuit, OPA128 from Burr Brown,[15] was picked for its very low bias current ($< \ 10^{-15} \ A$) and its good frequency response. The input as well as the output leads are isolated and the whole detector is sealed in a small grounded aluminium box. Since the set point for the tunneling current is approximately 1 nm, the output voltage is centered around $-0.1 \ V$.

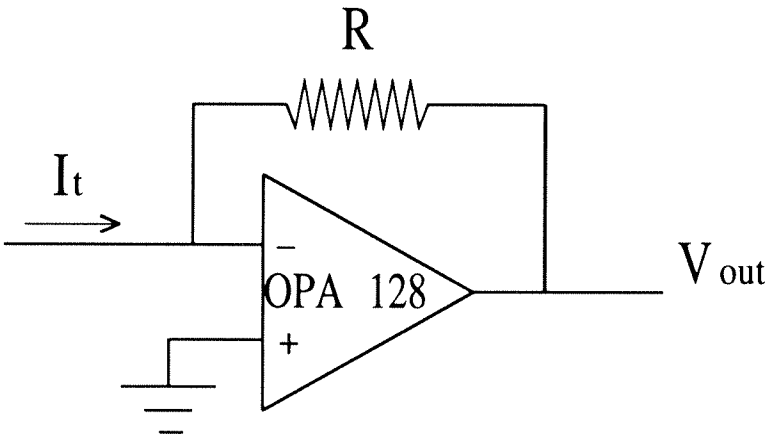

FIGURE 1.6 Current-to-Voltage Converter.

b. 12 bit Analog-to-Digital Converter

The 12 bit Analog-to-Digital converter (A-to-D) digitizes the tunneling signal from the Current-to-Voltage converter on 12 bits and makes it available to the Digital Signal

Processing board as was shown in Figure 1.3. The circuit, presented in Figure 1.7, is divided into four parts.

1) An ultra-low noise amplification of the input signal through an INA110 amplifier from Burr Brown.[15] This amplifier has programmable gains of 1, 10, 100, 200, and 500. In this application, the gain is set at 10 so that a tunneling current of 1 nA at the tip corresponds to 1 V at the A-to-D converter chip.

2) A Sample-and-Hold and Analog-to-Digital converter combination, SHC803 and ADC803 from Burr Brown.[15] The Sample-and-Hold freezes the input data on a clock pulse and inverts it. 150 ns later, the A-to-D is triggered to start the conversion. The A-to-D is set for a range of [-10,0] Volts corresponding to a digitized range of [0,4095].

3) Output ports. The 12 line parallel port from the A-to-D is connected to two successive latches LS373.[16] The first holds the last conversion from the A-to-D. The second, triggered by the Digital Signal Processing board, gets the latest data from the first latch and holds it while the DSP is reading it. A manual push button for transfer as well as a 12 LED display of the current code is also available for calibration and control.

4) A timing circuit. This stage, based on a 10 MHz crystal, determines the sampling frequency of the A-to-D and synchronizes the Sample-and-Hold and latches for every conversion. It is set to allow a digitizing rate of 500 KHz.

The design of the A-to-D as a stand alone unit offers the advantage of being completely independent of the rate at which the DSP is reading data, that is, the data acquisition frequency of the DSP can be viewed as a software variable rather than a hardware constraint. Detailed Schematics of this unit can be found in Appendix A.

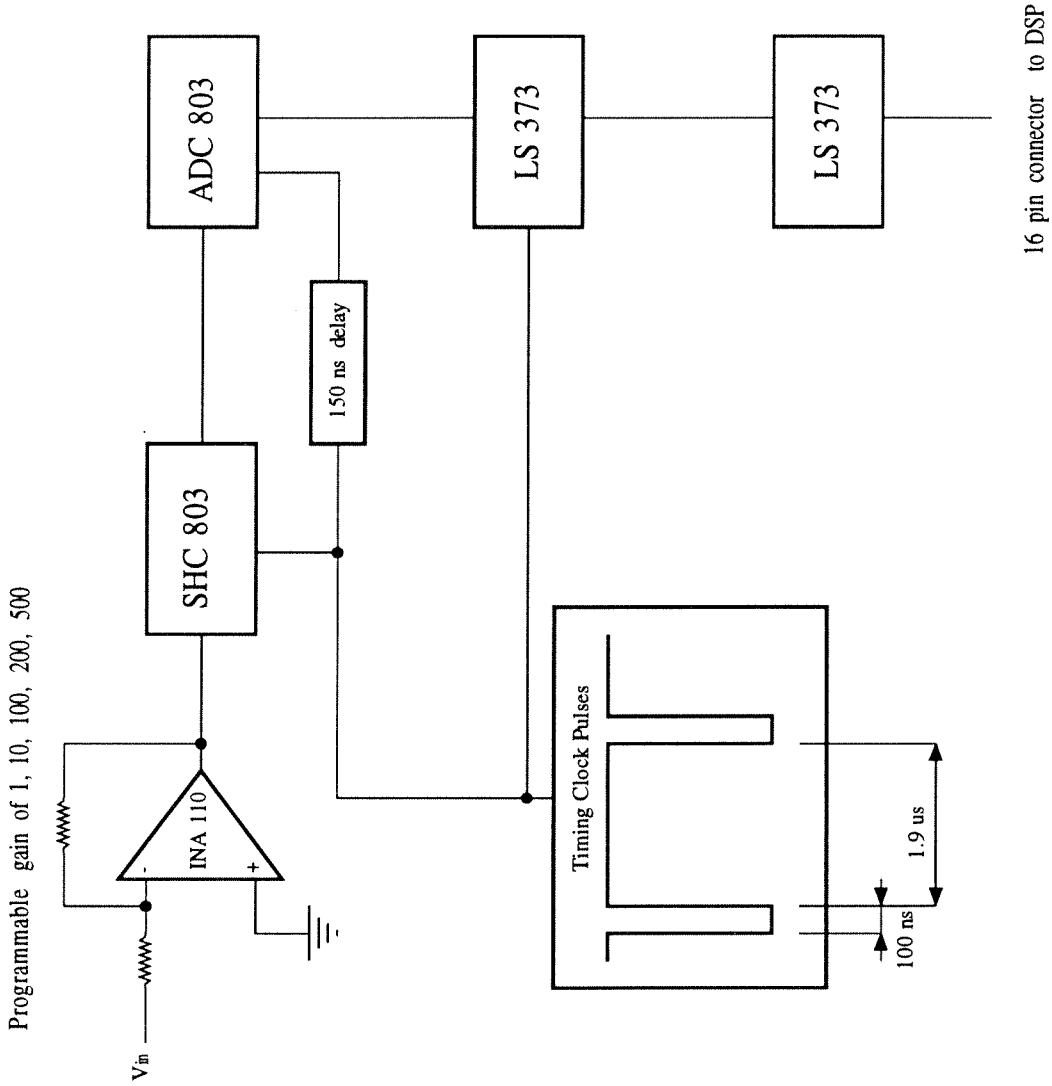

FIGURE 1.7 12 bit A-to-D Converter.

c. Digital Signal Processing Board

The Digital Signal Processing board Motorola DSP56000 is a stand alone computer designed for real time digital processing.[17] In the present application, it is the central control unit of the STM. Reading in the digitized tunneling signal, it compares it to the software defined set point, computes the subsequent correction and outputs it via a 16 bit Digital-to-Analog converter. The frequency at which these corrections occur is software adjustable. The DSP also controls the topographic measurement acquisition and communicates the data at a software adjustable rate to a Personal Computer for real time visualization. A more detailed look at the software running on the DSP56000 will be given in section 1.3.1.

d. 16 bit Digital-to-Analog Converter

Part of the digital signal processing package from Motorola, the DSP56ADC16, a 16 bit Digital-to-Analog converter[18] (D-to-A), was tailor-designed to work with the DSP56000. It is used here to convert the binary corrections computed by the DSP into an analog signal controlling the expansion or contraction of the piezoceramic actuator. The throughput of this device is hardware set at 96 KHz. Its output ranges from [-3,3] Volts for a binary input range of [0,65535].

e. High Voltage Amplifier for the Z Channel

The high voltage amplifier for the Z channel is the final element in the tunneling current feedback loop. Connected to the inside electrode of the piezoceramic tube, its output voltage controls the expansion or contraction of the actuator, *i.e.*, the gap distance. There are actually two inputs to this device which coalesce into one output as can be seen from Figure 1.8.

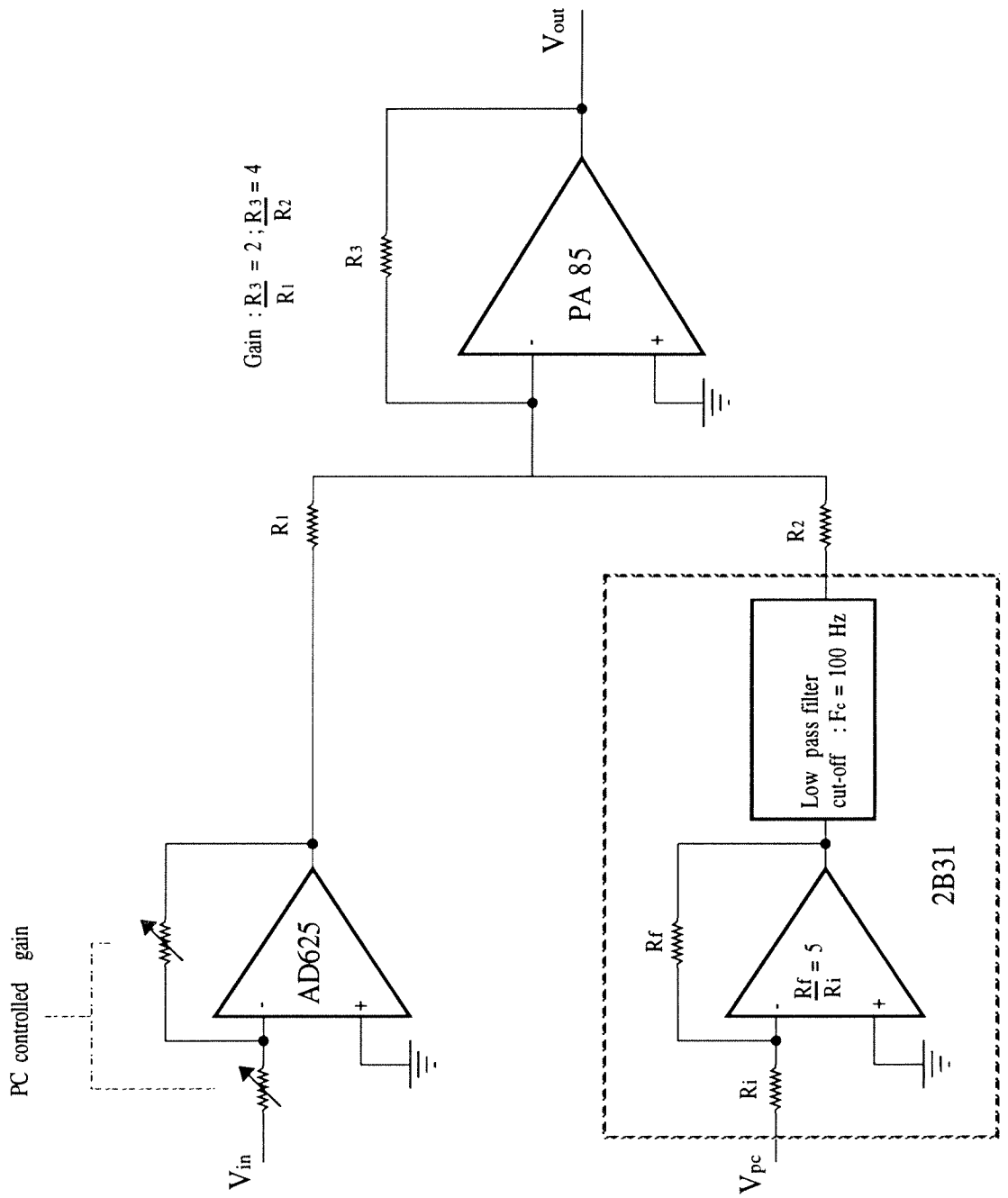

FIGURE 1.8 High Voltage Amplifier, Z Channel.

The first and most important input, labeled V_{in} in Figure 1.8, comes from the 16 bit D-to-A and represents the amount of correction necessary to maintain a constant gap distance, as computed by the Digital Signal Processing board. This signal is amplified through two stages to limit the noise level. The first stage provides the low voltage amplification. The amplifier AD625 manufactured by Analog Device[19] was picked for its ultra low noise and high frequency response characteristics. The gain of this stage can be adjusted through a digital I/O line from the PC (9 pin connector port). The possible gains are 1, 1.56, 2.14, 2.66 and 3.2 . The high voltage amplification is based on the high voltage operational amplifier PA85 from Apex.[20] This stage amplifies the output of AD625 by a factor of two. The resulting signal is then directed to the Z electrode of the piezoceramic tube.

The other input to the amplifier, labelled V_{pc} in Figure 1.8, allows for offsets of the feedback loop, therefore enabling the user to center the topographic measurements within the range of the STM - see section 1.3.2.e. The V_{pc} input is software controlled by the PC. It also undergoes a two-stage amplification. The low voltage amplification is performed by an amplifier-filter module 2B31 from Analog Device.[21] Its gain is hardware set to 5 and the low-pass filter cut-off frequency to 100 Hz. This amplification is followed by a high voltage amplification. The same high voltage amplifier PA85 is used to amplify V_{pc} by a factor of 4. The PA85 is wired as a summing amplifier therefore adding together the feedback loop and offset signals. The range of V_{pc} is [-2.5,2.5] Volts. Therefore the user prescribed offset may vary within [-50,50] Volts or roughly $\pm$ 1 μm in tip motion along the Z axis. Detailed schematics of this circuit are available in Appendix A.

1.2.3 Data Acquisition

When the STM is recording topographic informations of a specimen surface, the signal sent to the tube actuator is also directed to the PC via the DSP board. The PC

then stores and displays the data in real time but also moves the tip to another raster point so that another measurement can be performed. In this section, the various electronic components of the acquisition loop are described, namely, the 12 bit Digital-to-Analog converters of the PC controlling the in-plane position of the tip, the subsequent high voltage amplification of the PC signals and finally the interface between the PC and DSP through which the topographic measurements are transmitted.

a. *12 bit Digital-to-Analog Converters of the PC*

The first task in data acquisition is to position the tip at the location where a topographic measurement is desired. The PC controls the raster generation. It does so through two of the six 12 bit Digital-to-Analog converters on the DDA-06 PC board by Keithley.[22] These two channels are connected to the X-Y piezoceramic driver that amplifies the signal before applying it to the tube actuator.

b. *High Voltage Amplifier for the X-Y Channels*

The purpose of this component is to amplify the two input signals generated by the PC, V_x or V_y, to output high voltage signals V_x^+, V_x^- or V_y^+ and V_y^- which are applied to a pair of opposite quadrant electrodes of the piezoceramic tube. This will in effect bend the tube in the X or Y, direction, thus providing the tip in-plane motion as described in section 1.2.1. Since the X and Y channels are similar, V_x or V_y will henceforth be referred to as V_{in} and V_x^+, V_x^- or V_y^+,V_y^- as V_{out}^+ and V_{out}^-. To obtain two equal and opposite outputs V_{out}^+ and V_{out}^- from one single input, V_{in} is directed to two similar amplification circuits, illustrated as (1) and (2) in Figure 1.9. Circuit (1) takes V_{in} directly as input where circuit (2) first inverts V_{in} through an operational amplifier OP27[19] and sends the subsequent $-V_{in}$ to a circuit exactly identical to circuit (1). Therefore, the output of circuit (1) and (2) will yield equal and opposite V_{out}^+ but V_{out}^-.

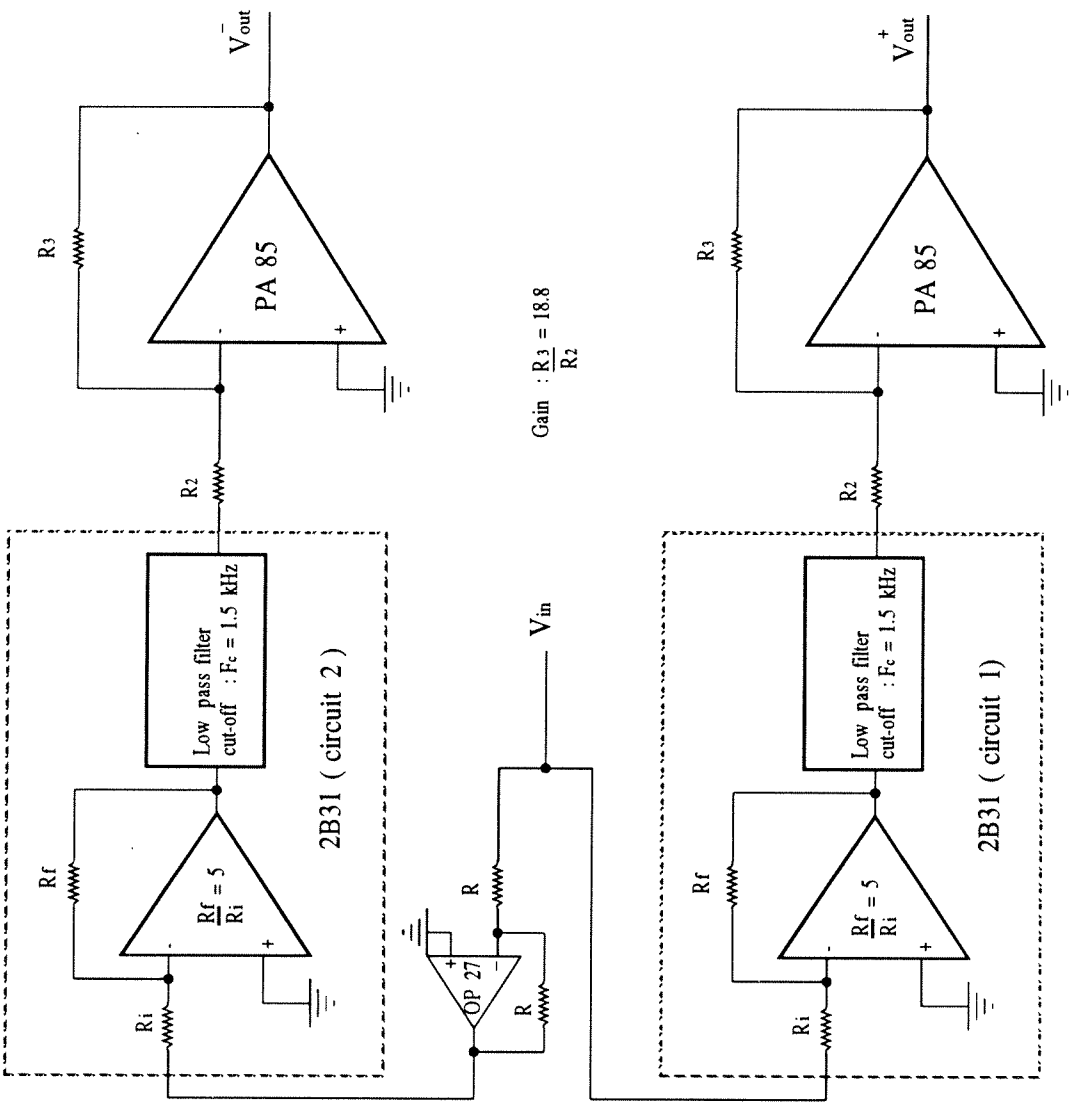

FIGURE 1.9 High Voltage Amplifier, X-Y Channels.

Circuits (1) and (2) are again designed as two-stage amplifiers. The first stage amplification is performed by a combination amplifier-filter 2B31 from Analog Device.[21] The amplification is set to 5 and the low-pass filter cut-off was chosen to be 1.5 kHz. This frequency corresponds to the maximum acquisition frequency at which the microscope is expected to run. The high voltage amplification is a straight forward design based on the high voltage amplifier PA85 from Apex.[20] The gain of this stage is set at 18.8 .

The PC DDA-06 D-to-A has a range of [-2.5,2.5] Volts. Consequently, the output range for $V_{out}^{\pm}$ is [$\mp$235,$\pm$235] Volts which, according to equation (1.2.2) leads to an in-plane range of tip motion of $[-25\mu m, 25\mu m]$ for the selected tube actuator. A more detailed schematic of the X-Y piezoceramic driver is available in Appendix A.

c. PC-Digital Signal Processing Board Interface

Once the tip is in position, the DSP acquires and sends the corresponding topographic measurement to the PC. To perform this task, the PC and DSP must be interfaced. To that purpose, the Host Bus Interface Board of Motorola[17] was diverted from its primary function which is to download program lines rather than data from the PC to the DSP. It has the advantage of not requiring any new hardware but also limits the flexibility of the communication procedure. The data at each raster point is transmitted as a 16 bit word. The decoding from bits to nanometers requires the knowledge of the software adjustable gain selected for the Z channel of the piezoceramic driver.

1.2.4 Structural Support

The two previous sections have described how the feedback loop is supposed to stabilize the tunneling distance between the tunneling probe and the specimen surface, and how topographic measurements could then be acquired. The last problem to address

is how to approach the tunneling range. A number of different solutions to that problem have been found since the first STM[2]was constructed, but most of them can only handle very small samples and are not directly applicable to this work.

Because the specimens in this project may be large (typically 3 cm long) and/or within the loadframe, it was decided to bring the tip to the sample which is the exception rather than the norm in STM design. Furthermore, since the specimens may be of various thicknesses and shapes, it was important for the tunneling acquisition to start from a large distance away (2 cm).

Special care must also be given to the thermal stability of the apparatus. Working in a laboratory environment, the microscope may be exposed to minute changes in temperature. These fluctuations may cause contractions and expansions in the frame of the STM on the order of microns. Thermal drifts as big as $1\mu m/minute$ have been observed in some STMs. Such behavior would render any quantitative observations utterly impossible because of the resulting in-plane distortions of the scans. This potential problem was addressed in two different ways. First, one can inhibit the thermal drift by minimizing the coefficient of thermal expansion of all STM parts and accordingly, Invar, an iron-nickel alloy[23] was extensively used. It combines a very low coefficient of thermal expansion, $\alpha = 10^{-6}\ ^{\circ}C^{-1}$, to good stiffness and machinability properties. Thermal drift may also be controlled by design considerations. Temperatures changes on an axisymmetrical STM with the tip lying along its axis of symmetry, only occasion axisymmetrical contractions or expansions, leaving its axis, $i.e.$, the tip, unaffected.

A simplified schematic of the final STM is presented in Figure 1.10 and a photograph of the apparatus is shown in Figure 1.11. It consists basically of five different parts.

- Microscope lower cylinder: It is a 3" diameter hollow cylinder, bolted to the base via a combination of X-Y translation stages. The outer diameter is threaded

at 36 threads per inch. It can move in the plane of the specimen surface (X-Y) but its Z attitude is fixed with respect to the sample.

- Microscope upper cylinder: Also a 3" in diameter hollow cylinder, its outer diameter is similarly threaded at 36 threads per inch. Two alignment pins corresponding to two fittings in the lower cylinder restricts its motion to a Z translation with respect to its bottom counterpart.

- Tunneling axis: Aligned with the aforementioned cylinders axes, this column comprises the tunneling tip, the tunneling current detector and an Inchworm actuator from Burleigh.[24] The Inchworm has a range of 6.25 mm together with a stepping size of approximatively 5 nm. It is needed in the final stage of tunneling acquisition in closing the gap between the tip and specimen by very small increments.

- Approach ring. Designed as a 3" Inside Diameter cylinder (ID), with a 36 threads per inch thread on its ID, it is intended to fit to the ODs of the lower and upper cylinders. Clockwise or counterclockwise rotation of this ring translates the upper cylinder away from or closer to the lower cylinder along the Z axis. This motion provides the coarse approach capability of the STM. Two peep holes through the lower cylinder allow visual control of the tip-specimen gap distance through a low magnification binocular ($\times$ 60).

- Translation stages. A combination of two orthogonal translation stages is included in the STM between the lower cylinder and the base. Motion of the whole STM with respect to the specimen in the X-Y plane is then made possible by two Inchworm type actuators mechanically tied to each stage.

The procedure to reach the tunneling range can now be laid out. To start with, the specimen is clamped rigidly to the base or to the loading frame and the microscope

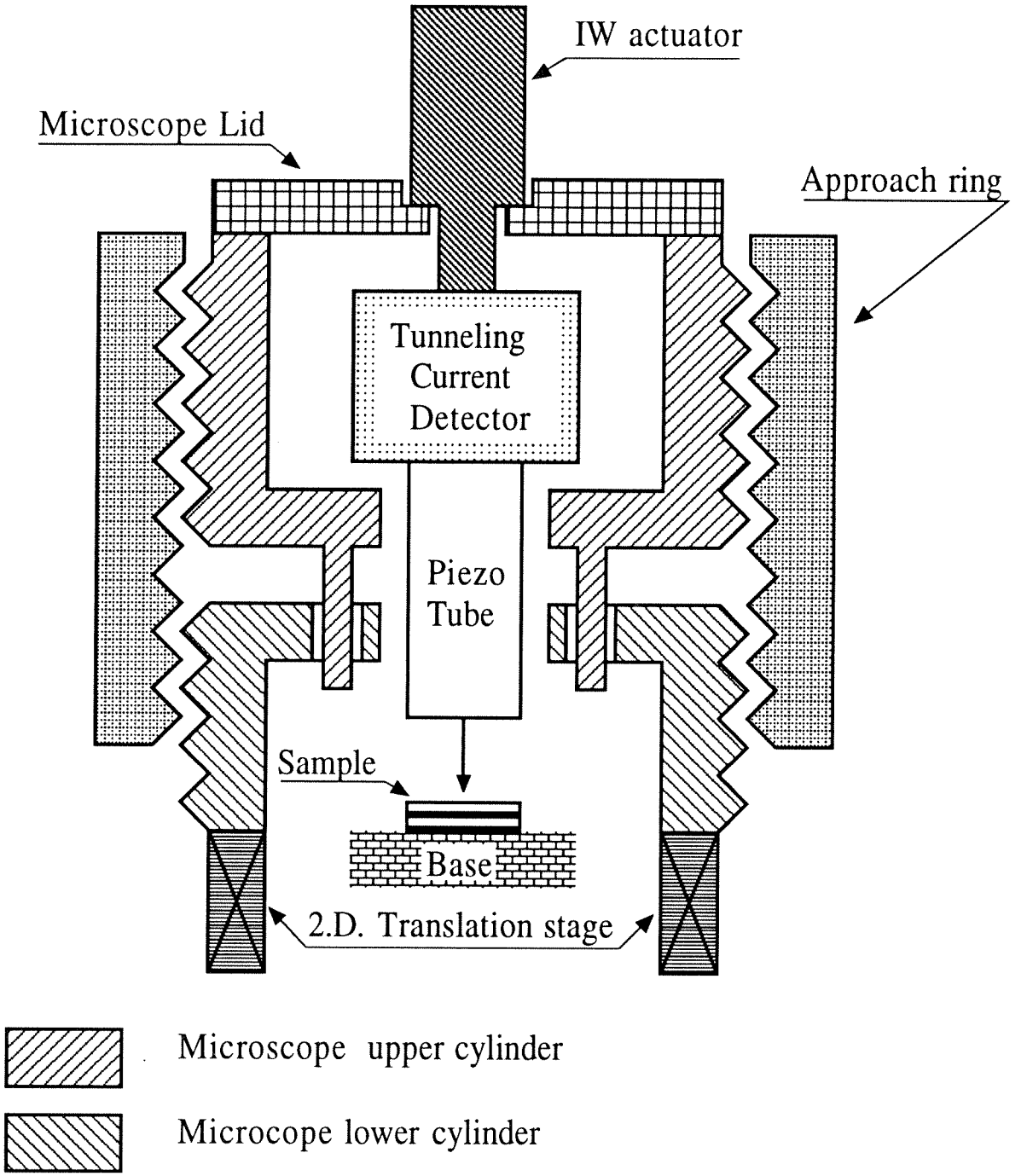

FIGURE 1.10 STM Simplified Schematic.

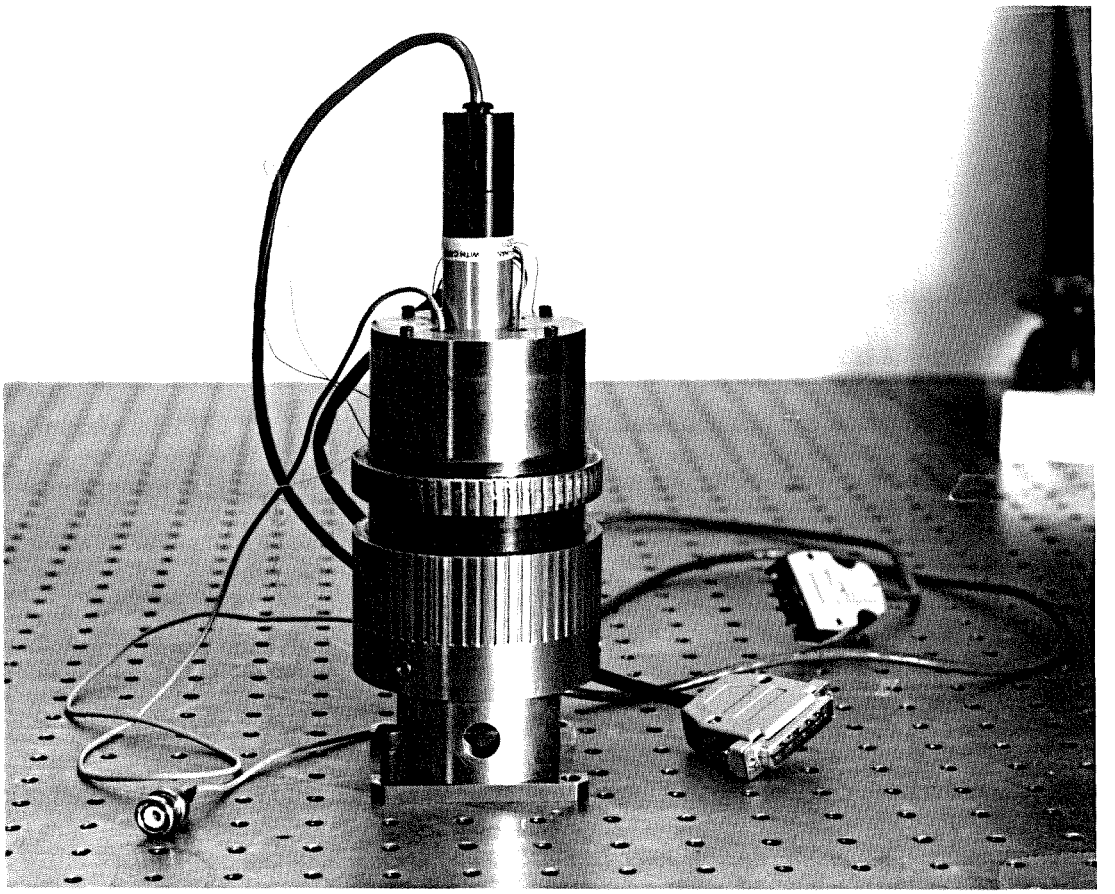

FIGURE 1.11 Photograph of the STM.

assembly is extended, opening the gap between the upper and lower cylinders by counter-clockwise rotation of the approach ring. The STM is then positioned over the specimen and bolted down to the X-Y translation stages. Clockwise rotation of the outside ring brings the tip to within 20 μm of the specimen surface. The approach is visually monitored through the lower cylinder peep holes and binoculars. At that point, the STM feedback loop is triggered. Since no tunneling current can be detected at such a gap distance, the feedback loop extends the piezoceramic tube to its maximum. The Inchworm is stepped down by the PC at a speed of 0.1 $\mu m s^{-1}$ and as soon as the tunneling signal is sensed, the stepping of the Inchworm stops. The feedback loop adjusts the length of the piezoceramic actuators so as to stabilize the tunneling distance and data acquisition can

start. Descriptions of the electronic interfaces between the PC and the three Inchworm actuators are available in Appendix A.

1.2.5 Load Frame

The ultimate goal of this work being to study material deformation under the STM, it was necessary to design a loadframe which would hold and pull on a specimen while positioned under the microscope. The next two sections discuss the design and electronics associated with that device.

a. *Schematics*

It was initially thought that if the straining of the specimen under the STM occurred while the STM tip was out of tunneling range, it would be very difficult to track and scan the same area of the specimen surface before and after deformation, an operation which is absolutely necessary in order to extract the material response to a change in loading conditions (see chapter 4). It was therefore decided to deform the specimen *in-situ*, that is when the tip is in tunneling range, 1 nm away from the specimen surface. Later testing of the the STM revealed that the same specimen area can be easily identified before and after deformation and that the initial concern expressed above is actually not dominantly relevant. However, the STM *in-situ* deformation capabilities were proven absolutely essential later in this work and consequently the loadframe was not changed.

The limitation of *in-situ* straining has several consequences. First and foremost, it limits the type of deformation to which the specimen can be submitted. Indeed, in order to accommodate the 1 μm out-of-plane range of the STM, it is necessary to strain the specimen along the plane perpendicular to the tip. It was therefore decided to build a tensile loading frame with its axis lying along the X axis of the STM as defined in

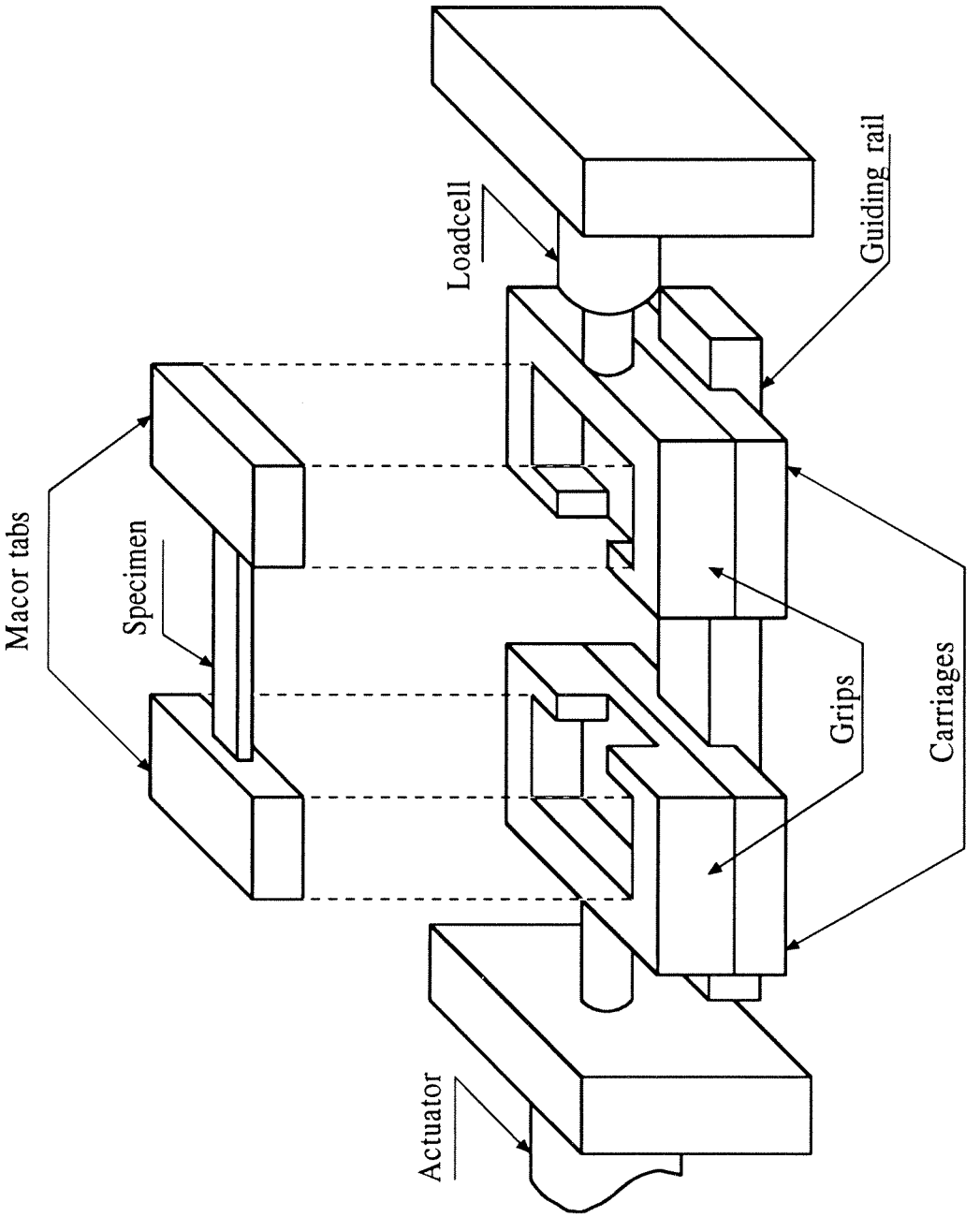

FIGURE 1.12 Loadframe Simplified Schematic.

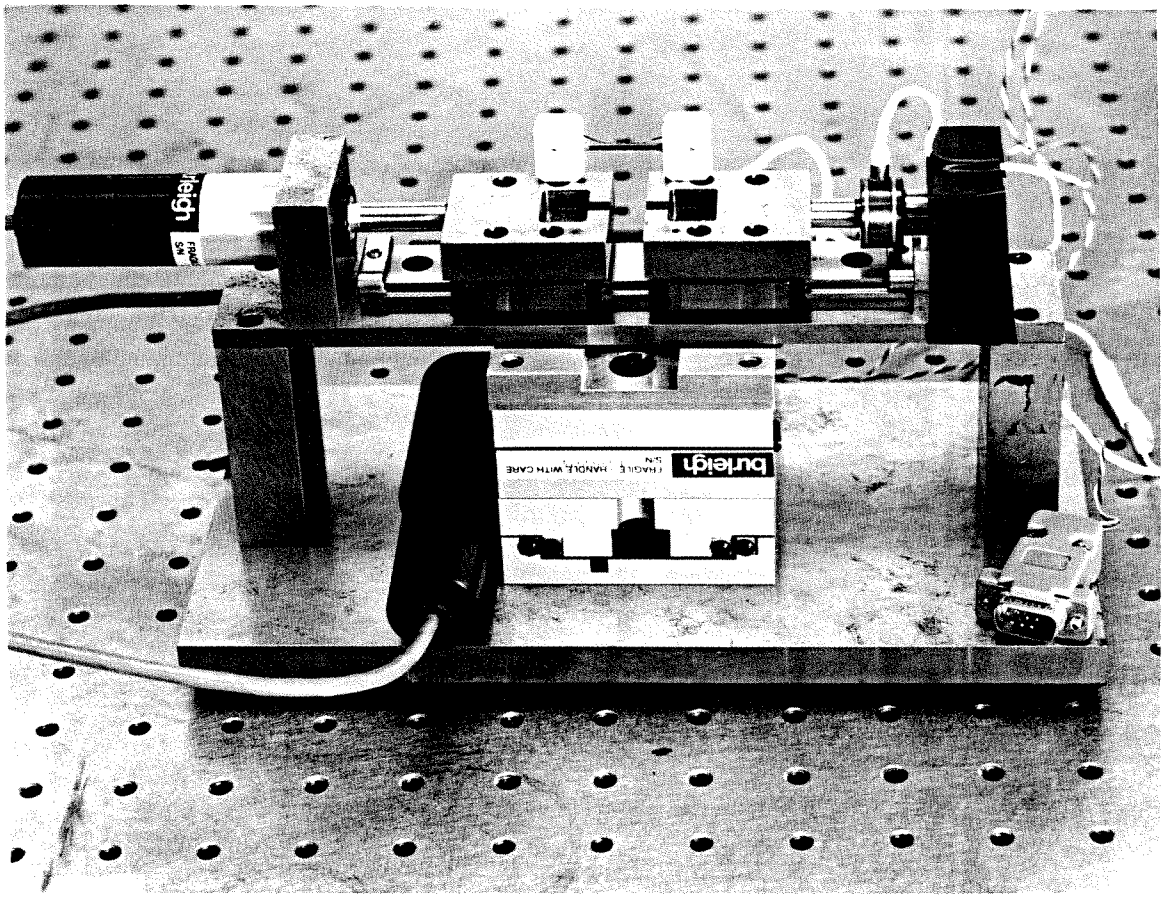

FIGURE 1.13 Photograph of the Loadframe.

Figure 1.4. Secondly, because the STM probe is so close to the specimen, care must be exercized to ensure very smooth and slow straining. As for all other critical motions in this system, an Inchworm actuator was chosen to push/pull on the specimen; its rate of displacement was set at $0.1 \mu m s^{-1}$. The 15 N load limitation on the Inchworm determines the maximum tensile/compressive force to which the specimen can be submitted. It is measured by a 22 N (5 lb) load cell.[25] Finally, to further exclude undue out-of-plane motion of the specimen during straining, the issue of alignment of the loadframe needs to be addressed. Besides requiring high precision machining of the grips, good alignment demands that the translation of one grip with respect to the other is perfectly parallel with the pulling motion. For that purpose, the grips are mounted on high precision carriages

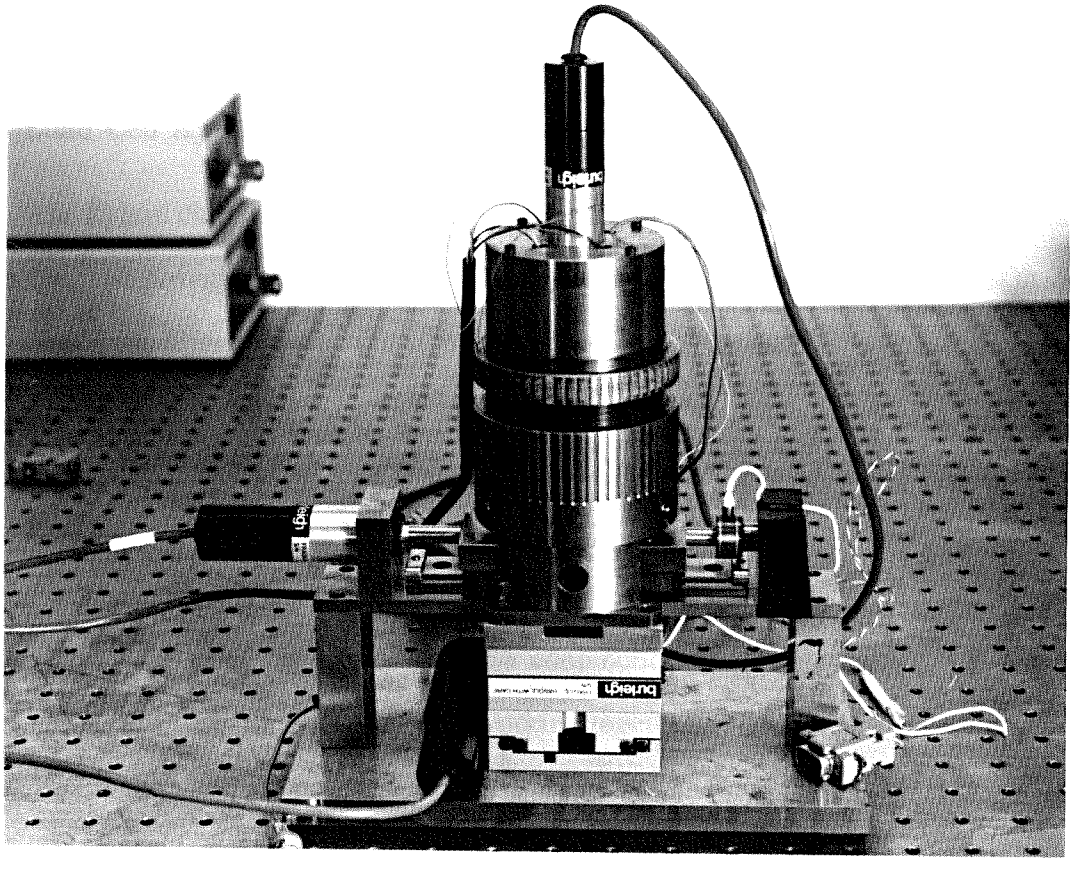

FIGURE 1.14 Photograph of the Loadframe Resting under the STM.

sliding along a guiding rail.[26]

A schematic of the loadframe is presented in Figure 1.12and its photograph in Figure 1.13. Because of the low load capability of the Inchworm, the cross section of the specimen has to be small so that measurable deformation can be induced. A typical specimen has a length of 28 mm, a width of 2 mm, and a thickness varying from 0.25 mm to 0.8 mm. The specimen is glued to tabs machined from Macor (machinable ceramic from Corning). The low coefficient of friction of that material allows the tolerance on the hard steel grips to be kept very tight without facing insertion problem of the tabs in the grips. As for all the other Inchworms of the system, the motion of the straining actuator is controlled by

the PC - see Appendix A.

b. Load Cell Amplifier

The hybrid chip 2B31 from Analog Device is the unique component in the load cell amplifier.[21] It provides an excitation voltage set at 5 V, a signal amplification set at 240 and a low-pass filter on the output signal whith a cut-off frequency adjusted to 10 Hz. A schematic of this circuit is presented in Appendix A.

1.3 Software

The backbone of the microscope is a conjunction of two computers, a PC and a Digital Signal Processing board (DSP) working together. The PC, an IBM clone 386 - 33 MHz is the interface between the STM and the user. The Digital Signal Processing board, Motorola DSP56000, takes care of all the critical tasks, *i.e.*, feedback loop controls and data acquisition. The following sections present a an overview of the software that controls these two computers.

1.3.1 Digital Signal Processing Board Software

The DSP was programmed in assembly language.[27] The software is structured around three main interrupt routines. An interrupt routine has the characteristic of being a more or less independent set of instructions which are executed in priority upon external or internal triggers. Once an interrupt routine is triggered, the computer "interrupts" the normal flow of its program and immediately deals with the request. Figure 1.15 presents the three main interrupt routines of the DSP program, namely feedback loop control, data acquisition and parameter updating.

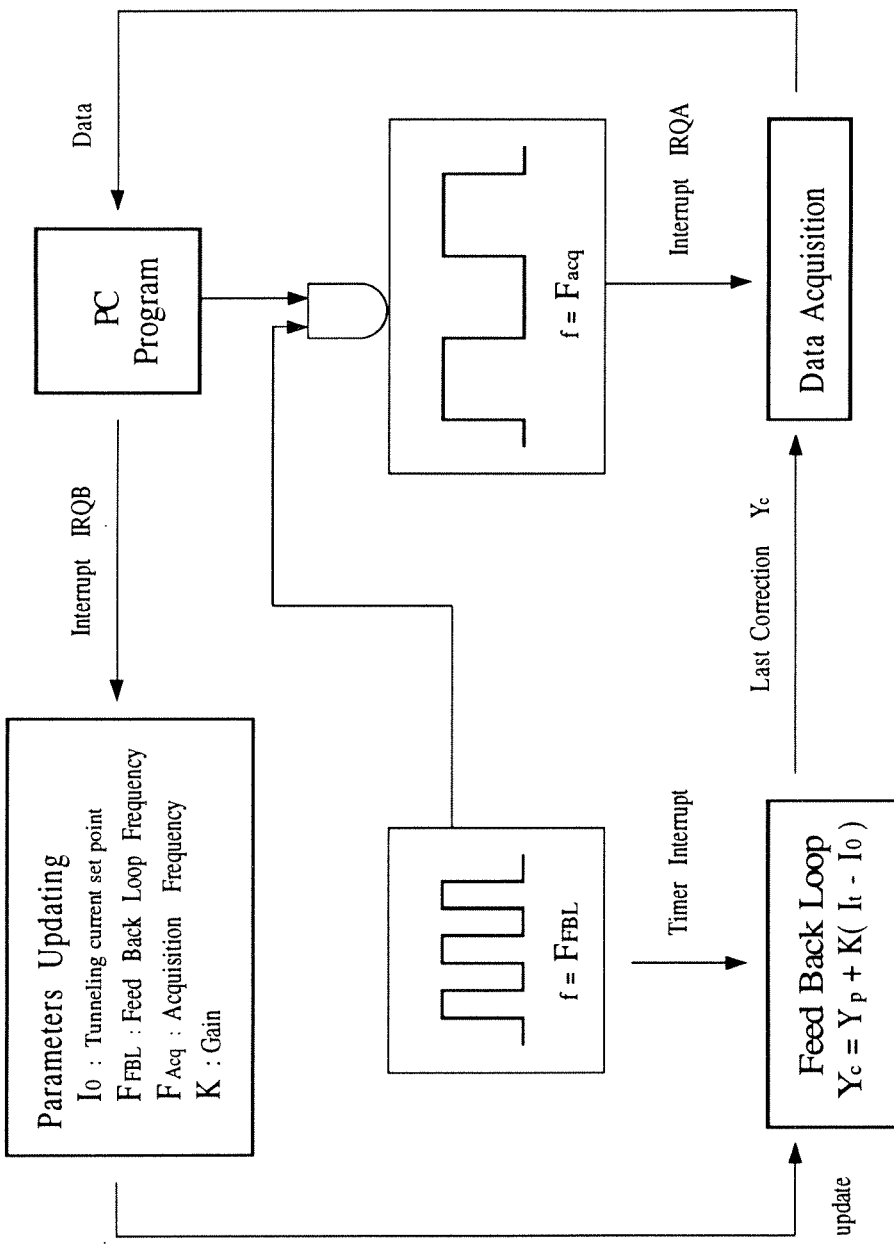

FIGURE 1.15 Chart of the Digital Signal Processing Board Program.

The critical task of the DSP is to ensure that the STM tip does not crash onto the specimen surface. It is therefore critical for the position of the probe to be constantly monitored and adjusted. To that end, the feedback loop control has been programmed as the highest priority interrupt routine of the software. Triggered by the internal DSP clock, every time it is called, at a user adjustable frequency F_{FBL} (typically $F_{FBL} = 100\ KHz$), it senses the latest value of the tunneling current I_t and computes the appropriate correction to the piezoceramic actuator by

$$Y_c = Y_p + K(I_t - I_0), \tag{1.3.1}$$

where

Y_c = new correction,

Y_p = previous correction,

I_t = present value of the tunneling current,

I_0 = set point for the tunneling current,

K = feedback loop gain.

This very simple equation is a mix between a proportional controller, for fast response, and an integral controller to limit residual errors. Once Y_c has been computed, it is sent via the 16 bit D-to-A and high voltage amplifier to the tube actuator. The various parameters involved in that loop, *i.e.*, K, I_0 and F_{FBL} are adjustable at anytime as explained later in section 1.3.2.a. It is important to note that once this routine is activated, it cannot be stopped and its completion supersedes any other tasks required from the DSP. Only during those moments when the control loop is finished and the new one has not yet started will the DSP process any other requests.

Also very high in the priority list is the data acquisition routine. Since the data storage is performed by the PC, one has to ensure synchronicity between the DSP and the PC. It is achieved by programming the acquisition loop as an external interrupt, *i.e.*, a routine triggered from an external source. When the PC is ready to receive a new datum, it sends a flag to the DSP via a digital I/O line. This signal, combined with a DSP clock pulse, triggers the data acquisition. The latest feedback correction is then transmitted to the PC. The PC acknowledges the information by disabling the interrupt and processes the data as described in the next section. As soon as it is again ready to acquire a new datum, it re-enables the interrupt and at the next DSP acquisition pulse the sequence may be restarted. This two-trigger combination offers flexibility in the timing of the two computers and allows the acquisition frequency F_{ACQ} to be software adjusted. F_{ACQ} can range from 0 to 3000 Hz.

Finally the last interrupt of the DSP program is the parameter updating routine. It possesses the lowest priority. Upon user request, the PC will externally trigger this routine to update some of the critical parameters of the DSP program, namely the feedback loop frequency F_{FBL}, the data acquisition frequency F_{ACQ}, the tunneling current set point I_0 and the gain of the feedback loop K.

In such a software architecture which incorporates several interrupt routines, it is important to understand that the DSP is predominantly inactive. Only at specific moments and for very short times is computation required. Consequently, response to any priority request is almost instantaneous.

1.3.2 PC Software

Written in C, this code was programmed userfriendly and performs seven different tasks, each accessible through a main menu. Here is an overview of each of these parts.

a. *Parameter Adjustment*

This routine gives the user the option to change interactively eleven different parameters relevant to the STM operation. The main ones are :

- I_0, tunneling current set point. It can be adjusted from 0 to 10 nA. Upon adjustment, the new value of I_0 is directed to the DSP by triggering an interrupt routine.
- I_{TH}, detection threshold of the tunneling current. Because of inherent noise in the tunneling signal, the DSP will read a non-zero tunneling signal even in non-tunneling configurations. If the current detected is below I_{TH}, the DSP will not interpret it as tunneling current but as noise and consequently will not adjust the feedback loop.
- K, feedback loop gain. As described in equation (1.3.1), K represents the multiplicative factor by which the difference between the tunneling current and its set point is amplified. As for I_0, the new value is transmitted to the DSP for immediate update.
- V_b, bias voltage. Tunneling microscopy requires a bias voltage between the tip and the specimen. The PC will relay the chosen value of V_b to the specimen through a 12 bit A-to-D. V_b can be adjusted between $-5\ V$ and $5\ V$.
- W_x, W_y, scan size along the X and Y direction. These variables define the voltages applied to the piezoceramic tube at the upper right corner of a scan. $W_x = 50\ V$ means that the roster of points for the scan will correspond to voltages ranging from $-50\ V$ to $50\ V$ on the two X quadrant electrodes. W_x and W_y may be adjusted between 0 and 200 V.
- n_x, n_y, number of raster points along the X and Y axes. Once W_x or W_y is known, it is divided into n_x or n_y intervals respectively. The width of those

intervals represents the pixel size of the scan. Knowledge of both W_x, W_y and n_x, n_y is necessary to fully define the scan raster.

- F_{FBL}, feedback loop frequency. F_{FBL} determines how many times per second the feedback loop is required to check and correct the gap distance. It ranges from 0 to 100 KHz.

- F_{ACQ}, acquisition frequency. F_{ACQ} is the rate at which the tip scans the specimen surface and acquires topographic measurements. It ranges from 0 to 3000 Hz.

- Z_r, out-of-plane range. Depending on Z_r, the the maximum range of motion of the tube actuator along the Z axis is set at roughly 170 nm, 270 nm , 370 nm, 450 nm or 550 nm. Z_r can be thought of as a standard magnification in the Z direction.

It is just this capability of the software to adjust these parameters that makes digital STMs so much more flexible than their analog counterparts. A regular STM would require difficult hardware adjustments to achieve the same results.

b. Tunneling Acquisition

This option starts an automatic tunneling acquisition sequence. It should only be triggered once the tip has been approached manually to within 20 μm of the specimen surface. The tip is lowered by 200 nm toward the specimen using the Inchworm actuator. The piezoceramic tube is then slowly extended by increments of 0.1 nm After each increment, the DSP senses the tunneling current. If I_t is found larger than I_{TH}, the tube extension is stopped, the feedback loop is started and the tunneling current is then stabilized at its set point I_0. Otherwise, if I_t is less than I_{TH}, the stepping (down) continues. When the actuator is fully extended and no tunneling current has been detected,

it retracts 0.3 μm, the Inchworm brings the tip another 200 nm closer to the specimen and the whole process starts again until tunneling is detected. Tunneling acquisition typically takes twenty minutes.

As explained in section 1.2.4, this automated sequence can be bypassed. If I_{TH} is set to 0, the DSP believes it has detected the tunneling signal because of electronic noise upon starting the automatic tunneling acquisition sequence. However, the probe is far away from the sample surface and the detected I_t is much lower than the set point I_0. Consequently the tube actuator gets fully extended. The Inchworm actuator can then be used to interactively approach the tip closer to the specimen. As soon as I_t reaches a detectable level, as can be monitored on the PC screen, the user just stops the Inchworm and the STM is operational. This alternate procedure only requires a couple of minutes and was used successfully throughout this work afer experience with the STM was gained.

c. *Image Acquisition*

Triggering this option starts the data acquisition procedure. The scan raster is computed and the tip is positioned over the first point of the scan at the lower left corner of the image. Actually, two images are acquired at the same time : the forward scan where the tip follows $x = const.$ grid line in the positive Y direction, and the backward scan where the tip is also moved along $x = const.$ grid line but in the negative Y direction - see Figure 1.16. That way, each image is obtained following the same leg of the eventual hysteresis loop of the piezoceramic tube (see section 2.5.1). As the data acquisition starts, the PC screen switches to a high definition graphic mode and new data points are displayed in real time, color-coded at the pixel location corresponding to the in-plane tip position. Because of speed requirements in the data processing on the PC side, this option is computer intensive and it is not possible to abort it once started.

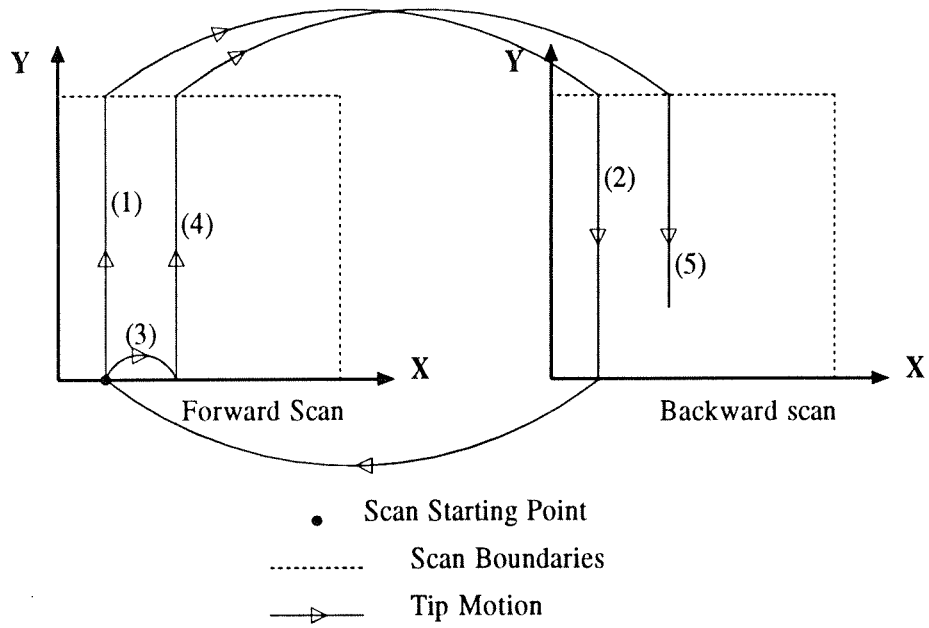

FIGURE 1.16 Forward and Backward Scans.

d. Ending Tunneling

In order to end a tunneling session, as much care must be given to retract the tip as was given to approach it. Upon selection of tunneling termination, the Inchworm actuator steps the tip away from the specimen by approximatively 15 μm. The feedback loop is then stopped and the STM electronics can be switched off.

e. Z-Offsetting

Z-offsetting is used to center the out-of-plane range of the STM. For instance if one were to choose the Z range of the piezoceramic actuator to be 550 nm and the asperities of the specimen are also on the order of 550 nm high, one would have to make sure that the zero correction position of the tip corresponds to a 225 nm elevation. Two phenomena are symptomatic of a improperly adjusted offset as illustrated in Figure 1.17, namely

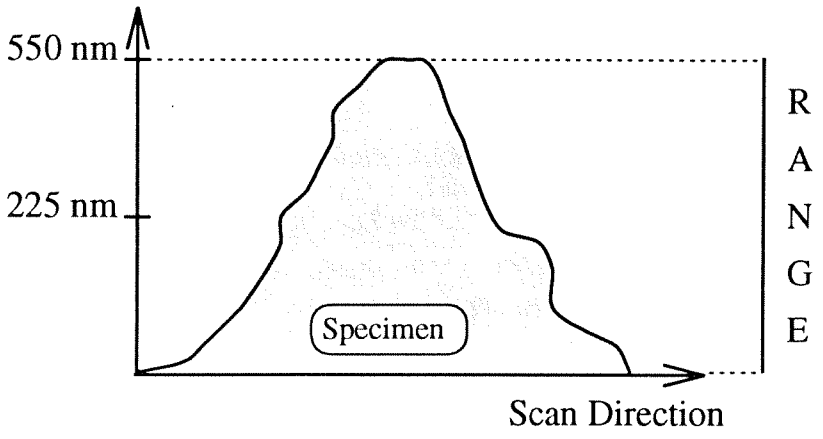

a. Properly adjusted range.

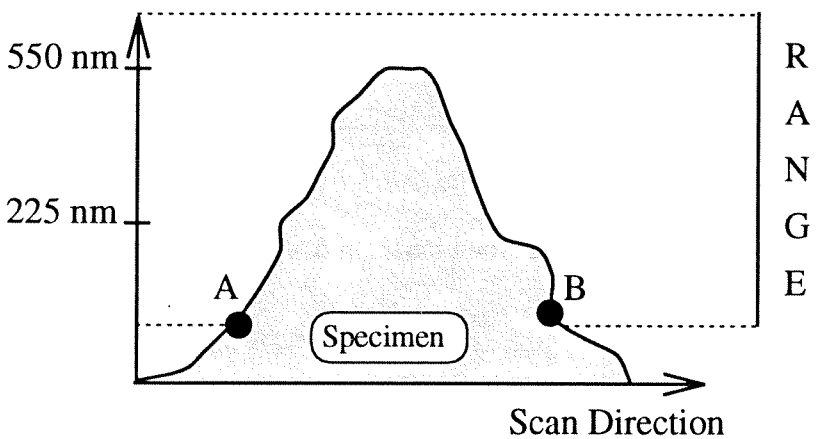

b. Offset too high. Loss of signal before A and after B.

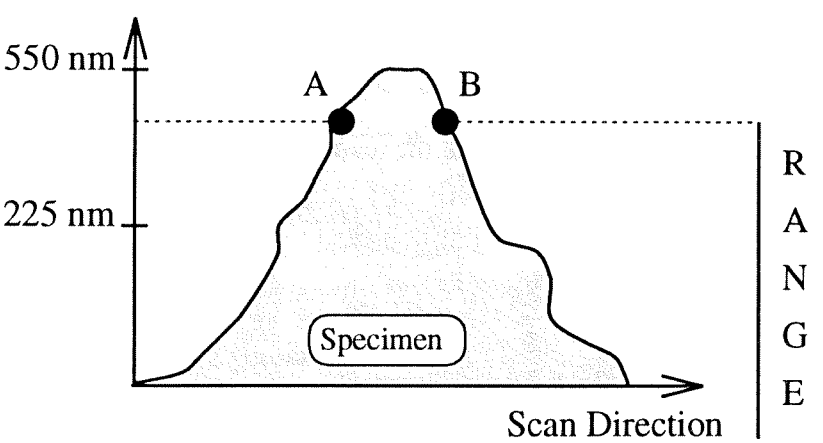

c. Offset too low. Tip-specimen contact from A to B.

FIGURE 1.17 STM Offset Adjustment.

- Loss of tunneling signal. If the offset is too high, say 400 nm, the lower part of the asperities is out of reach. Data points in the lower regions are not valid.
- Tip-specimen contact. If the offset is too low, say 100 nm, the tip is not able to retract sufficiently to accommodate the asperities. As a consequence, the tip comes into contact with the specimen, damaging both and ruining the scan.

It is obvious from the previous explanation that the offset should always be rather higher than lower. The user has two ways of adjusting it. First, the correction of the feedback loop can be offset by a multiple of V_{PC} as was described in section 1.2.2. The second solution involves a "mechanical" offset of the feedback loop rather than an electronic one. Since the Inchworm actuator has a resolution of 5 nm, it can step the tip up or down within the tunneling range. As it goes up/down, the gap distance momentarily increases/decreases. To compensate that change, the feedback loop expands/contracts the piezoceramic tube which in effect increases/decreases the offset.

f. X-Y Positioning

The STM is bolted down to a combination of two orthogonal translation stages which provides X-Y motion of the whole apparatus with respect to the specimen. Each stage is remotely controlled by the PC. Triggering this function enables the user to position the microscope interactively over the area of interest. Details about the interface electronics is available in Appendix A.

g. Specimen Straining

The load providing actuator of the load frame is also remotely controlled by the PC. As the user loads the specimen, the load is monitored on a digital voltmeter and should not exceed 15 N. Details about the interface electronics is available in Appendix A.

CHAPTER 2

STM Calibration

As for any other apparatus, the various subsystems making up the STM must be thoroughly evaluated. However, in the case of a digital microscope, the task is a little easier than for its analog counterpart. Indeed, because all the critical STM parameters are software adjustable, the calibration needs only to check that the different Analog-to-Digital (A-to-D) and Digital-to-Analog (D-to-A) converters are linear. There are three such systems in the current STM design : the 12 bit A-to-D converter digitizing the tunneling signal, the 16 bit D-to-A converter providing the feedback loop correction to the Z electrode of the piezoceramic tube actuator and the two 12 bit D-to-A converters controlling the in-plane position of the tip. The errors associated with each of these components defines the final resolution of the apparatus. Finally the critical piezoelectric properties of the tube actuator are investigated to yield the global calibration of the STM.

2.1 STM Parameter Adjustment

Among all the software adjustable parameters in the STM, the feedback loop gain K and the data acquisition frequency F_{ACQ}, need to be determined experimentally to optimize the scan quality.

Adjusting the feedback loop gain K is straight forward. Theoretically, K should be as big as possible to decrease the time response of the feedback loop. However, if K is too large, the feedback loop is underdamped which results in an oscillatory behavior of

the correction signal.[b] To determine the optimum value of K at a given Z magnification, one only needs to ramp K from very small, say 10^{-6} to higher values, say 10^{-2}, while monitoring the feedback loop output. The highest value of K that still stabilizes the feedback loop without inducing oscillations is the optimum for the system. For the lowest Z magnification of the STM, the proper feedback loop was found to be $K = 10^{-3}$. The feedback loop time response may be critical to avoid tip-specimen contact when scanning a very rough specimen. In such cases, the value of K should be increased at the expense of scan quality.

The other parameter which requires experimental adjustment is the data acquisition frequency F_{ACQ}. Again, there are two opposing requirements on F_{ACQ} : in the event of drift of the specimen under the STM, the distortion at each pixel is related to the rate of drift divided by the scanning speed; therefore, to limit that effect, F_{ACQ} should be chosen as high as possible. This is very similar conceptually to photographing a moving object with a regular camera; the faster the aperture time, the sharper the picture. On the other hand, a high scan speed results in less time at every pixel location, so that, less time is available for the feedback loop to reach its steady state and achieve an accurate height adjustment. Experience showed that a good compromise for high quality topographies is $F_{ACQ} = 400\ Hz$.

2.2 12 bit Analog-to-Digital Converter

The calibration of the 12 bit Analog-to-Digital converter (A-to-D) which samples the tunneling signal was performed by connecting a very stable voltage source to its input and recording the corresponding binary code on the Digital Signal Processing board. The result was then transmitted to the PC, thus duplicating exactly the STM operation.

---

[b] High values of K makes the piezoceramic tube vibrate up and down in the KHz range, resulting in an audible noise.

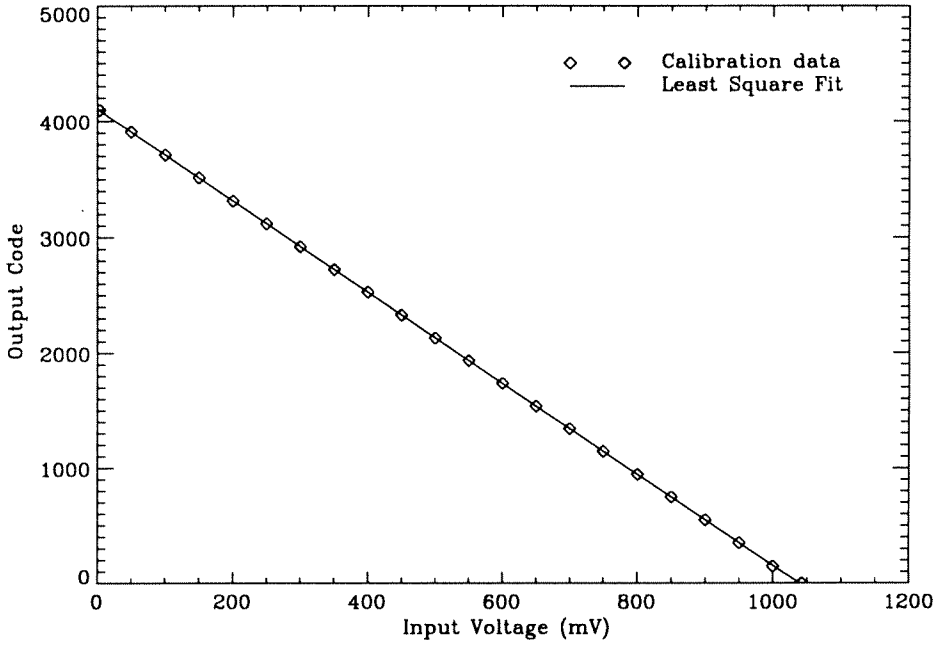

FIGURE 2.1 Calibration of 12 bit Analog-to-Digital Converter.

Figure 2.1 presents the results of the calibration. The input voltage was ramped from 0 to 1042 mV and the output code was recorded decreasing from 4095 ($2^{12} - 1$) to 0. If Figure 2.1 shows the linear response from the A-to-D to a voltage ramp, the critical information to assess the performance of the component is the deviation from linearity expressed in term of a "Least Significant Bit" unit (LSB). This quantity was obtained by least square fitting a straight line through the calibration points and subtracting it from the original measurements.[c] The result of this operation is presented in Figure 2.2. A conservative assessment of the absolute error leads to

$$\text{Output Code} = \text{Theoretical Code} \pm 1\ LSB. \tag{2.2.1}$$

The question that needs to be answered now is whether this level of noise is acceptable.

---

[c] The least square fit was performed for $0 < V < 1000\ mV$, excluding the first and last calibration data. These latter points do not represent the behavior of the A-to-D since, being located at the extremes of the input range, they incorporate the results of electronic saturation.

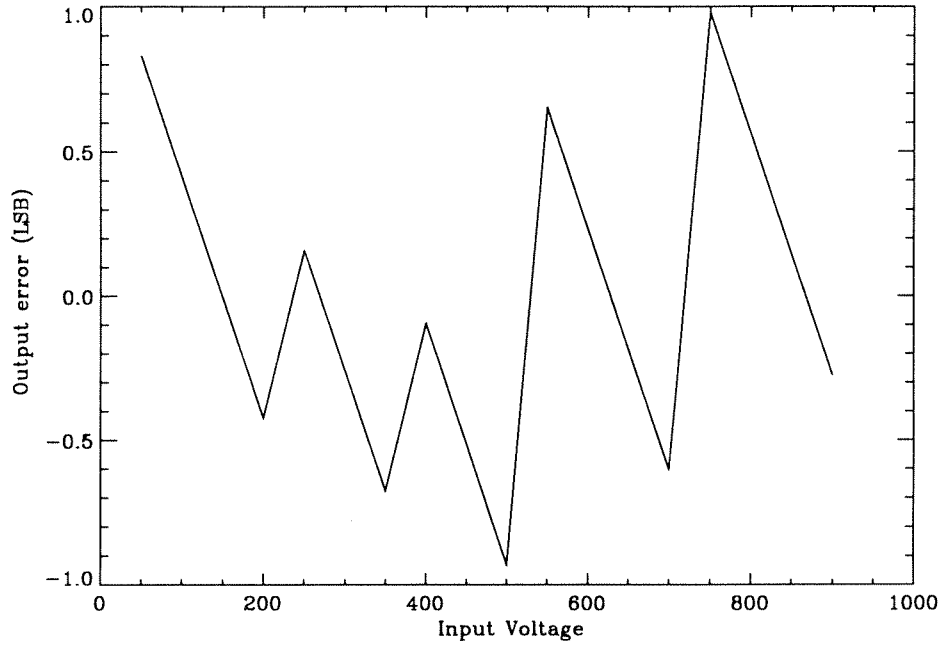

FIGURE 2.2 Error Assessment for the 12 bit Analog-to-Digital Converter.

This question can be resolved by calculating the effect of the digitization error of the tunneling signal on the feedback loop output. In the Digital Signal Processing computer (DSP), each variable is a number between -1 and 1. Consequently, $\pm$ 1 LSB error in the signal code translates into a $2/2^{12}$ uncertainty within the DSP, or $\Delta_{IN} = 4.9 \times 10^{-4}$. The output of the DSP is a 16 bit Digital-to-Analog converter (D-to-A). To increase the output code by one LSB, the internal representation of that code needs to change by $2/2^{16}$ that is a threshold of $\Delta_{THRES} = 3 \times 10^{-5}$. The relationship between Δ_{IN} and the subsequent error on the output Δ_{OUT} is the feedback loop equation,

$$\Delta_{OUT} = K\Delta_{IN} = 4.9 \times 10^{-7} \tag{2.2.2}$$

where K, the feedback loop gain, is set at its typical value of 10^{-3} as discussed in section 2.1. From relation (2.2.2) it is obvious that

$$\Delta_{THRES} > \Delta_{OUT}, \tag{2.2.3}$$

which means that the error in the input code is not sufficient to alter the output code at all. There is therefore no need to improve the A-to-D.

Another way to understand this error assessment is to state that 1 LSB in tunneling current amounts to less than 1 LSB in output correction. In other words, 12 bit digitization on the input signal is "overkill." The STM would perform similarly if the tunneling voltage was sampled on eight true bits.

2.3 High Voltage Amplifier, X-Y Channels

This section discusses the calibration of the electronics responsible for the in-plane positioning of the STM tip during scanning. To control the tip motion the PC is connected digitally to two 12 bit D-to-As, one for each axis. The tip position along each axis can only be one of 4096 possible locations, each uniquely identified by a binary code between 0 and 2^{12} (4096). When the PC moves the probe, the codes corresponding to the tip end position are transmitted to the two D-to-As. The subsequent voltages are amplified and split into two signals (per axis) V_X^+, V_X^- and V_Y^+, V_Y^-, each connected to the relevant tube quadrant. The resulting in-plane deformation of the actuator is, at this point, assumed to be linear with $V_X^+ - V_X^-$ and $V_Y^+ - V_Y^-$; therefore, calibrating the PC-amplifier combination mainly consists of checking that the excitation voltages are linear with respect to the PC generated input codes. If this is indeed the case, it means that the PC unit of motion, *i.e.*, 1 LSB, represents a constant voltage increment at the tube electrode and generates a fixed displacement increment of the tip throughout the possible range of motion. Also, through the calibration, the squareness of the scan grid can be assessed.

The calibration for each axis was performed by measuring the two relevant quadrant voltages on the piezoceramic tube corresponding to a given PC generated code. The data recorded here span only code 1548 to 2548 which is the code range for all the scans acquired in this work.

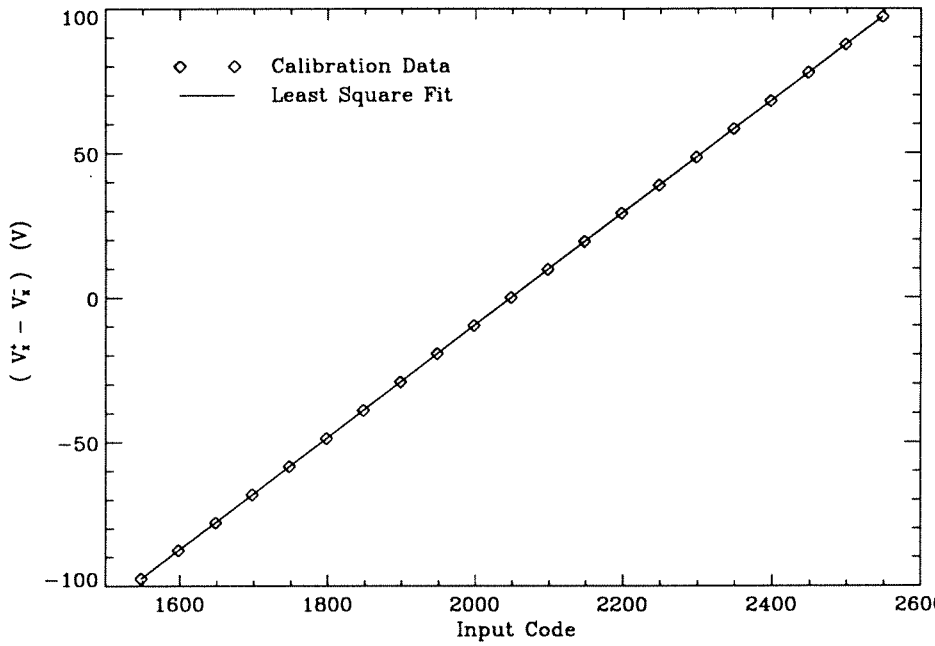

FIGURE 2.3 Calibration of the High Voltage Amplifier, X Channel.

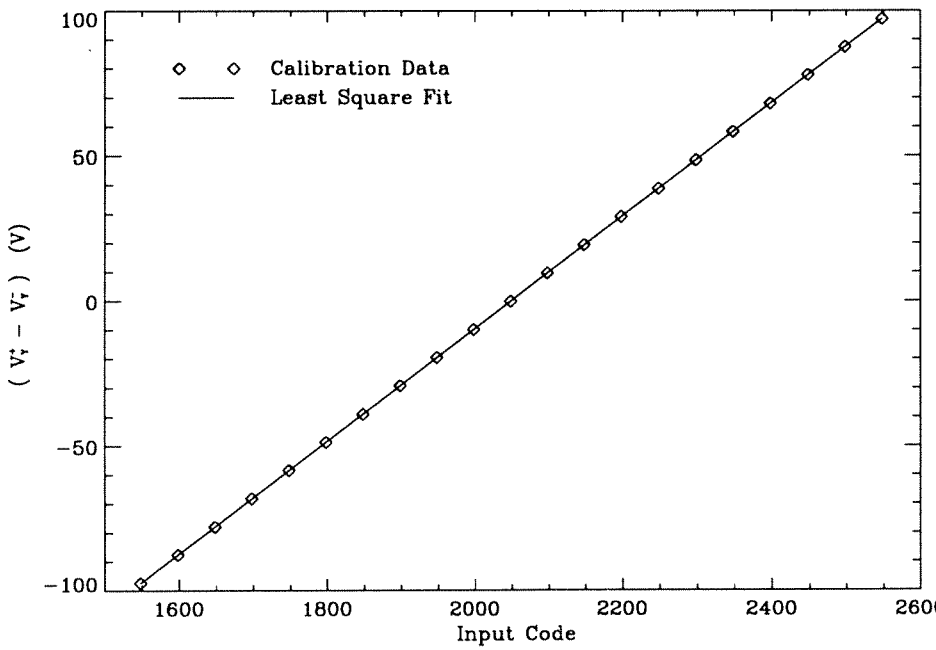

FIGURE 2.4 Calibration of the High Voltage Amplifier, Y Channel.

Figures 2.3 and 2.4 present the raw calibration data for both axes. For each set, a straight line was fitted to the data and it was found that[d]

$$\begin{cases} V_X^+ - V_X^- = 0.19449223 \times \text{code} + \textit{constant} \\ V_Y^+ - V_Y^- = 0.19449247 \times \text{code} + \textit{constant}. \end{cases} \tag{2.3.1}$$

The leading coefficients in relation (2.3.1) represent the in-plane units of motion expressed in volts. The equivalence between these X and Y voltages and physical distances will be determined by the tube calibration.

As is customary in digital electronics calibration, the deviation from linearity is more important than the linear trends in the data. This can best be assessed by computing the difference between the data and their linear fit, normalized by the leading coefficient of the fit. These errors are presented in Figures 2.5 and 2.6 for the X and Y axis respectively. The deviation from linearity can be readily estimated at $\pm$ 0.1 LSB. Note that because of this low error estimate, the structure of the noise, whether random or systematic is irrelevant. To be thorough, one should add to that error the high frequency electrical noise which amounts to $\pm$ 10 mV per channel or again ± 0.1 LSB. So, assuming the response of the piezoceramic to be perfectly linear with voltage, the distance between two specific features of a specimen topography can be measured within ± 0.2 LSB.

The final check in the performance characterization of the PC - amplifier combination addresses the squareness of the scan grid. It was shown above that the linearity of the positioning was indeed good. Therefore equation (2.3.1) accurately reflects the behavior of the system. The squareness may then be quantified by the ratio of the two leading coefficients of the linear fit for each axis, giving a squareness factor such that,

$$\text{Squareness factor} = \frac{0.19449223}{0.19449247} \approx 1 - 10^{-6}. \tag{2.3.2}$$

---

[d] The two leading coefficients are displayed with 8 significant digits, not for their physical meaning but to give a basis for comparison.

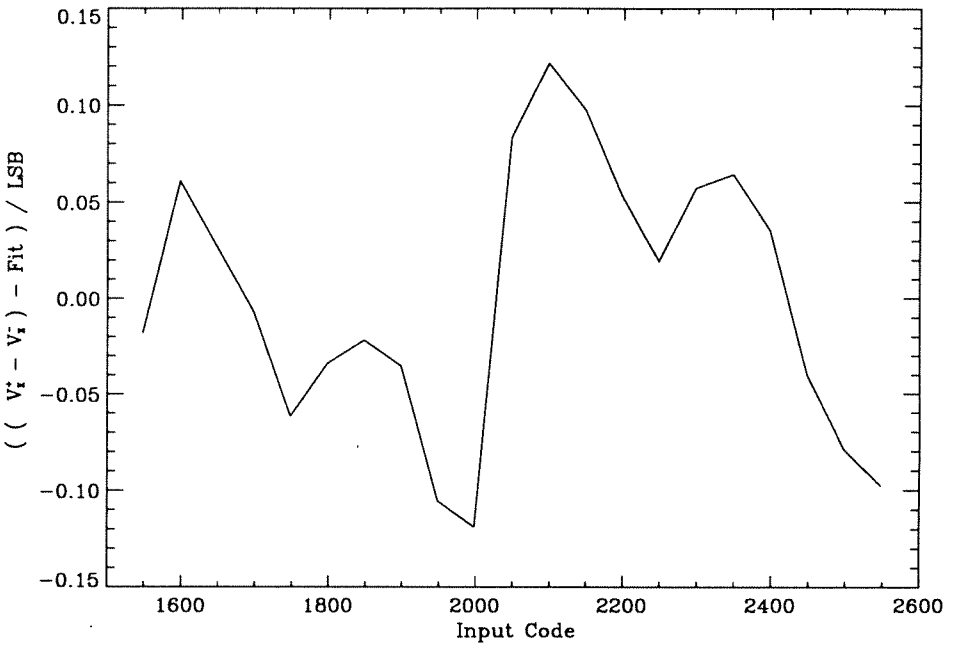

FIGURE 2.5 Error Assessment for the High Voltage Amplifier, X Channel.

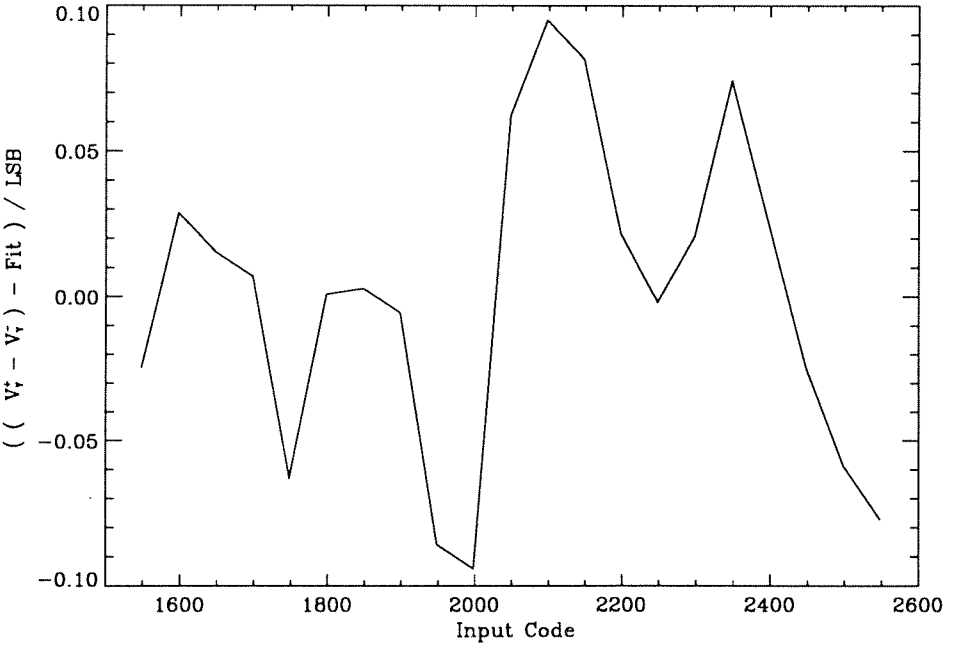

FIGURE 2.6 Error Assessment for the High Voltage Amplifier, Y Channel.

Thus the STM scan grid is square within $10^{-4}\%$.

2.4 High Voltage Amplifier, Z Channel

In normal STM operation, the Digital Signal Processing computer (DSP) senses the tunneling signal every 10 μs, computes the necessary correction to the piezoceramic tube length so as to keep the tunneling distance constant and outputs it to the Z electrode of the actuator via a 16 bit D-to-A and high voltage amplifier. There is thus a one-to-one relationship between the DSP binary code corresponding to a given correction, a binary number between 0 and 2^{16} (65636), and the voltage to which the Z electrode of the tube is submitted. The tube extension is linear with voltage, so that a height measurement at a given point may be performed by simply recording the corresponding voltage correction V_Z. However, if the D-to-A and amplifier combination induces a linear relation between its input code and output voltage, measuring V_Z is strictly equivalent to storing its code value, which is much more convenient and actually the way the STM acquires data. Therefore, to validate the STM profile measurements it is necessary to investigate the linearity of the D-to-A/amplifier system.

The calibration was performed by recording V_Z for various DSP generated codes ranging from 0 to $2^{16} - 1$ (65535). This operation was repeated for each different Z gain of the amplifier. Figure 2.7 presents the calibration results only for the maximum gain (6.4) which is used throughout this work. A straight line is fitted to the data and the 16 bit D-to-A LSB can be expressed in terms of voltage as

$$1 \text{ LSB } = 5.67 \times 10^{-4} \ V. \tag{2.4.1}$$

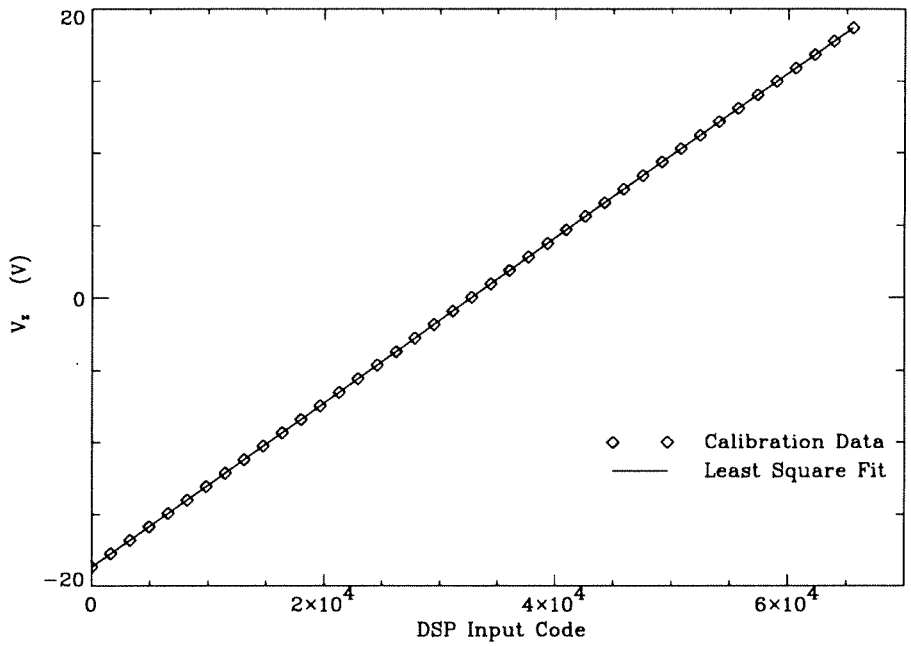

FIGURE 2.7 Calibration of the High Voltage Amplifier, Z Channel.

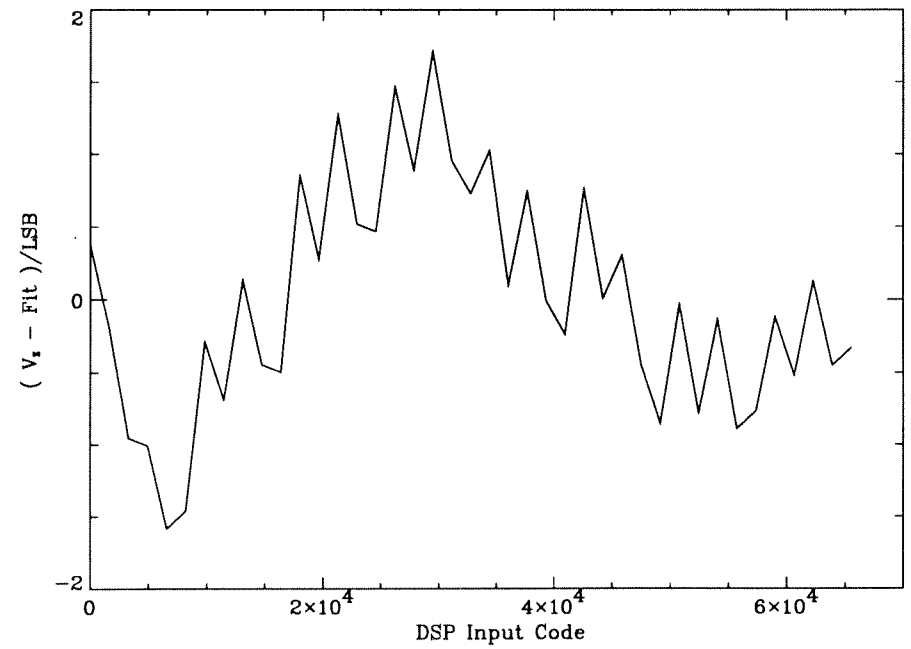

FIGURE 2.8 Error Assessment for the High Voltage Amplifier, Z Channel.

The deviation of the D-to-A from linearity may then be computed as the fit error in Volts normalized by 1 LSB expressed in Volts as well and is presented in Figure 2.8. From this analysis, it appears that the electronics behave linearly within $\pm$ 2 LSB. In other words, the 16 bit D-to-A actually acts as a true 14 bit D-to-A.

The discussion above deals with the systematic error in the D-to-A and amplifier system. The random electrical noise should also be taken into account. It is very difficult to assess the effect of such noise directly. Under good tunneling conditions it was observed that the steady-state tunneling signal was stable enough so as to induce corrections in the DSP output signal amounting to less than 5 mV or 8 LSB. If these observations reflect the effect of random noise, the 16 bit D-to-A should be downgraded to 13 true bit and consequently the error in height measurement should be estimated at $\pm$ 4 LSB. The translation from LSB units to meters depends on the piezoelectric properties of the tube which are determined in the next section.

2.5 Piezoceramic Tube Calibration

In the previous section, it was shown that the electronics controlling the tip position behave linearly. The deviation from linearity led to the computation of errors which characterize the STM resolution assuming that the deformation of the piezoceramic tube is linear with excitation voltage. To conclude the full calibration of the apparatus, one needs to investigate the validity of this assumption and quantified the sensitivity of the actuator.

2.5.1 Tube Hysteresis

The controlling parameter in the contraction/expansion (Z axis) or bending (X-Y axis) of the piezoceramic actuator is the piezoelectric charge constant d_{31} as shown in

equation 1.2.1 and 1.2.2. The common assumption for piezoceramic materials is that d_{31} is a constant. Actually, it is not and exhibits a hysteresis type dependence on the excitation voltage as illustrated in Figure 2.9 (a). Consequently, the deformation of a piezoelectric material is not quite linear with voltage either (see Figure 2.9 (b)). However, within the hysteresis loop, there are linear segments and for accurate measurements, the STM tube needs to run in these linear regimes. For even higher consistency, the STM should only work on a given leg ("upper" or "lower") of the hysteresis loop. This observation explains why the software programming of the STM data acquisition accommodates two sets of measurements for every scan recorded by the microscope, namely the forward and backward scans for which the Y excitation voltage is ramped up, and down, respectively.

Because the hysteresis originates in d_{31} which regulates the deformation of the tube along all three axes, it is not necessary to study the hysteresis for each independently. Rather, since the STM acquires two scans, each on one leg of the Y hysteresis loop, the non-linearity is assessed for that axis and assumed to be similar for the X and Z axis. As an example, Figure 2.10 presents the forward and backward scans of a PolyVinylChloride (PVC) specimen. Each contains 300×300 pixels or grid points for an in-plane excitation voltage ranging from $-90\ V$ to $+90\ V$ for both the X and Y axes. Close to the lower and upper boundaries of the scans, that is for the extremes of the Y hysteresis loop, differences or distortions in surface measurements are clearly visible upon careful comparison of the two two figure, but the center portions of each scan appear only translated with respect to each other. In such images, one can locate visually the position of specific topographic features in pixel coordinates, or Volt units, according to the tip positioning calibration. The differences in ordinates of the recorded location of the same object in both scans yields an immediate estimate of the width of hysteresis loop at that Y position. Such a result is presented in Figure 2.11.

Though the voltage range (-90 to $+90\ V$) is only a quarter of the STM maximum

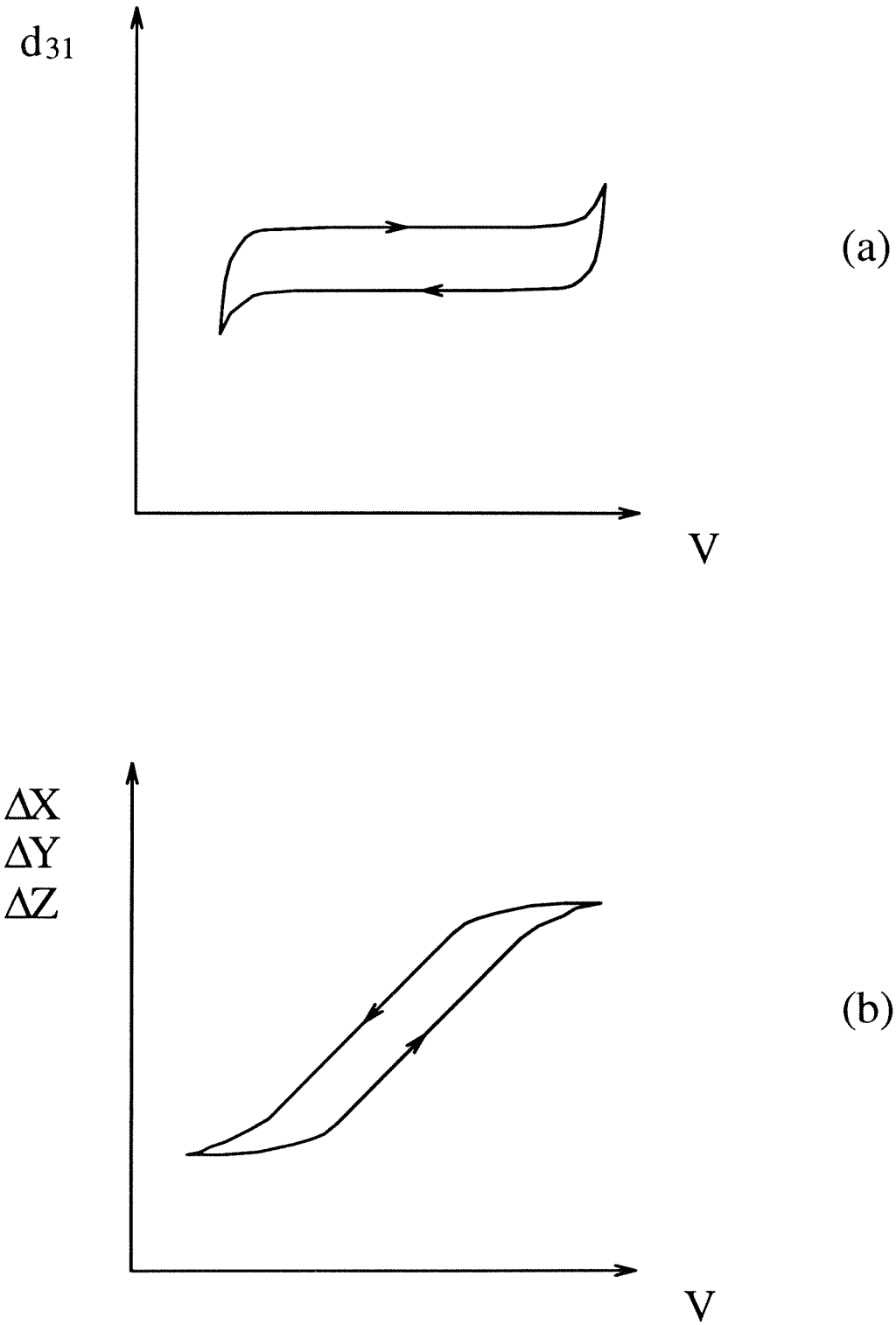

FIGURE 2.9 Theoretical Hysteresis Behavior of Piezoceramic Materials.

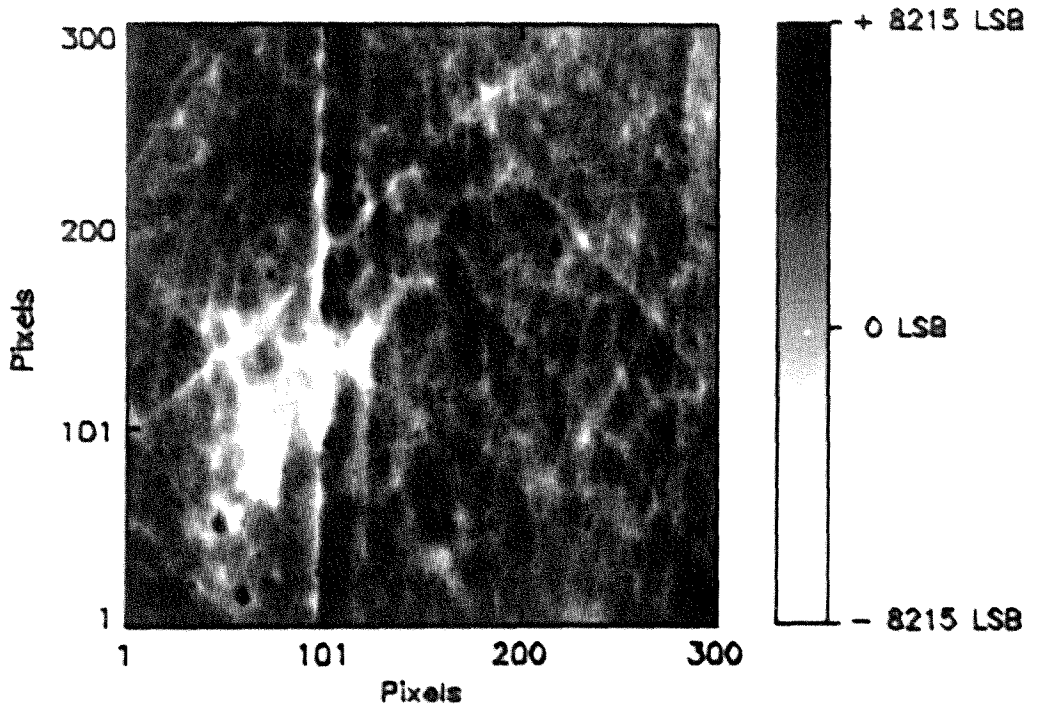

(a) Forward Scan of a PVC specimen

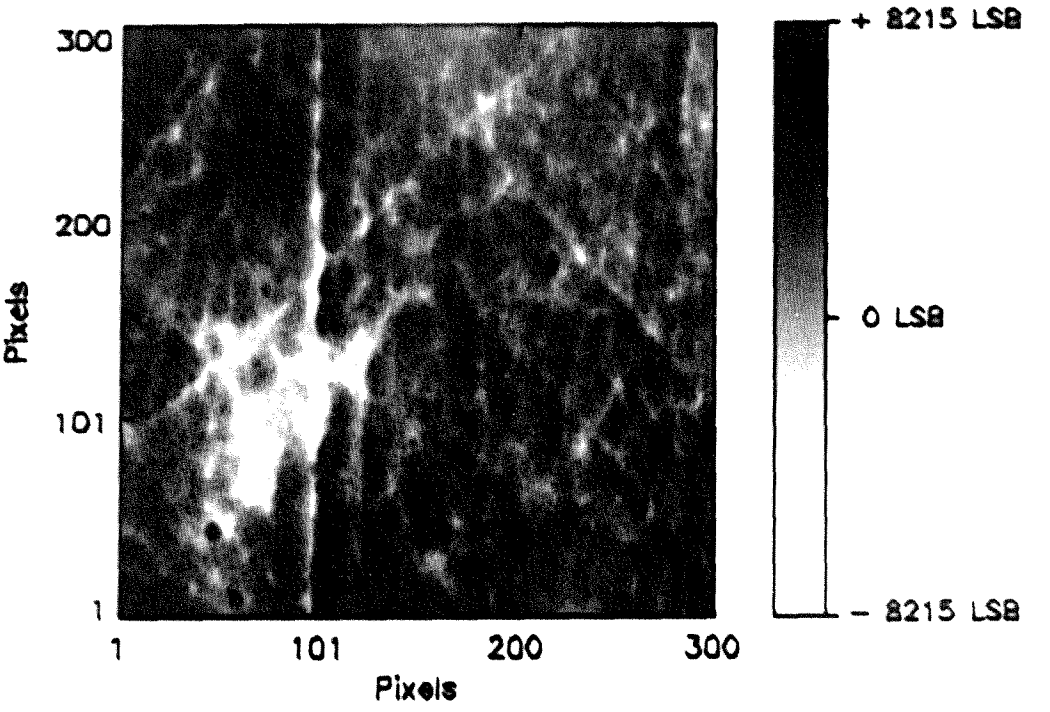

(b) Backward Scan of a PVC Specimen

FIGURE 2.10 Example of Hysteresis in Scans of a PVC Specimen.

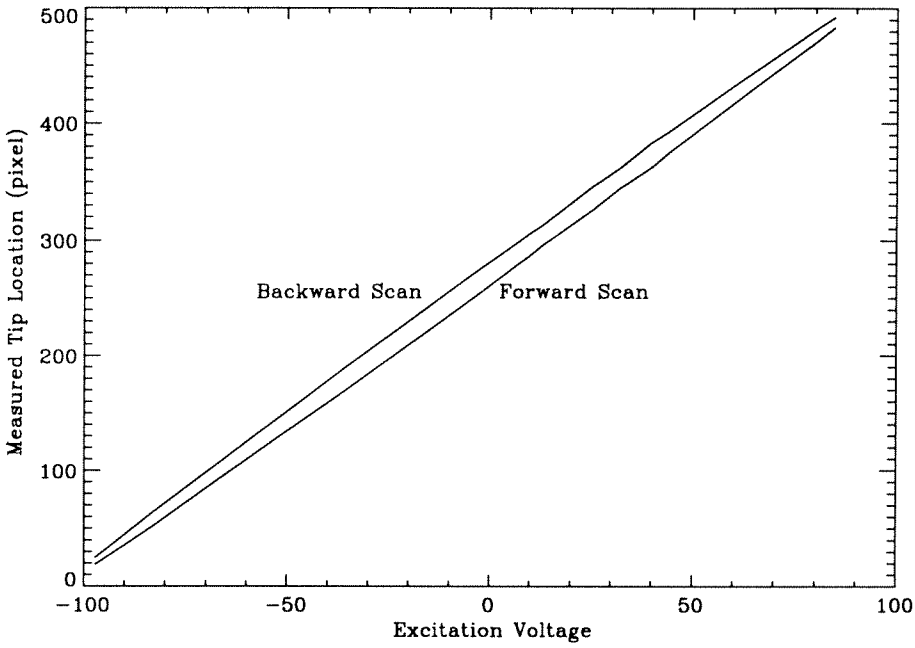

FIGURE 2.11 Hysteresis Measurement along the Y Axis of an STM Scan.

theoretical capabilities, the hysteresis loop is found to be already significant. However, the linearity of each leg between $-80\ V$ and $+80\ V$ is still within the experimental measurement error of $\pm\ 0.5\ pixel$.

It is very difficult to obtain more accurate hysteresis data than those just presented. Therefore it is assumed from this point on, that for a voltage excitation V such that $-80\ V\ <$ V $<\ +80\ V$, the piezoceramic tube behaves linearly. The actual error involved in that assumption is not directly assessed. However, later in this work, the resolution in displacement measurement by Digital Image Correlation of STM scans is determined. It will reflect not only the limitation of the numerical code but also the validity of the linearity postulate. In addition, it will include errors associated with X-Y coupling in the tip motion which are not discussed here.

2.5.2 Determination of the Tube Piezoelectric Properties

Now that a voltage range has been determined in which the piezoelectric properties of the tube are assumed constant, it is possible to obtain experimentally the sensitivity of the actuator to excitation voltage on the X-Y and Z electrodes.

a. *Theoretical Analysis*

This calibration is performed by scanning a mechanically etched diffraction grating. Such gratings have a periodic sawtooth pattern as shown in Figure 2.12.

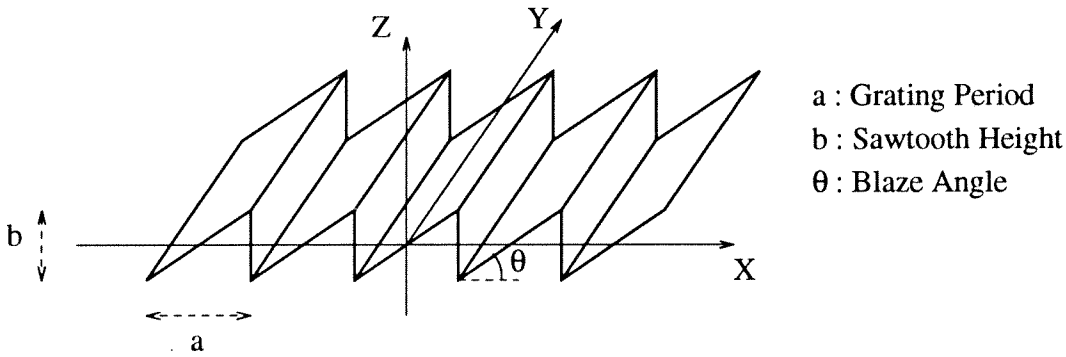

FIGURE 2.12 Sawtooth Pattern of a Diffraction Grating.

Let a be the period of the diffraction grating, b the sawtooth height and θ the blaze angle of the grating; then, in a XYZ reference frame such that the XY plane collapses onto the average plane of the grating and the Y axis is parallel to the grating grooves, the height h of the periodic pattern can be expressed as a function of the in-plane coordinates (x, y) over a period as

$$h(x,y) = tan\theta\, x \qquad x \in [-\frac{a}{2}, \frac{a}{2}], \forall y. \tag{2.5.1}$$

$h(x,y)$ can be decomposed in a Fourier serie along the X axis as

$$h(x,y) \;=\; c_0 \;+\; \sum_{n=1}^{\infty}\Big[\, c_n \, cos\frac{2n\pi x}{a} \;+\; d_n \, sin\frac{2n\pi x}{a} \,\Big], \tag{2.5.2}$$

where

$$\begin{cases} c_0 \;=\; \dfrac{1}{a}\displaystyle\int_{-\frac{a}{2}}^{\frac{a}{2}} h(x,y)\, dx \\ c_n \;=\; \dfrac{2}{a}\displaystyle\int_{-\frac{a}{2}}^{\frac{a}{2}} h(x,y)\, cos\frac{2n\pi x}{a}\, dx \qquad n \;>\; 0 \\ d_n \;=\; \dfrac{2}{a}\displaystyle\int_{-\frac{a}{2}}^{\frac{a}{2}} h(x,y)\, sin\frac{2n\pi x}{a}\, dx \qquad n \;>\; 0, \end{cases} \tag{2.5.3}$$

which yields

$$h(x,y) \;=\; \frac{b}{\pi}\sum_{n=1}^{\infty}\frac{(-1)^{n+1}}{n}\; sin\frac{2n\pi x}{a}\;. \tag{2.5.4}$$

Define $H(f_x, f_y)$, the Fourier transform of $h(x,y)$ as[e]

$$H(f_x,f_y) \;=\; \frac{1}{2\pi}\int_{-\infty}^{\infty}\int_{-\infty}^{\infty} h(x,y)e^{-2\pi i(f_x x \,+\, f_y y)}\, dxdy; \tag{2.5.5}$$

one then deduces $\big|H(f_x,f_y)\big|$ from equation (2.5.4) as

$$\big|H(f_x,f_y)\big| \;=\; \frac{b}{2\pi}\sum_{n=1}^{\infty}\frac{1}{n}\,\big|\delta(f_x \,+\frac{n}{a},f_y) \;-\; \delta(f_x \,-\frac{n}{a},f_y)\big|, \tag{2.5.6}$$

where $\delta(f_x,f_y)$ represents a delta function in the Fourier domain. Equation (2.5.6) means that the power spectrum of a topographic scan of a such a diffraction grating yields amplitude peaks in the Fourier domain located at harmonic frequencies of the grating frequency. It is this very characteristic on which the tube calibration procedure is based.

b. Experimental Procedure

Following the mathematical analysis, the experimental STM calibration procedure can be laid out in these steps :

---

[e] Definitions of the Fourier transform differ from one another by the scaling factor in front of the integral.

- Acquire a $n \times n$ pixel scan of a diffraction grating.
- Compute the scan power spectrum.
- Determine the frequency of the first harmonic peak in $pixel^{-1}$ from the power spectrum and equate it to the grating frequency to obtain the pixel size in meters.
- Measure the amplitude of the first harmonic peak in Z units of motion (LSB) and relate it to the theoretical height of the grating b to yield the Z-LSB size in meters.

Such a procedure is experimentally very convenient since it requires only one scan processed by a unique mathematical transformation to determine the tube actuator sensitivities (measured in volt per meter) for both in-plane and out-of-plane deformation. However some thought must be given in choosing the proper STM scan characteristics, the proper diffraction grating properties as well as the necessary data processing tools to conduct this calibration as accurately as possible.

The requirements on the STM scan characteristics are straightforward. First of all, the in-plane spatial resolution should be set at its minimum, meaning that the pixel size, or distance between neighboring scan grid points, should be as small as possible. In this digital machine where the in-plane tip motion is measured in LSB, the smallest pixel size is 1 LSB. On the other hand, the scan should be as large as practical in order to cover as many grating sawteeth as possible; the more sawteeth in the picture, the better their frequency can be measured. Total memory limitation in the PC restricts the scan size to 512×512 $pixels$. The size of the pixel in LSB and the width of the scan in $pixel$ fully define the voltage range V to which the tube needs to be submitted. According to equation (2.3.1)

$$-51\,V < \mathrm{V} < +51V, \tag{2.5.7}$$

which complies with the tube hysteresis limitation. The last parameter to be determined is the Z magnification. Ideally, the Z resolution should be set to a minimum, *i.e.*, the magnification should be maximized. However it is very difficult to ensure that a specimen lies perfectly perpendicularly to the tube axis. Consequently the Z range must be big enough to accommodate not only the roughness of the surface but also its probable tilt. For all calibration scans the lowest Z magnification was, therfore, used corresponding to a theoretical range of 600 nm according to manufacturing data. All other STM parameters were set at their standard values as discussed earlier. In summary, calibration scans were such that

- Size = 512 × 512 $pixels$
- In-Plane Excitation Voltage, $-51\ V\ <\ \mathrm{V}\ <\ 51V$
- Z gain = 6.4
- Z Excitation Voltage, $-18.67\ V\ <\ \mathrm{V}\ <\ 18.67V$
- Feedback Loop Gain, $K\ =\ 10^{-3}$
- Feedback Loop Frequency, $F_{FBL}\ =\ 100\ KHz$
- Acquisition Frequency, $F_{ACQ}\ =\ 400\ Hz$

The calibration grating must also be chosen with care. From manufacturing data, one estimates that the size of the calibration scan is 6.8 μm. In order to have at least one full grating groove in the scan, the grating pitch should be at least 150 $lines/mm$. In addition, the blaze angle should be steep enough for the sawtooth height to amount to a significant number of LSB but not too step to get into range problems. The final choice was made for a 1200 $lines/mm$ grating with a $10°22'$ blaze angle which translates into

Periodicity of the grating, $a\ =\ 833.33\ nm\ \pm\ 1.5\ nm$

Height of Grating Sawtooth, $b = 152.34\ nm \pm 0.5\ nm$

The error estimates were provided by the grating manufacturer.[28] To avoid surface oxides and to ensure good electrical conduction, a 40 nm thick gold-palladium coating was deposited on the grating.

Finally, there are three data processing issues which need to be addressed before presenting the calibration results. First, when a specimen is positioned under the STM, it is likely that its surface will not be orthogonal to the tube axis. The topographic measurements then reflects both the surface roughness and the deviation from normality. Therefore, a least square plane is fitted through every scan and subtracted from it to yield a tilt-corrected image. The processed data set has a zero height average which complies to the previously formulated mathematical analysis.[f] Also, the grating grooves are not likely to be aligned with the scan axis as was assumed in the theoretical discussion of the calibration. Therefore, the first harmonic of the scan power spectrum will lie in the Fourier plane at the position (f_x, f_y). However, a rotation in the spatial domain is equivalent to the same rotation in the Fourier domain, and the physical frequency corresponding to position (f_x, f_y) is

$$f = \sqrt{f_x^2 + f_y^2}\,. \tag{2.5.8}$$

The last issue at hand is the actual computation of the first harmonic peak frequency and amplitude. Fast Fourier transform type algorithms are not adequate since they compute the power spectrum at discrete frequencies that may not coincide with the grating frequency. Instead, the exact Fourier integral

$$H(f_x, f_y) = \frac{1}{2\pi} \int_{-\infty}^{\infty} \int_{-\infty}^{\infty} h(x,y) e^{-2\pi i (f_x x + f_y y)}\, dx dy \tag{2.5.9}$$

---

[f] A non-zero average would only induce an additional delta function at location $(0,0)$ in the Fourier domain.

was evaluated for very finely spaced values of f_x and f_y in the Fourier domain (frequency increment of $1.56 \times 10^{-5}\ pixel^{-1}$). The position of the first harmonic is the set of (f_x, f_y) that maximizes $\left|H(f_x, f_y)\right|$.

c. Calibration Results

Two calibrations were performed. Figure 2.13 (a) presents one of the STM calibration scans while Figure 2.13 (b) displays a zoom of the scan power spectrum. There are obvious irregularities in the sawtooth pattern but the size scale of these defects is small compared to the groove period. Consequently, these local distortions will only affect the high frequency content of the Fourier transform, leaving the first harmonic peak unaffected. Indeed the various low frequency delta functions in the power spectrum are very clearly defined. The in-plane calibration results are presented in Table 1.

Calibration Run	1^{st} Harmonic Frequency $(pixel^{-1})$	Pixel Size (or LSB)
Calibration #1	$1.218 \times 10^{-2} \pm 4 \times 10^{-5}$	$10.15\ nm \pm 0.05\ nm$
Calibration #2	$1.220 \times 10^{-2} \pm 4 \times 10^{-5}$	$10.16\ nm \pm 0.05\ nm$

Table 1 In-Plane Calibration Results.

The error estimate for the first harmonic frequency is the result of the numerical Fourier transform scheme, but the uncertainty in the pixel size reflects both the numerical error as well as the grating accuracy. It is physically meaningless to speak in this context about an error of $0.05\ nm$ and it should be regarded as a statistical error.

The corresponding out-of-plane calibration is given in Table 2.

Calibration Run	1^{st} Harmonic Peak Amplitude (LSB)	LSB Size Along the Z Axis
Calibration #1	2935.85	$8.26 \times 10^{-3}\ nm$
Calibration #2	2778.66	$8.72 \times 10^{-3}\ nm$

Table 2 Out-of-Plane Calibration results.

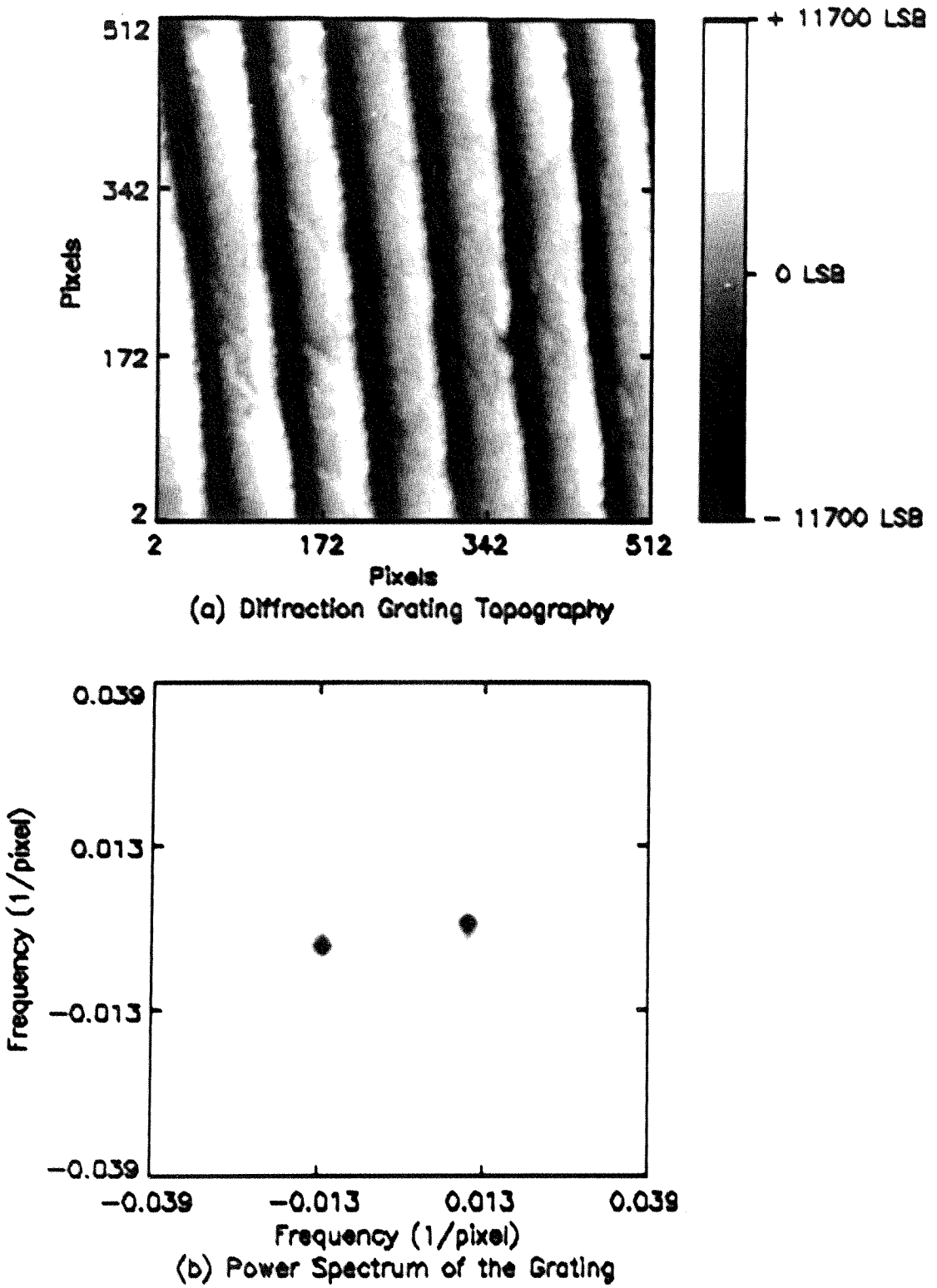

FIGURE 2.13 Calibration Scan of a Diffraction Grating and Corresponding Power Spectrum.

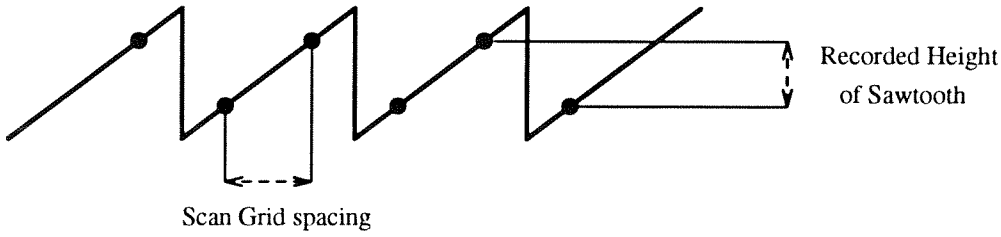

FIGURE 2.14 Sampling Error in Scan Acquisition.

The computation of the error here is more complicated than it was for the in-plane calibration. It is mainly related to sampling errors during scan acquisition. As is illustrated in Figure 2.14, the recorded sawtooth height may underestimate the actual grating step because the scan grid point may not be located at the highest and lowest position of the pattern. Therefore, the higher the first amplitude peak is, the better defined is the sawtooth in the corresponding scan. Moreover, if a delta function is mathematically sharp, experimentally it is blunted and the theoretical amplitude cannot quite be recovered. The error which results from these two problems is very difficult to assess. Consequently, it was decided to only consider the first calibration, which yielded the highest peak amplitude, as valid, associated with a conservative 5% error bar. The resolution of the STM in height measurement may now be evaluated. It was shown during the calibration of the Z-axis electronics that the uncertainty in a topographic record is $\pm$ 4 LSB. Therefore, the resolution of the STM is 8 LSB or 6.6×10^{-2} nm. In summary, the final calibration figures establish the following characteristics

1 X or Y Least Significant Bit = 10.15 nm to within 1%,

1 Z Least Significant Bit = 8.26×10^{-3} nm to within 5%,

Resolution in Height Measurement = 6.6×10^{-2} nm.

It is important to note that the size of the error bars in both the in-plane and out-of-plane calibration of the tube actuator do not represent a measure of the accuracy of the STM but rather the limitation of the calibration procedure.

2.6 Load Cell Calibration

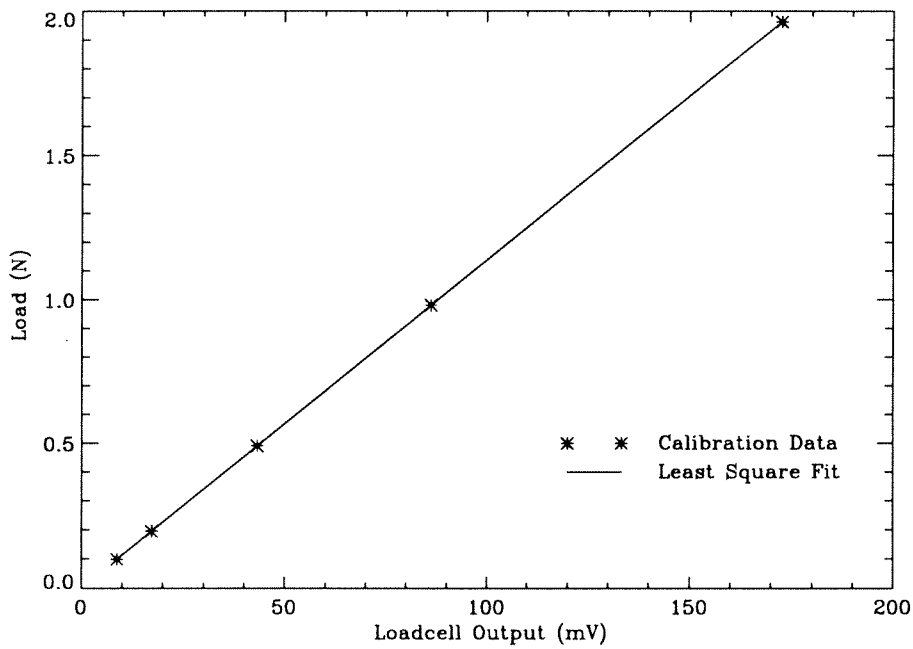

FIGURE 2.15 Load Cell Calibration.

Even though the load cell used in this work is very accurate and comes with calibration data from the manufacturer, it was thought necessary to check it in its standard setting as connected to its custom designed amplifier. In regular operation, the amplifier output is connected to a high precision digital voltmeter which oversamples the loadcell signal and displays it every second. This oversampling and subsequent averaging process takes care of high frequency noise and reduces the signal fluctuations to 0.5 mV. According to the manufacturer's data, such a noise level corresponds to a load uncertainty of 6×10^{-3} N. Therefore to assess the accuracy of the load cell/amplifier assembly, the load applied to

the load cell should be known to within 6×10^{-3} N or roughly 0.5 g. The calibration was performed by hanging dead weights on the load cell and recording the subsequent amplified signal on the digital voltmeter. Each weight was independently measured on a high accuracy scale to within 10^{-3} g[g]. Before the measurement, the load cell amplifier was zeroed out and its gain was adjusted to output 1792.2 mV for the shunt resistance within the amplifier. The calibration results are presented in Figure 2.15. A straight line fitted through the data leads to the relation

$$\text{Load } (N) \;=\; 1.1374 \times 10^{-2} \text{ Loadcell Output } (mV) \;-\; 3.1 \times 10^{-4} \;. \qquad (2.6.1)$$

The standard deviation for the fit was found to be 8.9×10^{-4} N, well within the 6×10^{-3} N due to electrical noise.

---

[g] The scale is limited to 200 g which explains why the maximum load in the calibration is only 2 N.

CHAPTER 3

Digital Image Correlation

Experimental methods in solid mechanics rely heavily on surface displacement measurements. To that end, many optical methods have been developed such as high resolution Moiré[29] , CGS[30]... Recently, a new technique has been proposed which states that a 2-D correlation method using white or laser speckle may be applied to obtain deformation of a body by comparing digital images of its surface in a undeformed and deformed configuration.[31-44] This technique has demonstrated good flexibility and accuracy. Investigations have even been pursued to extend the method to measure 3-D displacement field through stereo imaging.[45] Even more recently, digital images acquired by a Scanning Electron Microscope have allowed for very high resolution ($\approx$ 1 μm) measurements.[46,47] However, in this latter case, the computations were limited to 2-D (in-plane) displacement field and the Fourier based correlation algorithm required strong smoothing of the results precluding the observation of eventual inhomogeneities in the displacement field at the submicron level. If the two images were surface scans, obtained through a Scanning Tunneling Microscope (STM), the spatial resolution could be increased to 10 nm and using this correlation technique in-plane displacement and strains could be measured. Moreover, since the images are surface topographies, out-of-plane displacements could also be computed with very high accuracy (to within 5 nm).

To that end, a computer program was written which applies Digital Image Correlation for in-plane and out-of-plane displacement and displacement gradient measurements. A brief theoretical review of the technique as well as its numerical implementation is presented next.

3.1 Theoretical Considerations

A surface profile, as obtained by a Scanning Tunneling Microscope, is simply a discrete record of the "height" of the surface at grid points on a specimen surface, the sampling interval being typically on the order of 10 nm. Let $f(x,y)$ represent the surface profile of a specimen in an undeformed state at position (x,y), and $g(\widetilde{x},\widetilde{y})$ the surface profile after deformation at position $(\widetilde{x},\widetilde{y})$. If one assumes that the profile pattern before deformation is uniquely related to the profile pattern after deformation, then this suggests a correlation of these two patterns to detect the profile difference that is the object deformation. It is assumed henceforth that the deformation is in-plane, *i.e.*, height of characteristic features are preserved throughout the deformation.

3.2 The Image Correlation Technique

Let G be a point of coordinate (x,y) in the undeformed configuration. The height of the profile at G is $f(x,y)$. Similarly let $\widetilde{G}$ be a point with coordinates $(\widetilde{x},\widetilde{y})$ in the deformed configuration.

Based on the assumption about the deformation process, let χ be the mapping from the undeformed to the deformed configuration,

$$\begin{aligned} &\chi : \mathbb{R}^2 \rightarrow \mathbb{R}^2 \\ &\quad G \rightarrow \widetilde{G} = \chi(G) \text{ such that } g(\widetilde{x},\widetilde{y}) = f(x,y). \end{aligned} \tag{3.2.1}$$

Relation (3.2.1), expressed in terms of coordinates (x,y) and $(\widetilde{x},\widetilde{y})$ of G and $\widetilde{G}$ respectively, can be rewritten as

$$\begin{cases} \widetilde{x} = x + u(x,y) \\ \widetilde{y} = y + v(x,y) \end{cases} \tag{3.2.2}$$

where u and v are the in-plane displacement components of G.

Let $\widetilde{G}_0$ of coordinate $(\widetilde{x}_0, \widetilde{y}_0)$ be the image of G_0 through χ. Let S be a subset around point G_0 and $\widetilde{S}$ be a subset around $\widetilde{G}_0$, the image of S through χ. Assuming S to be small enough, equation (3.2.2) can be rewritten as

$$\forall\ \widetilde{G}(\widetilde{x},\widetilde{y}), \exists\ G(x,y) \text{ such that}$$

$$\begin{cases} \widetilde{x} = x + u(x_0,y_0) + \dfrac{\partial u}{\partial x}|_{(x_0,y_0)}(x-x_0) + \dfrac{\partial u}{\partial y}|_{(x_0,y_0)}(y-y_0) \\ \widetilde{y} = y + v(x_0,y_0) + \dfrac{\partial v}{\partial x}|_{(x_0,y_0)}(x-x_0) + \dfrac{\partial v}{\partial y}|_{(x_0,y_0)}(y-y_0). \end{cases} \tag{3.2.3}$$

Relation (3.2.3) defines a local mapping χ_l, the linearization of χ around G_0. Define a correlation coefficient C such as

$$C = \frac{\iint_S (f(G) - g(\chi_l(G)))^2\, dS}{\iint_S f^2(G)\, dS} \quad \text{, Least square coefficient}$$

or

$$C = 1 - \frac{\iint_S f(G) g(\chi_l(G))\, dS}{\left[\iint_S f^2(G)\, dS \iint_S g^2(\chi_l(G))\, dS\right]^{\frac{1}{2}}} \quad \text{, Cross correlation coefficient.} \tag{3.2.4}$$

It is easy to see that C will be zero if the coefficients of the mapping χ_l are exact. These coefficients are

$$\begin{aligned} u_0 &= u(x_0,y_0) & v_0 &= v(x_0,y_0) \\ u_{0,x} &= \frac{\partial u}{\partial x}|_{(x_0,y_0)} & v_{0,x} &= \frac{\partial v}{\partial x}|_{(x_0,y_0)} \\ u_{0,y} &= \frac{\partial u}{\partial y}|_{(x_0,y_0)} & v_{0,y} &= \frac{\partial v}{\partial y}|_{(x_0,y_0)}. \end{aligned} \tag{3.2.5}$$

The image correlation technique relies on the proposition that the set of coefficients minimizing C are indeed the displacements and the displacement derivatives at G_0.

Relation (3.2.4) is inappropriate when f and g are discrete sets of data. The integral sign in (3.2.4) is to be replaced by a sum sign over the grid points G_S contained in S,

$$\begin{cases} C = \dfrac{\sum_{G_S \in S} (f(G_S) - g(\chi_l(G_S)))^2}{\sum_{G_S \in S} f^2(G_S)} \\ \\ C = 1 - \dfrac{\sum_{G_S \in S} f(G_S) g(\chi_l(G_S))}{\left[\sum_{G_S \in S} f^2(G_S) \sum_{G_S \in S} g^2(\chi_l(G_S))\right]^{\frac{1}{2}}} \end{cases} . \tag{3.2.6}$$

The approach presented above should yield the in-plane displacement and displacement derivatives at a given point G_0. Since STM scans represent surface topographies, one should be able to extract the out-of-plane displacement component as well. There are two ways of obtaining this information.

The first solution involves invoking the 2-D correlation method, as described above. Once the displacement component (u_0, v_0) at point G_0 are known, the out-of-plane displacement w_0 can be computed as

$$w_0 = g(\widetilde{x} = x_0 + u_0 \, , \, \widetilde{y} = y_0 + v_0) - f(x_0 \, , \, y_0). \tag{3.2.7}$$

This scheme is very straight forward. However it is also likely to be the most error sensitive : the gradients of g may be locally large and thus a small imprecision in u_0 and v_0 could induce large errors in w_0.

The second approach tries to compute w_0 by involving it into the computation of the correlation coefficient C and then minimizing C not only with respect to the six in-plane parameters but also with respect to w_0. This could be accomplished for any definition of a correlation coefficient; however, because of programming considerations, this technique was only used for the least square coefficient which can be written as

$$C = \frac{\sum_{G_S \in S} (f(G_S) - (g(\chi_l(G_S)) - w_0))^2}{\sum_{G_S \in S} f^2(G_S)}. \tag{3.2.8}$$

In equation (3.2.8), w_0 appears now as a global offset in "height" between the two scans and assuming the dimension of subset S to be small, it should approximate the out-of-plane displacement component at G_0.

Finally, it should be noted that since G_S is a grid point in the undeformed configuration, $f(G_S)$ is defined. On the other hand, $\widetilde{G} = \chi_l(G_S)$ may not be at a grid point in the deformed configuration. Consequently interpolations over the deformed field are necessary so that $g(\widetilde{G})$ is defined for any $\widetilde{G}$ in the deformed field.

3.3 Numerical Method

The numerical implementation of this displacement measurement technique consists of two main parts. First, an interpolation scheme was programmed to evaluate the surface height at non-grid points in the deformed topographies. Further, a second-order optimization method was devised to minimize the least square correlation coefficient with respect to the mapping parameters, namely u_0, v_0, $u_{0,x}$, $v_{0,y}$, $u_{0,y}$, $v_{0,x}$ and w_0.

3.3.1 Interpolation Scheme

The Digital Image Correlation code was initially implemented with a bilinear interpolation scheme. However, the lack of C^1 continuity of this method was detrimental to the convergence properties of the overall displacement measurement technique, especially for rough topographic profiles. Therefore, a third-degree polynomial interpolation often referred to as the bicubic spline interpolation was considered, ensuring the continuity of the topographic in-plane derivatives. This yielded

$$\begin{aligned} g(\widetilde{x},\widetilde{y}) =& \alpha_{11} + \alpha_{12}\widetilde{y} + \alpha_{13}\widetilde{y}^2 + \alpha_{14}\widetilde{y}^3 \\ &+\alpha_{21}\widetilde{x} + \alpha_{22}\widetilde{x}\widetilde{y} + \alpha_{23}\widetilde{x}\widetilde{y}^2 + \alpha_{24}\widetilde{x}\widetilde{y}^3 \\ &+\alpha_{31}\widetilde{x}^2 + \alpha_{32}\widetilde{x}^2\widetilde{y} + \alpha_{33}\widetilde{x}^2\widetilde{y}^2 + \alpha_{34}\widetilde{x}^2\widetilde{y}^3 \\ &+\alpha_{41}\widetilde{x}^3 + \alpha_{42}\widetilde{x}^3\widetilde{y} + \alpha_{43}\widetilde{x}^3\widetilde{y}^2 + \alpha_{44}\widetilde{x}^3\widetilde{y}^3. \end{aligned} \tag{3.3.1}$$

The higher computational cost of this method is offset by the subsequent faster convergence rate of the optimization scheme[h].

3.3.2 Optimization Scheme

The most important feature of the correlation scheme is the minimization of C in equation (3.2.8) with respect to the mapping parameters of χ_l, namely u_0, v_0, $u_{0,x}$, $v_{0,y}$, $u_{0,y}$, $v_{0,x}$ and the out-of-plane component w_0. Let these seven quantities define a seven-dimensional space D such that

$$D = \left\{ P \in \mathbb{R}^7 \mid P(u, v, u_x, v_y, u_y, v_x, w) \right\}. \tag{3.3.2}$$

So, if P is the unknown vector, the mapping χ_l can be considered to be a function of P and, through χ_l in (3.2.8), $C = C(P)$, that is

$$C(P) = \frac{\sum_{G_S \in S} (f(G_S) - \tilde{g}(G_S, P))^2}{\sum_{G_p \in S} f^2(G_p)} \tag{3.3.3}$$

where

$$\tilde{g}(G_S, P) = g(\chi_l(G_S)) - w. \tag{3.3.4}$$

Let P_0 be a vector in D and let P be the vector solution of the minimization problem. Writing $C(P)$ as a truncated Taylor series around P_0 leads to

$$C(P) = C(P_0) + \nabla C(P_0)^T (P - P_0) + \frac{1}{2}(P - P_0)^T \nabla\nabla C(P_0)(P - P_0)\,. \tag{3.3.5}$$

Since P defines a minimum, $\nabla C(P) = 0$. Consequently, taking the gradient of (3.3.5) yields

$$\nabla\nabla C(P_0)(P - P_0) = -\nabla C(P_0). \tag{3.3.6}$$

---

[h] The interpolation programming was based on IMSL subroutines.

Solving for P iteratively from equation (3.3.6) will converge to the solution of the minimization problem. This scheme, called the Newton-Raphson optimization method, may be computer intensive since it requires the knowledge of $\nabla\nabla C(P)$, the Hessian matrix of C at P, defined as

$$\nabla\nabla C(P) = \left(\frac{\partial^2 C}{\partial P_i \partial P_j}\right)_{i=1,7;j=1,7}. \tag{3.3.7}$$

However, if C is chosen according to (3.2.8), it may only be necessary to compute ∇C, that is the first derivatives of C with respect to P. Indeed, the gradient of C with respect to P is

$$\nabla(C) = \left(\frac{\partial C}{\partial P_i}\right)_{i=1,7} \tag{3.3.8}$$

and from (3.3.3), we have

$$\frac{\partial C}{\partial P_i} = -\frac{2}{\sum_{G_S \in S} f^2(G_S)} \sum_{G_S \in S} (f(G_S) - \tilde{g}(G_S, P))) \frac{\partial \tilde{g}(G_S, P)}{\partial P_i}. \tag{3.3.9}$$

Upon taking another derivative, Hessian matrix terms are obtained as

$$\begin{aligned} \frac{\partial^2 C}{\partial P_i \partial P_j} = & -\frac{2}{\sum_{G_S \in S} f^2(G_S)} \sum_{G_S \in S} (f(G_S) - \tilde{g}(G_S, P)) \frac{\partial^2 \tilde{g}(G_S, P)}{\partial P_i \partial P_j} \\ & + \frac{2}{\sum_{G_S \in S} f^2(G_S)} \sum_{G_S \in S} \frac{\partial \tilde{g}(G_S, P)}{\partial P_i} \frac{\partial \tilde{g}(G_S, P)}{\partial P_j}. \end{aligned} \tag{3.3.10}$$

Equation (3.3.10) gives an exact formulation of the Hessian matrix of C at P. However (3.3.10) can be approximated when P is close to the exact solution[48] . In that case

$$\tilde{g}(G_S, P) \approx f(G_S) \tag{3.3.11}$$

and therefore

$$\frac{\partial^2 C}{\partial P_i \partial P_j} \approx \frac{2}{\sum_{G_S \in S} f^2(G_S)} \sum_{G_S \in S} \frac{\partial \tilde{g}(G_S, P)}{\partial P_i} \frac{\partial \tilde{g}(G_S, P)}{\partial P_j}. \tag{3.3.12}$$

This approximation in the calculation of the Hessian matrix makes the method easy to implement, especially since equation (3.3.12) involves terms such as $\frac{\partial \widetilde{g}(G_S,P)}{\partial P_i}$ which are now very simple to obtain.Through the bicubic spline interpolation, $\widetilde{g}(G_S,P)$ can be written as

$$\begin{aligned}\widetilde{g}(G_S,P) =& g(\widetilde{x},\widetilde{y}) - w \\ =& \alpha_{11} + \alpha_{12}\widetilde{y} + \alpha_{13}\widetilde{y}^2 + \alpha_{14}\widetilde{y}^3 \\ &+\alpha_{21}\widetilde{x} + \alpha_{22}\widetilde{x}\widetilde{y} + \alpha_{23}\widetilde{x}\widetilde{y}^2 + \alpha_{24}\widetilde{x}\widetilde{y}^3 \\ &+\alpha_{31}\widetilde{x}^2 + \alpha_{32}\widetilde{x}^2\widetilde{y} + \alpha_{33}\widetilde{x}^2\widetilde{y}^2 + \alpha_{34}\widetilde{x}^2\widetilde{y}^3 \\ &+\alpha_{41}\widetilde{x}^3 + \alpha_{42}\widetilde{x}^3\widetilde{y} + \alpha_{43}\widetilde{x}^3\widetilde{y}^2 + \alpha_{44}\widetilde{x}^3\widetilde{y}^3 - w.\end{aligned} \tag{3.3.13}$$

The relation between $\widetilde{x}$, $\widetilde{y}$, x, and y is

$$\begin{cases} \widetilde{x} = x_0 + \overline{x} + P_1 + P_3\overline{x} + P_5\overline{y} \\ \widetilde{y} = y_0 + \overline{y} + P_2 + P_4\overline{y} + P_6\overline{x}, \end{cases} \tag{3.3.14}$$

with

$$\begin{cases} \overline{x} = x - x_0 \\ \overline{y} = y - y_0, \end{cases} \tag{3.3.15}$$

so that, finally, the various terms $\frac{\partial \widetilde{g}(G_S,P)}{\partial P_i}$ may be calculated as

$$\left.\begin{aligned}
\frac{\partial \widetilde{g}(G_S,P)}{\partial P_1} &= \frac{\partial \widetilde{g}(G_S,P)}{\partial \widetilde{x}}\frac{\partial \widetilde{x}}{\partial P_1} + \frac{\partial \widetilde{g}(G_S,P)}{\partial \widetilde{y}}\frac{\partial \widetilde{y}}{\partial P_1} = \frac{\partial \widetilde{g}(G_S,P)}{\partial \widetilde{x}} \\
\frac{\partial \widetilde{g}(G_S,P)}{\partial P_2} &= \frac{\partial \widetilde{g}(G_S,P)}{\partial \widetilde{x}}\frac{\partial \widetilde{x}}{\partial P_2} + \frac{\partial \widetilde{g}(G_S,P)}{\partial \widetilde{y}}\frac{\partial \widetilde{y}}{\partial P_2} = \frac{\partial \widetilde{g}(G_S,P)}{\partial \widetilde{y}} \\
\frac{\partial \widetilde{g}(G_S,P)}{\partial P_3} &= \frac{\partial \widetilde{g}(G_S,P)}{\partial \widetilde{x}}\frac{\partial \widetilde{x}}{\partial P_3} + \frac{\partial \widetilde{g}(G_S,P)}{\partial \widetilde{y}}\frac{\partial \widetilde{y}}{\partial P_3} = \overline{x}\frac{\partial \widetilde{g}(G_S,P)}{\partial \widetilde{x}} \\
\frac{\partial \widetilde{g}(G_S,P)}{\partial P_4} &= \frac{\partial \widetilde{g}(G_S,P)}{\partial \widetilde{x}}\frac{\partial \widetilde{x}}{\partial P_4} + \frac{\partial \widetilde{g}(G_S,P)}{\partial \widetilde{y}}\frac{\partial \widetilde{y}}{\partial P_4} = \overline{y}\frac{\partial \widetilde{g}(G_S,P)}{\partial \widetilde{y}} \\
\frac{\partial \widetilde{g}(G_S,P)}{\partial P_5} &= \frac{\partial \widetilde{g}(G_S,P)}{\partial \widetilde{x}}\frac{\partial \widetilde{x}}{\partial P_5} + \frac{\partial \widetilde{g}(G_S,P)}{\partial \widetilde{y}}\frac{\partial \widetilde{y}}{\partial P_5} = \overline{y}\frac{\partial \widetilde{g}(G_S,P)}{\partial \widetilde{x}} \\
\frac{\partial \widetilde{g}(G_S,P)}{\partial P_6} &= \frac{\partial \widetilde{g}(G_S,P)}{\partial \widetilde{x}}\frac{\partial \widetilde{x}}{\partial P_6} + \frac{\partial \widetilde{g}(G_S,P)}{\partial \widetilde{y}}\frac{\partial \widetilde{y}}{\partial P_6} = \overline{x}\frac{\partial \widetilde{g}(G_S,P)}{\partial \widetilde{y}} \\
\frac{\partial \widetilde{g}(G_S,P)}{\partial P_7} &= \frac{\partial \widetilde{g}(G_S,P)}{\partial \widetilde{x}}\frac{\partial \widetilde{x}}{\partial P_7} + \frac{\partial \widetilde{g}(G_S,P)}{\partial \widetilde{y}}\frac{\partial \widetilde{y}}{\partial P_7} = 1
\end{aligned}\right\}. \tag{3.3.16}$$

Derivatives of $\widetilde{g}(G_S, P)$ with respect to $\widetilde{x}$ or $\widetilde{y}$ are easily computed from (3.3.13).

This minimization method depends on the starting point P_0. Before executing this calculation, a coarse optimization scheme determines therefore an initial guess : the displacement derivatives and out-of-plane displacement are set to zero and all possible integer values of u_0, v_0 within a given range are tried. The set $(u_0, v_0, 0, 0, 0, 0, 0)$ that produces the lowest correlation coefficient is then used as the starting guess for the optimization procedure.

3.4 Postprocessing

Comparing two images with Digital Image Correlation yields seven variables at preselected pixel locations in the reference image, namely u, v, w, u_x, u_y, v_x, v_y. These parameters define locally the mapping that brings the undeformed image to the deformed one. From these parameters, it is possible to extract the local in-plane strain at each computational point.

Earlier work on the method[37] has employed the small deformation theory framework to compute in-plane strains and the local rigid body rotation angle θ

$$\begin{cases} \epsilon = \frac{1}{2}(\nabla \mathbf{u} + \nabla \mathbf{u}^T) \\ \theta = \frac{1}{2}(\frac{\partial v}{\partial x} - \frac{\partial u}{\partial y}). \end{cases} \tag{3.4.1}$$

However preliminary tests of this code showed that when two images, differing only by a rigid body rotation of angle θ were compared, θ could only be deduced accurately for $\theta \leq 10°$, and, in addition that erroneous rotation-induced straining was observed. This inconsistency is implicit in the small deformation theory itself. To show this, let us assume that the deformed image is the result of a rigid body rotation of amount θ of the reference image around its origin; a point P of coordinate (x, y) in the undeformed

configuration is then mapped to $\widetilde{P}\ (\ \widetilde{x}, \widetilde{y}\ )$ in the deformed configuration according to

$$\begin{cases} \widetilde{x} \ = \ x\ cos\theta \ - \ y\ sin\theta \\ \\ \widetilde{y} \ = \ x\ sin\theta \ + \ y\ cos\theta. \end{cases} \tag{3.4.2}$$

Consequently, the resulting displacement components u and v are :

$$\begin{cases} u \ = \ \widetilde{x} \ - \ x \ = \ x\ (\ cos\theta \ - \ 1\ ) \ - \ y\ sin\theta \\ \\ v \ = \ \widetilde{y} \ - \ y \ = \ x\ sin\theta \ + \ y\ (\ cos\theta \ - \ 1\ ). \end{cases} \tag{3.4.3}$$

From u and v, the components of the strain tensor ϵ_{xx}, ϵ_{yy}, ϵ_{xy} as well as the theoretical rigid body rotation angle θ' can be computed as

$$\begin{aligned} \epsilon_{xx} \ &= \ \frac{\partial u}{\partial x} \ = \ cos\theta \ - \ 1 \\ \epsilon_{yy} \ &= \ \frac{\partial v}{\partial y} \ = \ cos\theta \ - \ 1 \\ \epsilon_{xy} \ &= \ \frac{1}{2}(\ \frac{\partial u}{\partial y} \ + \ \frac{\partial v}{\partial x}\ ) \ = \ 0 \\ \theta' \ &= \ \frac{1}{2}(\ \frac{\partial v}{\partial x} \ - \ \frac{\partial u}{\partial y}\ ) \ = \ sin\theta. \end{aligned} \tag{3.4.4}$$

If "θ is small enough" (small deformation theory), equation (3.4.4) becomes

$$\begin{aligned} \epsilon_{xx} \ &= \ O(\ \theta^2\ ) \\ \epsilon_{yy} \ &= \ O(\ \theta^2\ ) \\ \epsilon_{xy} \ &= \ 0 \\ \theta' \ &= \ \theta \ + \ O(\ \theta^3\ ). \end{aligned} \tag{3.4.5}$$

Thus, as long as $O(\ \theta^2\ )$ is below the resolution of the Digital Image Correlation code, processing its output in the small deformation theory framework will yield an accurate estimate for the local strain tensor components and rigid body rotation angle. It was found, however, that on good images the resolution in strain can be as low as 10^{-4} which means that rigid body rotation of the amount of 0.8° will induce a detectable (small deformation) strain. In other word, the "θ is small enough" statement translates for our purposes to "$\theta \ \ll \ 0.8°$ " to rightfully use the small deformation theory for processing the data.

It is experimentally very difficult to ensure that stretching a specimen will not induce a rigid body rotation of more than 0.8°. It was therefore decided to extract strain and rotation data from the correlation output by drawing on the large deformation theory. At every computational point, from u, v, u_x, u_y, v_x, v_y, the in-plane deformation tensor $\mathbf{F}$ and the Right Cauchy-Green tensor $\mathbf{C}$ are evaluated,

$$\begin{aligned} \mathbf{F} &= (\,\mathbf{1} + \nabla\mathbf{u}\,) \\ \mathbf{C} &= \mathbf{F}^T\mathbf{F}. \end{aligned} \tag{3.4.6}$$

The Lagrangian strain tensor γ is determined as

$$\gamma = \frac{1}{2}(\,\mathbf{C} - \mathbf{1}\,), \tag{3.4.7}$$

and the local rigid body deformation part of the deformation process $\mathbf{Q}$ may then be computed through the Polar Decomposition Theorem,

$$\mathbf{Q} = \mathbf{F}(\sqrt{\mathbf{C}})^{-1}. \tag{3.4.8}$$

In component form, $\mathbf{Q}$ can be written as

$$Q = \begin{pmatrix} cos\theta & -sin\theta \\ sin\theta & cos\theta \end{pmatrix} \tag{3.4.9}$$

and hence θ can be computed. On computer generated data, rigid body rotation angles as high as 80° between two images were successfully determined with less than 10^{-4} degree in absolute error without generating any "artificial" strain.

There is more to the accurate computation of θ than just extracting another deformation parameter from the comparison of two images, it is also essential to the proper and understandable representation of the displacement field. Indeed, if the mapping between the undeformed and deformed image is a combination of a deformation process superposed on some global rigid body rotation, whether legitimate or not, the in-plane displacement component will reflect both. Thus, if the deformation induced displacements

are small compared to the size of the image, rigid body rotation induced displacements will cloud the data. In this specific application, very small displacements are expected and supposedly no or very little rigid body rotation. It is therefore extremely important to extract accurately any meaningless rotation $\mathbf{Q}$ and to correct the data accordingly by ascribing the measured displacement to a rotation $\mathbf{Q}^{-1}$. The global rigid body rotation of a given deformation field is estimated by taking the average of the local rigid body rotation angle at every pixel location were computation was carried out. After postprocessing, the following data are then available at every preselected pixel location in the reference image,

u,v, in-plane displacement components corrected for rigid body rotation,

w, out-of-plane displacement component,

γ, in-plane components of the Lagrangian strain tensor.

In addition, some global field parameters are also computed,

$\overline{\theta}$, Average rigid body rotation angle,

$\overline{\gamma}$, Average in-plane component of the Lagrangian strain tensor,

α_1, α_2, Average principal axis direction, computed from $\overline{\gamma}$,

λ_1, λ_2, Average principal stretches, computed from $\overline{\gamma}$.

CHAPTER 4

Translation Experiments

The main objective of this whole work is the study of mechanical systems at the submicron scale. To that aim, the STM was built to acquire high resolution topographies of a specimen surface under some loading conditions. At this stage of the project, it is therefore necessary to extract from the different scans, the responses of the specimen to the various boundary conditions to which it is submitted. The Digital Image Correlation technique (DIC) was chosen for the task. Comparing two images of the same area of a specimen surface but under different loading conditions, this pattern recognition type algorithm computes the 3-D displacement field which maps one scan onto the other. How well this whole experimental scheme is suited to submicron mechanical studies depends solely on how well the DIC recovers local displacement fields. This chapter addresses this very question.

To test the performance of the technique, one needs to impose well defined changes in boundary conditions to the specimen for which the displacement responses are known and compare the subsequent experimental measurements to the theoretical ones. If the task at hand seems conceptually simple, experimentally it is not. At such a small scale continuum mechanics may not hold and therefore it is not possible to predict the material response to a change in loading conditions. Only transformations such as translations and rotations are acceptable since for those, the induced displacements do not depend on the material properties. On the other hand, the DIC is expected to have a subpixel accuracy. In this set up, the pixel size may be as small as 10 nm. Testing the technique by using translation tests would require that the imposed displacement be controlled to

within $1/100$ of the pixel size, or 1Å, which is not quite feasible. Finally, assuming that there is an experimental solution to this problem and that one employs the DIC on two scans translated relative to each other by a known amount (in meters), one would need to convert the DIC results, expressed in pixels, to meter units using the tube calibration. The error associated with that calibration amounts to 1% for in-plane distances and 5% for those out-of-plane. Consequently, such an assessment of the DIC performance would mainly reflect the limitation of the calibration procedure and would restrict *a priori* the strain resolution to 1% in-plane, 5% out-of-plane, which is unacceptably large.

There is actually a way to circumvent all these problems and assess accurately the resolution of the DIC on STM topographies. If one were to compare two scans translated with respect to each other through DIC, the subsequently computed displacement field should be perfectly uniform regardless of the amount of translation. That is, the displacement of every computational point should be strictly equal. The deviation of uniformity of such a field is then a direct assessment of the DIC resolution. This is a very simple experiment to perform, especially since the amount of translation is completely irrelevant. Moreover, in this procedure, the working units are pixels and, therefore, the DIC resolution is estimated regardless of the tube calibration error. In the following sections, the experimental set up for such a test is described, the main sources of noise are identified and finally the results of the translation tests are presented and discussed.

4.1 Experimental Set Up

As was explained above, the translation experiments involve acquiring a series of scans, each translated relative to each other, comparing them by pairs through the DIC technique and quantifying the non-uniformity of the subsequent displacement fields. In order to perform these tests in the most satisfactory fashion, there are some experimental issues that need to be discussed, the test procedure must be laid out and finally the

data analysis, whether preprocessing of the scans or postprocessing of the displacement calculations, need to be addressed.

4.1.1 Experimental Issues

The first task at hand is to determine the STM scan characteristics for the translation experiments. In this apparatus, the scan size is restricted by hysteresis considerations so that the excitation voltage to the piezoceramic tube stays in the $[\ -80\ V\ ,\ +80\ V\ ]$ range, which corresponds, according to the tube calibration, to roughly 900 LSB in the plane. Because of PC memory limitations, it is not possible to acquire a 900 $\times$ 900 $pixel$ scan. However a 300 $\times$ 300 $pixel$ scan with a pixel size of 3 LSB is definitely feasible yielding a scan area of 9135 $nm\ \times\ 9135\ nm$. This represents the largest scan for which the scan grid may be assumed to be square and regular and it is on such scans that the translation experiments were performed. As for all the other scan parameters, they are set to their typical values as discussed in section 3.1, which results in the following STM topographies characteristics

Pixel size = 3 LSB or 30.45 nm

Scan area = 300 $\times$ 300 $pixel$ or 9135 $nm\ \times\ 9135\ nm$

Feedback Loop Frequency, $F_{FBL}\ =\ 100\ KHz$

Acquisition Frequency, $F_{ACQ}\ =\ 400\ Hz$

Feedback Loop Gain, $K\ =\ 10^{-3}$

Bias Voltage, $V_b\ =\ 0.25\ V$

The next question to be addressed is how to generate a translation between two scans. Since the amount of translation is irrelevant, one could use the STM X-Y translation stages to move the microscope over the specimen surface. Actually, since zero translation

is as good as any, there is no need to translate the STM or the specimen. In fact, by not inducing any artificial translation, not only will one be able to assess the resolution of DIC by quantifying the non-uniformity of the displacement field, but in addition, the average displacement over the field will yield an estimate of the drift characteristic of the apparatus, a very important set of information for evaluating the overall performance of the system.

The previous paragraphs were dedicated to the definition of the general characteristics of the translation tests but there are also procedural variables that may affect the outcome of the experiment. Three such factors can be readily identified, namely the roughness of the specimen surface, the Z voltage history and the time between scans. Obviously, the roughness of the specimen surface, or mathematically speaking the amount of high frequency features in its topography, can have a great influence since if the specimen is too flat, the DIC calculations may not converge. Consequently two types of specimen are studied, 1) well polished aluminium specimens for which the surface roughness does not exceed 50 nm and 2) unpolished PolyVinylChloride (PVC) specimens for which the roughness is locally on the order of 150 nm. Typical scans of polished aluminium and unpolished PVC specimens are presented in Figure 4.1. Also, as was shown in section 2.5.1, the tube piezoelectric properties are affected by hysteresis, or in other words, are voltage history dependent. Even though this is inconsequential for the in-plane motion of the STM tip with proper precautions, its effect on the out-of-plane measurement has not been ascertained and should be examined. One can affect the Z voltage history by electronically offsetting the feedback loop between two scans, *i.e.*, increasing or decreasing the average voltage to which the piezoceramic tube is submitted. Comparing these two images by DIC will then reflect the influence of Z hysteresis, or Z voltage history, on the DIC resolution in displacement measurements. Finally there may be some time dependent behavior in the system originating in the electronics and/or in the tube

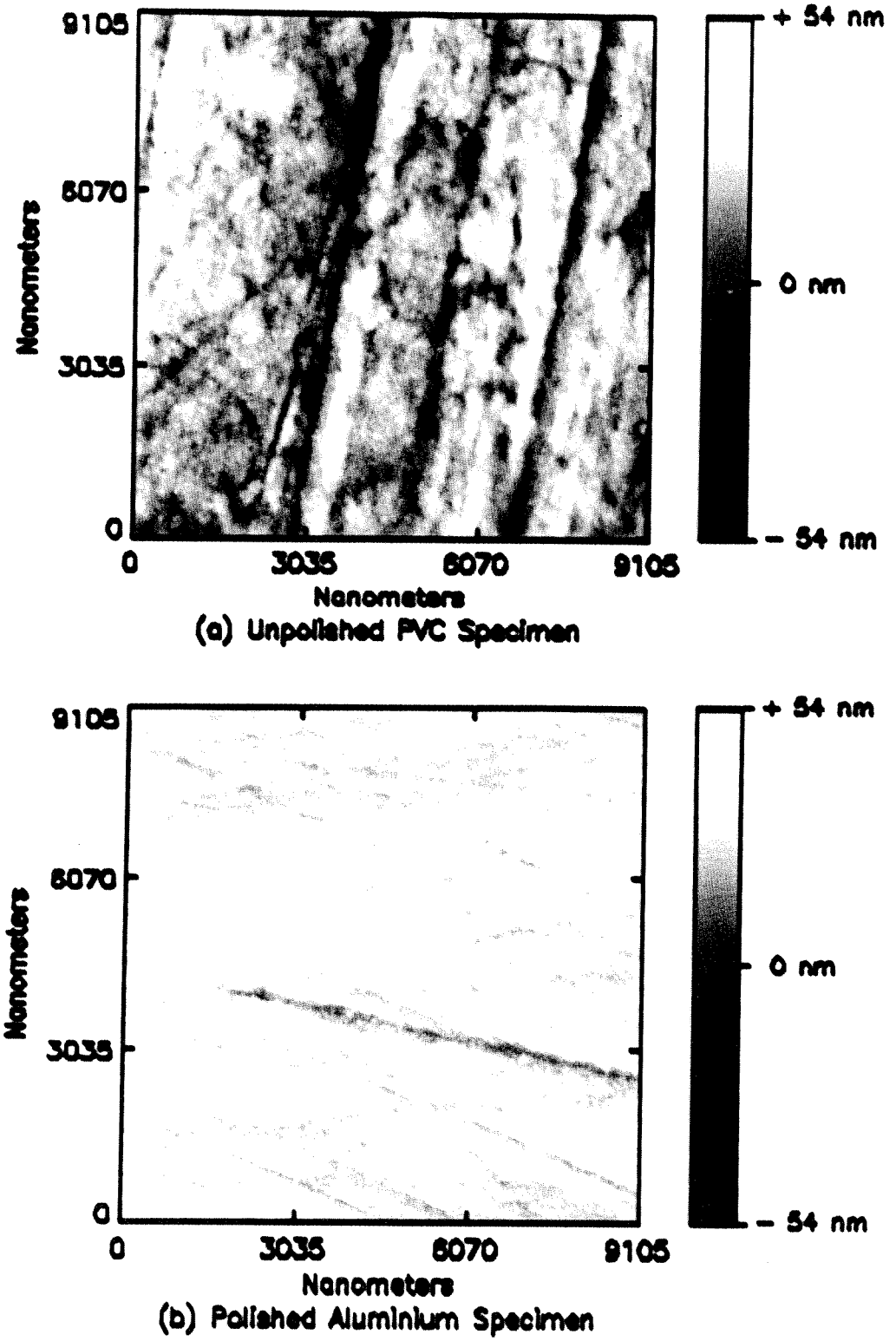

FIGURE 4.1 Examples of Topographies for Polished Aluminium and Unpolished PVC.

actuator. If such is the case, the time between scans will definitely affect the DIC results.

4.1.2 Procedure

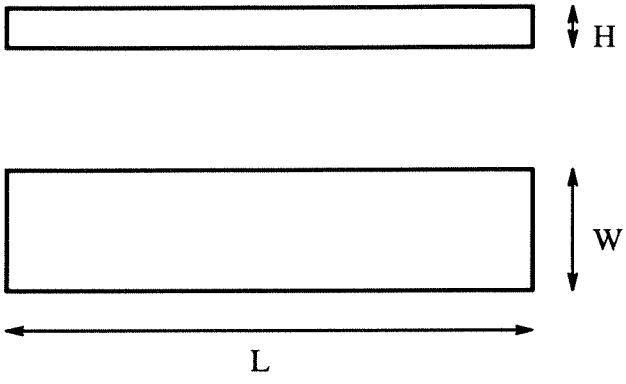

	PVC	Al
L	28	28
W	2	2
H	0.8	0.25

All dimensions in Millimeters

FIGURE 4.2 Specimen Geometry for the Translation Tests.

The specimens used for the translation tests consist of either a thin strip of PVC or of aluminium, their geometry being presented in Figure 4.2. The aluminium specimens are polished with a final grade of 1 μm diamond paste. The PVC samples are not polished. However, in order to remove small particles from their surfaces, they are held in contact with the 1 μm polishing wheel for about 30 s. Both types of specimens are then cleaned ultrasonically in isopropyl alcohol and a 40 nm thick gold-palladium layer is deposited onto their surface by a sputter coater. Once ready, the samples are clamped on the specimen base under the microscope and biased to 0.25 V. The STM tip is subsequently approached to within $\approx$ 10 μm of the specimen surface by rotating the microscope coarse approach ring as was explained in section 2.2.4. At this point, the STM is turned on. One hour later, after the electronics had time to reach thermal equilibrium, the tunneling acquisition is started. Sequences of four to twelve scans are acquired according to preset values of t_s, the time between scan. In between images, the Z correction voltage is

either kept at a constant value or offset by stepping the Inchworm actuator included in the tunneling column up or down.[i] The STM X-Y translation stages are never utilized and therefore the position of the microscope over the surface is theoretically constant throughout each test. As a final remark, the STM tips were made of tungsten, AC etched in a sodium nitrite solution and are available commercially.

4.1.3 Data Analysis

Before presenting and discussing the results of the various (non-) translation experiments, there are certain data analysis matters which need to be addressed. They involve the pre- and postprocessing of STM topographies as well as the numerical parameters for the Digital Image Correlation (DIC) scheme.

DIC does not require any preprocessing of the STM scans. However, two operations have proven valuable in increasing the convergence of the code. First of all, it was found that correcting for the out-of-plane tilt of the specimen under the microscope, as was done and explained for the calibration scans, is helpful in increasing the computational efficiency of the DIC scheme. The explanation lies in the fact that subtracting the least square plane from the topographic data reduces the low frequency content of the image, thus increasing the relative importance of medium to high frequencies in the scan spectrum to which DIC is most sensitive. The second preprocessing operation which was found to speed up the computation is a 3×3 median filtering of the scans. It consists of assigning at every pixel location the median value of a 3×3 $pixel$ window centered at that very position. It reduces "salt and pepper" type noise and therefore increases the contrast of the topographical features and facilitates convergence. It is important to note that none of

---

[i] Stepping the Inchworm up will momentarily increase the gap distance. Therefore the feedback loop will increase its correction to the piezoceramic tube to compensate and consequently offsetting the Z voltage to the piezoceramic tube - see section 2.3.2.

these two preprocessing operations could be shown to significantly change the resolution of the code, they only improve the convergence and therefore were applied to all the scans in this work.

Once preprocessed in this manner, the scans are ready to be compared by way of DIC. All the computations reported in this project have been carried out on the forward scan exclusively, for which the Y scan grid voltages follow the lower leg of the hysteresis loop. There is no other rationale to this besides consistency. As described in chapter 3, DIC requires the input of one critical parameter namely the subset size. It defines the number of pixels around the computational point which are included in the calculation of the local correlation coefficient. If the subset size is too big, high frequency fluctuations in the displacement field may be lost, if it is too small, it may not contain sufficient topographical information to ensure convergence of the scheme. Earlier work on DIC[49] has shown that a good compromise between preserving the local attribute of the displacement measurements and convergence requirements was reached for a subset size of 41×41 *pixel* and it was set to that value for all the computations. Finally for each DIC run, displacement calculations were performed at 121 points, located in the reference scan at pixel coordinates (x_i, y_j) such that

$$\begin{cases} x_i = 100 + 10(i-1) & i = 1,11 \\ y_j = 100 + 10(j-1) & j = 1,11. \end{cases} \tag{4.1.1}$$

These points are spread over the center area of the topography, thus accommodating potentially large translation without ever involving pixels close to the scan boundary which may be distorted because of hysteresis.

After the DIC computation is completed, a 3-D displacement field $\mathbf{U}$ results which represents the absolute measurement of the position of one image with respect to the other. In these translation tests, the interest focuses on the deviation of $\mathbf{U}$ from uniformity at every computational point. That is, the critical quantity is not $\mathbf{U}$ but $\mathbf{U} - \overline{\mathbf{U}}$, defined

here as the relative displacement field, where $\overline{\mathbf{U}}$ denotes the average of $\mathbf{U}$ over the field. Globally, the deviation of $\mathbf{U}$ from uniformity is measured by its statistical standard deviation $s(\mathbf{U})$.

4.2 Principal Sources of Displacement Measurement Error

When analyzing the result of the various translation experiments, it was clear that each test could be classified in one of two categories. The first consists of all the experiments for which the DIC computation yields a fairly uniform displacement field and where the deviation of uniformity seems random. The second category includes all those tests for which the deviation from uniformity is not random but has a definite structure to it. Random noise in data is acceptable since it can be quantified by a statistical error bar, however, correlated noise is unacceptable because it completely biases the result of an experiment. Much effort was therefore devoted to the identification of the correlated noise sources. Two main causes were singled out, the drift of the specimen with respect to the STM on one hand and the hysteresis of the piezoceramic tube on the other. The following sections explain in detail how and under which conditions each of these two factors affects displacement field measurements.

4.2.1 Drift Induced Noise

Among the displacement fields exhibiting correlated noise, some appeared as if the specimen had been stretched or compressed along one particular direction. In all these cases, the average translation value between images was significant, *i.e.*, the specimen was moving under the microscope while the scans were acquired. The cause for such a phenomenon is elaborated upon later in this section.

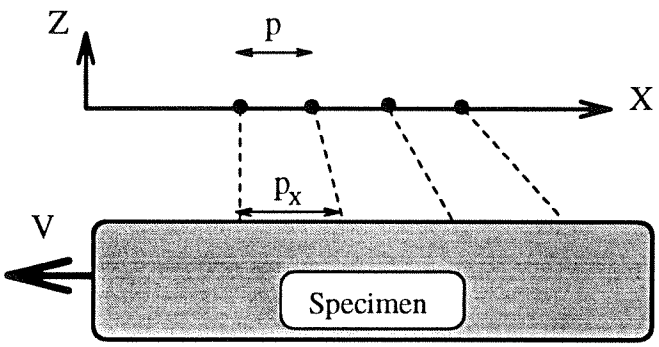

FIGURE 4.3 Distortion of the Scan Grid Induced by Drift.

To delineate in detail how specimen motion under the STM affects the displacement measurement, a specific example, involving a translation of the specimen along the X axis of the STM, is considered. Let scan A be the reference scan, acquired when the sample is still under the microscope. The unit grid cell of scan A is square and regular with a mesh spacing p. Let scan B be a subsequent scan, recorded after the specimen starts moving. The relative displacement of the STM tip with respect to the specimen during scan acquisition is now altered and consequently the scan grid is distorted - see Figure 4.3. Defining V as the rate of drift, t_x as the time it takes the tip to move from one X location in the scan grid to the next, the scan B pixel size along the X and/or Y axis, p_x and/or p_y, can be computed as

$$\begin{cases} p_x = p - Vt_x \\ p_y = p. \end{cases} \tag{4.2.1}$$

In scan A the pixel shape is a square of dimension $p \times p$ whereas for scan B it is a rectangle of dimension $(p - Vt_x) \times p$. Comparing scan A and B through DIC yields the mapping that brings locally a grid cell of B onto a grid cell in A, which in this case, disregarding an eventual global rigid body translation, is simply a stretch $\lambda_x = Vt_x/p$ along the X axis (in this example, the drift occurs along the X axis only). If $V < 0$ then $\lambda_x < 0$

and the subsequent relative displacement field, that is the the absolute displacement field $\mathbf{U}$ minus its average $\overline{\mathbf{U}}$, appears to be the result of a compression along the X axis and respectively for $V > 0$. Note that this analysis holds if V is considered as the difference in drift rate between scan A and B. Figure 4.4 is an experimental illustration of drift induced "compression." It was obtained by comparing two scans of an aluminium specimen. The first image was acquired early in the tunneling session. At that point, the specimen was drifting along the X axis in the positive direction as could be assessed *a posteriori* by comparing the relative position of all the scans during the experiment. When the second scan was taken, however, the drift was starting to die down. Therefore the relative drift rate was negative and it induced an apparent compression.

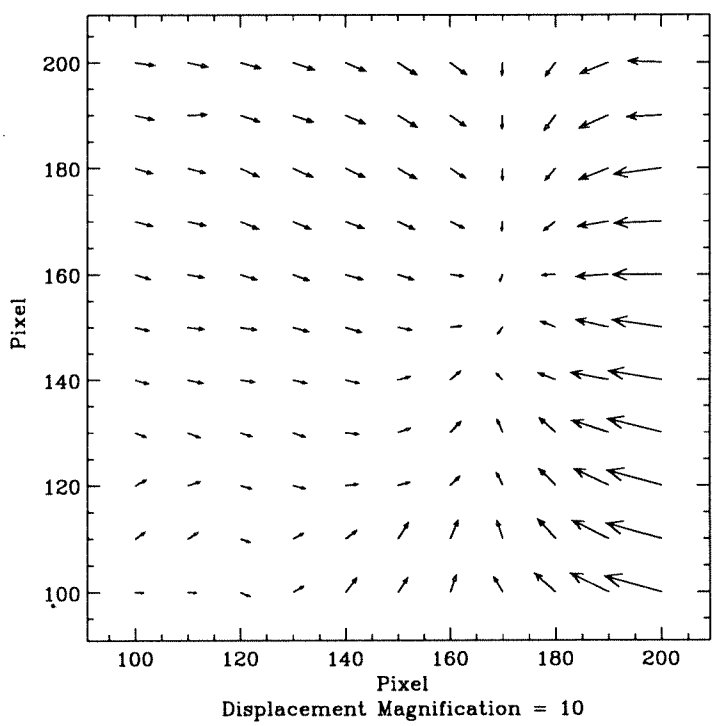

FIGURE 4.4 Example of a Displacement Field Distorted by Translation Drift.

If the drift motion of the sample under the microscope is a rotation rather than a translation, the induced displacement field can be shown to reflect an almost perfect shear

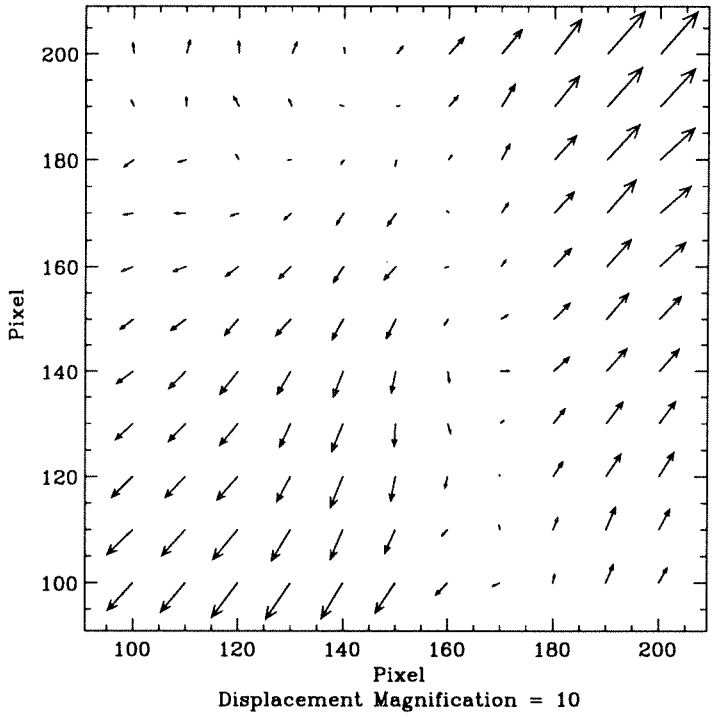

FIGURE 4.5 Example of a Displacement Field Distorted by Rotation Drift.

loading, *i.e.*, a compression along the $-/+$ 45° direction and a smaller traction along the $+/-$ 45° direction as shown in Figure 4.5. Obviously all the combinations of drift induced translation and rotation are possible and it may be difficult to recognize a displacement field as being the result of drift related noise. It is therefore necessary to determine the drift rate in translation for every scan, V, or in rotation, ω. If one compares two chronologically successive scans, acquired t_s minutes apart, one can compute the rigid body translation $\overline{\mathbf{U}}$ and rotation $\overline{\theta}$ between them. An estimate of $\overline{\mathbf{V}}$ and $\overline{\omega}$ may then be calculated as

$$\begin{cases} \overline{\mathbf{V}} = \dfrac{\overline{\mathbf{U}}}{t_s} \\ \overline{\omega} = \dfrac{\overline{\theta}}{t_s}. \end{cases} \tag{4.2.2}$$

All the drift related distortions were experimentally found to occur when at least one of the scans involved in the DIC computation was such that one component of $\overline{\mathbf{V}}$ was in excess

of 0.15 $pixel/min$ and/or $\overline{\omega}$ amounted to more than $0.01°/min$. As a consequence, if a scan is exhibiting such drift characteristics in the rest of this work, it is regarded as distorted and is therefore discarded. In most of the cases for which drift distortion was noticed, it could be traced to an improper clamping of the specimen under the STM. Therefore, natural drift causes, such as thermal expansion of the microscope structure, do not seem to be at the origin of the problem.

4.2.2 Hysteresis Induced Noise

Among all the tests that exhibited a nonrandom distortion in the displacement measurement, there was a sizeable number for which the noise patterns were strikingly similar, so as if the specimen had been hydrostatically loaded as illustrated in Figure 4.6. The noise was usually fairly symmetric and appeared systematical when two scans were compared between which the Z voltage to the piezoceramic tube had been offset, *i.e.*, when the Z voltage history had been significantly changed between images.

To explain these observations, the origin of this noise should be such that its induced distortions affect the X-Y axes equally and be triggered by a change in Z voltage history. When the problem is stated in this fashion the resolution must be found in term of d_{31}, the piezoelectric charge constant of the tube actuator. As the Z voltage history is altered, the value of d_{31} is changed because of hysteresis which in effect reduces/increases the pixel size of subsequent scans, thus resulting in an *apparent* hydrostatic traction/compression type displacement field. Various Z voltage histories between scan were tried to see whether the original value of d_{31} could be recovered. None of these attempts were ever successful. Actually, it was found that whatever the Z voltage history was, d_{31} always seemed to increase, *i.e.* the hysteresis induced displacement pattern is always compressive when comparing a scan before the history change to a scan after. This is not quite consistent with the hysteresis assumption presented above and there is no explanation yet for the reason.

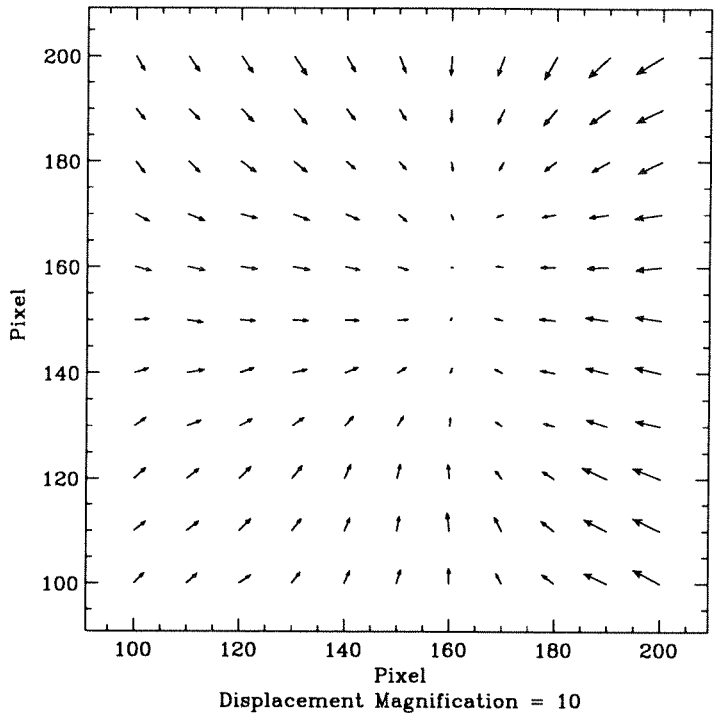

FIGURE 4.6 Example of a Displacement Field Distorted by Hysteresis.

The other procedural parameter t_s, the time between successive scan, has sometimes also been found to trigger the hysteresis noise. When t_s is shortened significantly, all the scans acquired for smaller t_s exhibited the hysteresis distortion when compared to those with longer t_s. However, increasing t_s did not seem to affect the scan grid.

Only extremely rigorous procedural constraints have been shown to successfully limit the occurrence of hysteresis distortions. First, t_s should be fixed once and for all throughout an experiment. Second and most importantly, the Z voltage should be monitored in between scans and kept at $0 \pm 0.1\ V$ using the Inchworm actuator to offset it if the need arises. Only very rarely did the hysteresis noise reach detectable levels under these circumstances.

4.3 Results and Discussion

After having identified the two main causes of noise in the displacement measurements, it was necessary to perform a whole new series of translation tests according to the strict procedural guide lines which were found to limit the occurrence of distortions. In particular, the time between scans, t_s, was set at 20 min and in between scan acquisitions, the Z voltage fluctuations were controlled. Each experiment consisted of a sequence of four to twelve images of the same area of the specimen. Among these scans, all pair combination were mutually compared by Digital Image Correlation (DIC). The uniformity of the subsequent 3-D displacement fields $\mathbf{U}$ of components u, v, w in the STM XYZ frame, were quantified by computing the standard deviation of $\mathbf{U}$ for each of its components separately, namely $s(u)$, $s(v)$ and $s(w)$. Finally these three variables were averaged over all the tests to yield the results presented in Table 3.

Specimen Material	# of tests (DIC Runs)	$\overline{s(u)}$ $(pixel)$	$\overline{s(v)}$ $(pixel)$	$\overline{s(w)}$ (LSB)
Aluminium	48	0.15	0.09	50
PVC	75	0.08	0.08	90

Table 3 Standard Deviations of the Displacement Components for Translation tests.

The first obvious information which can be drawn from these results is that there is a significant difference between the PVC and aluminium specimens which is interpreted to mean that the roughness of the specimen surface is a definite factor in the overall resolution power of the method.

In a flat specimen, the high frequency content of its topography is limited, *i.e.*, the height difference between two neighboring points on the surface is small on the average (smaller than for a rough sample). To compute the out-of-plane displacement w at a given point between a reference scan and a translated or deformed one, the DIC code basically subtracts its height from the reference topography the elevation at the location to which

it is mapped by the in-plane deformation parameters. If there is a slight inaccuracy in the mapping coefficients, it induces an error in w on the order of the average roughness of the specimen. This error is therefore smaller for flat topographies than for rough ones. It is consequently not surprising to measure a $\overline{s(w)}$ that is smaller for flat aluminium samples than for PVC specimens.

The high frequency deficiency in "a flat scan" also explains the overall larger $\overline{s(u)}$ and $\overline{s(v)}$ for the aluminium samples. Indeed, it is the occurrence of the high frequency features in a scan subset that provide its unique topographic characteristic, therefore the lower the high frequency content, the more difficult the convergence of the DIC scheme. Actually it was noticed during data processing that the convergence of the DIC code was 20% to 30% slower for flat scans than on rough ones, *i.e.*, the deformation parameters are not as clearly defined and consequently the error increases.

More difficult to understand is the inconsistency between $\overline{s(u)}$ and $\overline{s(v)}$ for flat samples. There is no reason for the DIC method to be more accurate along one axis than the other. Its cause must therefore originate in the STM itself. The only difference between the X and Y axes lies in the way the scan grid is traversed by the tip during scan acquisition. On the forward scan the probe follows a full Y range or 300 *pixels* before it it advances 1 *pixel* in the X direction. Thus the rate of motion of the probe along the Y axis is two orders of magnitude greater than along the X axis. Therefore, according to equation (4.2.1), eventual drift affects the X direction much more than the Y direction. However, among the 48 tests on aluminium samples only two exhibited some signs of drift induced noise. Consequently global drift is not a viable explanation. Yet, the drift may very well be intermittent or irregular. In that case the grid would be locally distorted and as discussed above more so in the X direction. When DIC compares such a scan to a flawless one, it extracts a subset of the image and tries to match it to the reference image. If the topographic information within the subset is very sharp, as is the case for

rough specimens, the match is easy and the eventual irregularities of the scan grid do not affect it much. However, if the surface features within the subset are insignificant, as it is for a flat sample, the optimum mapping is hard to define and the local distortions may have a bigger influence on the final results. In the subsequent displacement computation then, the error will be larger overall but more so in the X direction. If this somewhat speculative rationale holds, it not only explains why the in-plane standard deviations are higher for aluminium than for PVC, but also why $\overline{s(u)}$ is bigger than $\overline{s(v)}$.

Abiding by this explanation, one may also infer the optimum roughness which would decrease the error or standard deviations to a minimum. The optimum roughness is such that the displacement measurement error along the X axis is equal to that along the Y axis. Then the topographic information within the DIC subset is indeed sufficient to completely overcome any local distortions; if that was not the case $\overline{s(u)}$ would be larger than $\overline{s(v)}$. PVC appears therefore to be rough enough and the error associated with it, $\overline{s(u)} = \overline{s(v)} = 0.08\ pixel$ most probably reflects the displacement resolution of the whole STM-DIC measurement system.

The standard deviation is actually a direct statistical measure of the displacement field accuracy. Therefore it can be claimed that, for the specific experimental settings of these tests, performed on specimens where the roughness amounts to 150 nm, the errors in displacement measurement are

In-plane displacement, error = $\pm 0.08\ pixel$ or $\pm$ 2.4 nm

Out-of-plane displacement, error = $\pm 90\ LSB$ or $\pm$ 0.75 nm.

Thus, the total possible in-plane displacement resolution is 4.8 nm whereas for out-of-plane displacement it is 1.5 nm.

To conclude this discussion, some questions raised during the tube calibration procedure can now be answered. First, the overall randomness of the noise in the displacement

measurements confirms that the in-plane hysteresis of the tube is not significant in the central portion of the scan. Similarly, coupling between the X and Y motion of the tip is below detectable levels. These two facts corroborate some assumptions made earlier in section 2.5.1 and therefore validate the calibration results a *posteriori*.

CHAPTER 5

Stress-Strain Response of PolyVinylChloride

Now that the characterization testing of the STM as a displacement measurement tool is completed, the investigation of mechanical systems at the submicron scale can be pursued. As the first such study, a conceptually simple experiment is considered, namely the tensile loading of thin PolyVinylChloride (PVC) specimens. The motivation for this specific test is twofold. First, because of the high spatial resolution of this STM ($10\ nm$), it constitutes a first step in determining the scale, if any, at which the continuum assumption may break down (for PVC). Second, earlier works[47,50,51] have shown that at the 3 μm size scale continuum mechanics appeared applicable. Therefore, if one considers the average of the displacement fields over the scan area as obtained by Digital Image Correlation (DIC) of STM topographies, rather than its local values, it should reflect the macroscopic properties of PVC, thus offering a final validation for the whole scheme. In this chapter, the experimental set up for the tensile testing of PVC is explained in detail, qualitative observations of the strained PVC surfaces are presented and finally the quantitative results of the tensile experiments are discussed.

5.1 Experimental Set up

The experimental set up for the tensile tests is very similar to that of the translation experiments. However there are some issues only relevant to the loading of specimens under the microscope that need to be discussed specifically. In turn, the test procedure requires some adjustments over that proposed in the previous chapter. Finally, since the objectives of the tensile experiments are different than those for the translation tests, the data reduction also demands some additional considerations.

5.1.1 Experimental Issues

There are three experimental problems associated with loading a PVC sample. The first two are related to the change in boundary conditions to which the specimen is submitted. The remaining one deals with the viscoelastic behavior of PVC.

The first issue at hand arises because of the design of the loadframe. As described earlier in section 1.2.5, the microscope loading system is displacement controlled: to provide the load, one grip of the loadframe is physically moved while the other is held fixed. The subsequent load is measured by recording the force necessary to apply to the fixed end for holding it stationary. As a consequence, all the accessible points of the sample surface are moving during loading. But, during a tunneling session, the STM tip is only $\approx 1\ nm$ away from the specimen surface and therefore the change in boundary conditions, *i.e.*, the displacement imposed to the moving end of the sample, must be very smooth so as to prevent tip-specimen contact. The only method to check whether or not such a "crash" occurs is to acquire a scan after the loading step and look for signs of contact on the specimen surface. Figure 5.1 is a typical illustration of loading-induced tip-specimen contact. It was recorded after an abrupt load increment along the $-45°$ direction. The probe touched the surface three times, creating three crater type features aligned with the loading axis. The obvious solution to avoid such undue interactions between the tip and the sample would be to retract the probe some microns away from the surface before deforming the specimen. This procedure is however undesirable because retracting the tip would result in an offset of the feedback loop which, in turn, would induce hysteresis distortions in the subsequent scans. Therefore, the loading must be performed *in-situ* and precautions must be taken to limit the occurrence of tip-specimen contact. The rate of motion of the translating grip should, therefore, be small and constant throughout the specimen deformation so as to restrict acceleration fluctuations and jolts transmitted to the sample by the load providing Inchworm actuator. Therefore, the speed

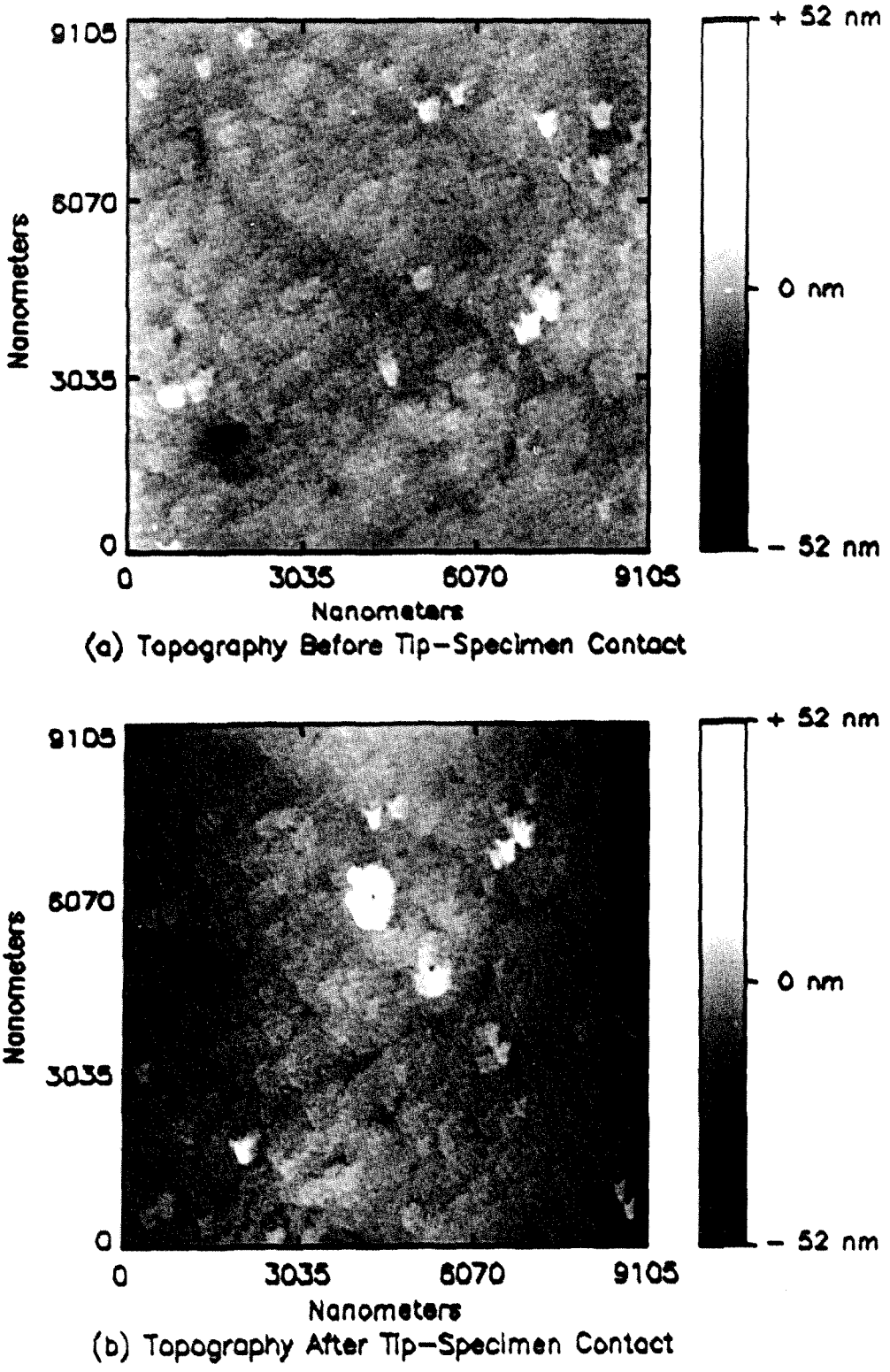

FIGURE 5.1 Example of Load Induced Tip-Specimen Contact on a Polished PVC Specimen.

of the grip was fixed in this set up at 0.1 μms^{-1}, two orders of magnitude smaller than the scanning velocity. More importantly, extreme care must be given to the alignment of the loadframe and of the specimen within it. Experimentally, it was observed that for a typical 0.5% uniaxial strain increment the out-of-plane motion of the specimen surface could be limited to less than 100 nm therefore validating the design as well as the alignment procedure of the loadframe.

The other issue associated with the change in boundary conditions on the specimen has to do with the fact that after the sample has been deformed, the position of the tip with respect to the specimen has changed. Thus, there may be very little overlap, if any, between scans acquired before and after deformation. It is therefore necessary to move the STM tip so as to locate it back over the same area of the specimen surface. Actually the closer the STM tip is repositioned to its original station the better since that avoids having to compare by Digital Image Correlation (DIC) pixels in the center portion of one image to pixels located close to the second image boundary which may be distorted by in-plane hysteresis. For this reason, the STM X-Y translation stages are activated after each load step so that the microscope follows the same surface area throughout the deformation process. Such an operation prohibits the determination of absolute displacement fields. Therefore, the DIC displacement output $\mathbf{U}$ should be regarded as the superposition of a rigid body translation, here estimated as $\overline{\mathbf{U}}$, the average of $\mathbf{U}$ over the field, and a displacement field $\mathbf{U} - \overline{\mathbf{U}}$, expressing the relative motion of points within the scan area.

Finally, there are some experimental problems in testing (unplasticized) PVC because of its viscoelastic properties, however weak they may be at room temperature. Indeed, when such a material is deformed, it relaxes and the measured load decreases with time at the rate of $2 - 3\%$ *per decade*. To make matters worse, it was found necessary in the translation tests to acquire a sequence of three or four scans at each load in order to estimate the potential rate of drift of the specimen. With a time between scans set

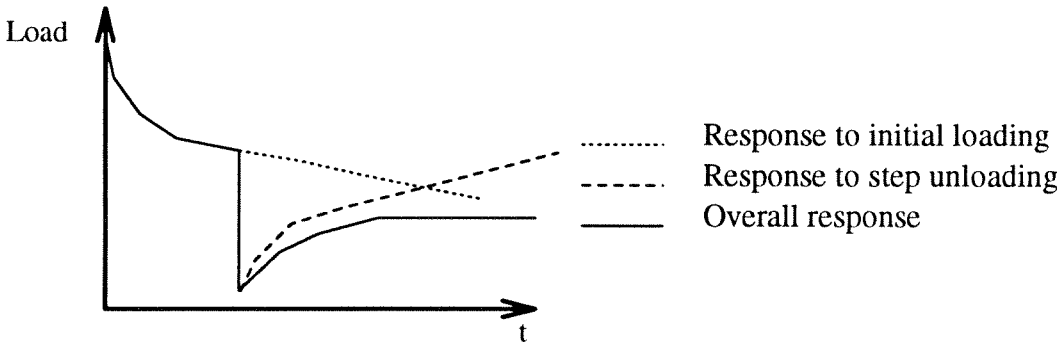

FIGURE 5.2 Viscoelastic Response of a PVC Specimen to an Unloading Step.

at $t_s = 20\ min$, roughly one hour or three and a half decades is required at every load level and the subsequent drop in measured load can amount to $6 - 9\%$ of the load step. Since the specimen is submitted to boundary conditions of fixed displacements, the in-plane displacement field is not likely to be affected by the relaxation. However, such a drop induces an out-of-plane motion of the specimen surface (time dependent Poisson effect[j]), so that as a scan is being acquired, the average Z position of the sample increases or decreases with respect to the STM, resulting in an artificially tilted topography and thus compromising out-of-plane displacement measurements. In terms of STM response and function, such a tilt corresponds to a progressive offset of the feedback loop, therefore inducing hysteresis distortions. Consequently, it is of the utmost importance in testing a viscoelastic material to restrict the relaxation or creep behavior by careful management of the deformation history. For that very reason, most of the tensile experiments performed on PVC are unloading tests : the load is initially ramped up to its maximum value ($13\ N$) and allowed to relax for one hour before the experiment is started after which time the relaxation rate has decreased to manageable levels. When the test begins, the load is fairly stable and undistorted scans may be recorded. Upon unloading (typically $-4\ N$),

[j] Measuring the out-of-plane relaxation of the specimen by recording the height of its surface with respect to the STM at a given location but at various times would be a method to evaluate the time dependence of Poisson ratio.

the material will, on the one hand, pursue its relaxation from the initial loading but also react to the sudden decrease of the pulling force on the other; approximatively 30 s after the load change, the two responses do nearly cancel each other resulting in a stable load reading for about $50 - 70$ min as sketched in Figure 5.2. The process can be repeated successfully for subsequent load steps. With this procedure, no artificial tilt of the image is induced and the viscoelastic properties of PVC are not likely to be responsible for eventual distortions of the scans.

5.1.2 Experimental Procedure

The experimental procedure for the tensile tests is very similar to that for the translation experiments and will not be detailed here again thoroughly. In this section only the differences between the two are discussed and some of key characteristics are restated.

The specimen for the tensile experiments consists of a thin strip of PVC[k] glued to two ceramic (MACOR) tabs with 5 min epoxy, as shown in Figure 5.3. In order to ensure good alignment of the specimen within the tabs, a jig was constructed which duplicates the loadframe grips and the epoxy cures while the PVC strip is resting in the jig. The specimen is then coated with a 40 nm thick gold-palladium layer.

The initial loading is typically 13 N along the $\tilde{\theta} = 99.5°$ direction with respect to the STM X-Y axis.[l] The unloading step is set at $\approx$ 4 N and at every load level three scans are acquired, one every 20 minutes. In between scans and while the unloading is taking place, the Z voltage to the piezoceramic tube is monitored and corrected if necessary to keep it at 0 ± 0.1 V.

---

[k] All the specimens were cut from a $2' \times 4'$ sheet of Type 1 gray PCV, 1/32" thick, manufactured by Ain Plastics.

[l] The assembling of the tunneling axis of the STM involves screwing the current detector and piezoceramic tube to the Inchworm actuator. It is therefore difficult to ensure a perfect alignment of the tube with respect to the loadframe.

Finally the scan characteristics are chosen similar to those for the translation tests, namely

Pixel size = 3 LSB or 30.45 nm

Scan area = 300 $\times$ 300 $pixel$ or 9135 nm $\times$ 9135 nm

Feedback Loop Frequency, $F_{FBL} = 100\ KHz$

Acquisition Frequency, $F_{ACQ} = 400\ Hz$

Feedback Loop Gain, $K = 10^{-3}$

Bias Voltage, $V_b = 0.25\ V$

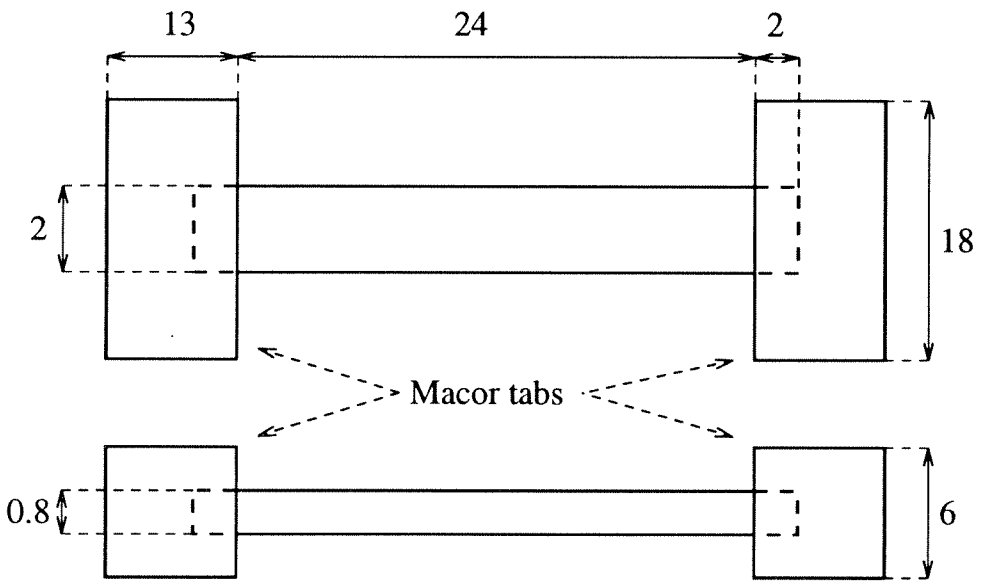

All Dimensions in Millimeters

FIGURE 5.3 PVC Tensile Specimen.

5.2 Data Analysis

There are many similarities between analyses for the translation and tensile test data. In particular, the preprocessing of the scans are identical. Every image is tilt

corrected and passes through a 3 × 3 median filter - see section 4.1.3. Digital Image Correlation (DIC) computations are carried out with the same settings, *e.g.*, the subset size is 41×41 *pixels* and the computational points are located in the reference scan at pixel coordinates $x_i = 100 + 10(i-1)$, $i = 1$ to 11 and $y_j = 100 + 10(j-1)$, $j = 1$ to 11, yielding the displacement field at 121 discrete locations within the center third portion of the image.

Given a DIC output displacement field $\mathbf{U}$, the postprocessing interest focuses on $\mathbf{U} - \overline{\mathbf{U}}$, where $\overline{\mathbf{U}}$ denotes the average of $\mathbf{U}$ over the whole field. However, it is necessary for the tensile experiments to extract from $\mathbf{U} - \overline{\mathbf{U}}$ the average strain levels to characterize the displacement field over the scan area. If the loading direction is parallel to the X direction of the STM axis system with its origin at the center of the scan, the relative displacement field $\mathbf{U} - \overline{\mathbf{U}}$ having in-plane components u and v should ideally be such that

$$\begin{cases} u = \varepsilon x \\ v = -\nu\varepsilon y \,, \end{cases} \tag{5.2.1}$$

where ε is the uniaxial strain along the X axis and ν is the Poisson's ratio of the material. However, experimentally, the loading direction is $\tilde{\theta} = 99.5°$: rotating the field (5.2.1) by $\tilde{\theta}$ yields

$$\begin{cases} u = \varepsilon(cos^2\tilde{\theta} - \nu sin^2\tilde{\theta}) - \varepsilon(1 + \nu)cos\tilde{\theta}sin\tilde{\theta}y \\ v = -\varepsilon(1 + \nu)cos\tilde{\theta}sin\tilde{\theta}x + \varepsilon(sin^2\tilde{\theta} - \nu cos^2\tilde{\theta})y \,. \end{cases} \tag{5.2.2}$$

From experimental u and v data, the obvious method to extract ε, ν and $\tilde{\theta}$ would be to perform a simultaneous non-linear fit of equations (5.2.2). If the displacement field is smooth and well defined, that would certainly be appropriate. It was found, however, that the data exhibited some scattering around the expected macroscopic field. The convergence of the non-linear fit may, therefore, be compromised. Consequently, one needs to force matters slightly. Experimentally, the direction of pulling is close to the Y direction ($\tilde{\theta} = 99.5°$) and the steepest displacement gradient should thus be observed in

the v displacement component. Letting $\theta = \tilde{\theta} - 90°$, v can be rewritten as

$$v = \varepsilon(1 + \nu)cos\theta sin\theta x + \varepsilon(cos^2\theta - \nu sin^2\theta)y \,. \tag{5.2.3}$$

Let $\Pi = ax + by$ be the least square fitted plane of the experimental v. Provided equation (5.2.3) represents the data,

$$\begin{cases} \varepsilon(1 + \nu)cos\theta sin\theta = a \\ \varepsilon(cos^2\theta - \nu sin^2\theta) = b. \end{cases} \tag{5.2.4}$$

Obviously, there is, in this last system, one unknown too many, but assuming $\nu = 0.3$, one can solve for ε and θ as

$$\begin{cases} tan\theta = -\dfrac{b}{a}\dfrac{1+\nu}{2\nu} \pm \dfrac{1}{2\nu}\sqrt{\dfrac{b^2}{a^2}(1+\nu)^2 + 4\nu} \\ \varepsilon = \dfrac{a}{(1+\nu)}\dfrac{(1+tan^2\theta)}{tan\theta}. \end{cases} \tag{5.2.5}$$

The ambiguity on $tan\theta$ in (5.2.5) can easily be lifted by realizing that θ is supposedly small ($\theta = \tilde{\theta} - 90° = 9.5°$) and therefore from (5.2.4) one has

$$\varepsilon = b + O(\theta^2). \tag{5.2.6}$$

Consequently, the value of $tan\theta$ which yields ε within $10 - 20\%$ of b and of the same sign, is the physically meaningful one.

This method for extracting the uniaxial strain ε and the principal axis direction θ, from the data may appear biased in that it forces a result out of the measured field without checking whether that very field corresponds in any way to the theoretical one. One must keep in mind, however, that the experimental displacement should only agree with the macroscopic one on average, not point-to-point and it is believed that this analysis truly draws out the average trend of the data.

5.3 Qualitative Observations

Even though the tensile test procedure calls for an unloading of the specimen, some loading experiments were performed early in this project. Because of the various problems related to the viscoelastic relaxation of the PVC under the microscope, the displacement fields for these tests were corrupted by hysteresis and no trustworthy quantitative results are available. However, if the hysteresis distortion affects the displacement measurements, the specimen scans allow for qualitative observations as records of the surface topography at various load levels.

In the (earlier) loading experiments, four different PVC specimens, coated with either 20 nm or 40 nm of gold-palladium, were loaded progressively. At each load, scans were acquired at various in-plane resolutions, 30.45 nm (the same as for unloading tests) but also at 20.3 nm and 10.15 nm. Executing Digital Image Correlation (DIC) on these scans yielded, besides distorted displacement fields, in some tests, small domains within the images where the convergence of the scheme was very poor. Subsequent careful observations of these STM scan areas revealed the appearance of significant topographic changes as the load increased. Moreover, it was noticed that the local convergence deficiencies and the corresponding topographic changes only occurred upon the first loading of three out of the initial four specimens.

Figure 5.4 presents some of the topographic differences which were observed. In all these cases, the features are small, on the order of $100 - 200$ nm of in-plane dimension. However the height of the defects, whether a dip or a crest, are significant, namely 10 to 40 nm, especially when compared with the average 150 nm roughness of the PVC specimens. The initiation of such topographic changes does not appear to be related to the pre-existing surface profile since their occurrences arise equally in flat or rough areas of the STM scans, but there is a definite correlation between their size and the load. Even at a stress level of only 1.5 MPa corresponding to a straining of 0.15% (PVC Young's

Modulus $\approx$ 1 GPa), some new topographic features could be detected.

To draw any conclusions from these observations, the influence of the gold-palladium layer on the specimen surface should first be assessed. In particular, one could wonder if these new topographic features are the result of local delaminations of the gold-palladium film and/or strain-induced unmasking of pre-existing defect. The coating on each sample surface is deposited by placing the specimen in a sputter coater. In the coating chamber, this apparatus creates a plasma of gold and palladium atoms in a rarefied argon atmosphere (90 $mTorr$). The high voltage (1.1 KV) responsible for the dissociation of the gold-palladium from the target also directs the atoms toward the specimen surface. Therefore the gold-palladium layer is built up "atom by atom," and their local orientation and stacking creates the grain structure of the film with a grain size of $5 - 10$ nm[m]. It is thus unlikely that the gold-palladium film is masking the features originally and collapses onto them as the strain increases. Moreover, if that were the case, the coating would fail, leaving non conductive areas of the specimen exposed to the STM tip which would, in turn, cause a loss of tunneling signal over the defect, a phenomenon that was never observed while scanning the damaged surfaces. Delamination of the coating can also be ruled out since most of the damages are depressions (holes) rather than local hills on the surface. It is therefore safe to conclude that the recorded topographic changes correspond to inhomogeneous deformation in the PVC. At such a small scale of $100 - 200$ nm, an inhomogeneity does not represent the material bulk behavior, rather, a few polymer chains ($5 - 15$ nm) must be involved. In that sense, the size of these features may reflect the lower limit below which a continuum type formulation for the constitutive behavior of PVC may no longer be advisable.

Once these topographical changes have occurred, no further "damage" can be ob-

---

[m] The reason for using a gold-palladium coating, rather than pure gold layer, lies in the fact that this gold-palladium grain size is very much smaller than that for pure gold ($50-100$ nm).

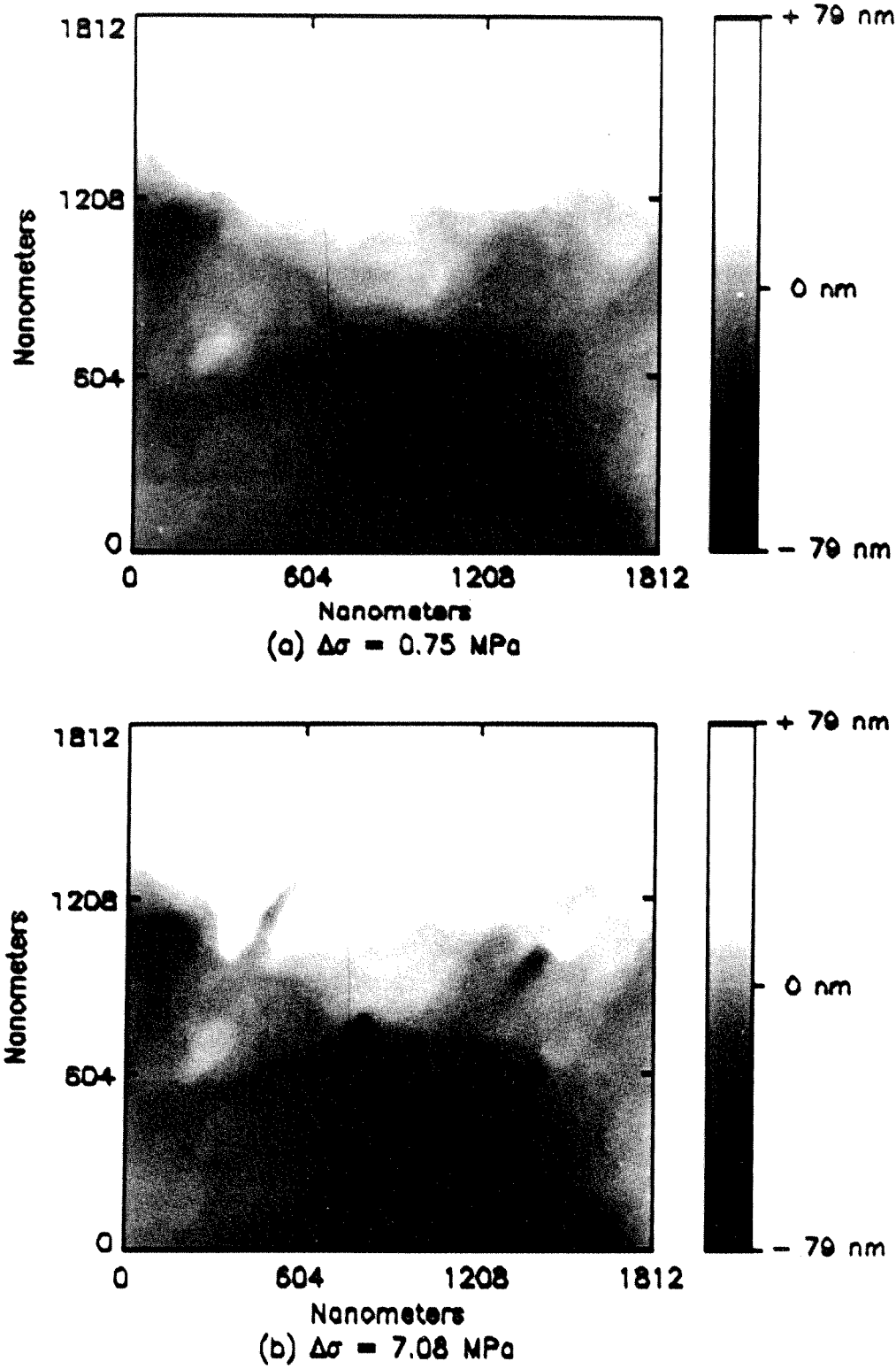

FIGURE 5.4 Example of Load Induced Topographic Changes on Virgin PVC Specimen Surfaces.

served, that is, the local reorganization of the PVC micro-structure (chains) seems irreversible. If this analysis is correct, one should observe macroscopically a difference in the strain-stress response of the PVC specimens between their first loading and all the subsequent ones. Because the STM strain measurements need to be performed during unloading tests, they cannot corroborate this hypothesis. However, strain gauge data, originally obtained to confirm the STM results, should show the effect of this assumed microscopically induced behavior of PVC.

5.4 Quantitative Results

The analysis of the topographic features appearing on the surface of a virgin PVC specimen has led to two observations. First, it appears that macroscopically the stress-strain response of PVC tensile specimen may be different between the first loading and all subsequent reloadings. Second, it is suggested that at the scale of 100 nm, inhomogeneities in the displacement fields may be observable. In order to confirm or invalidate these predictions, measurements of the macroscopic responses of PVC specimens to tensile loading over several load cycles were performed and high spatial resolution displacement fields were computed from STM scans of PVC specimens at various load levels. The following section presents the results of these investigations.

5.4.1 Macroscopic Strain Measurements

Macroscopic measurements of strain were performed by attaching a strain gauge to a specimen similar to those prepared for the STM tensile experiments. The specimen was placed in the microscope loadframe and four tests were conducted. The first three consisted in loading the specimen by increments of $\approx 10^{-4}\ m/m$ up to $8 \times 10^{-4}\ m/m$. At each strain level, the load cell and strain gauge signals were recorded. The fourth test

was similar in its procedure to the initial three, but it was carried on up to the failure of the strain gauge ($1.5 \times 10^{-2}\ m/m$). These data are presented in Figure 5.5.

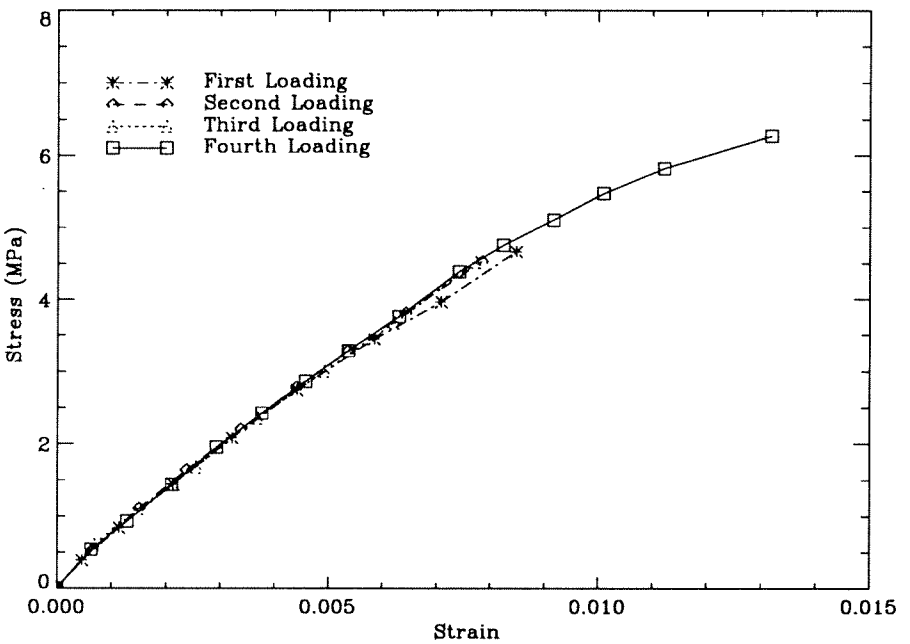

FIGURE 5.5 Strain Gauge Measurements on PVC specimens Subjected to Tensile Loading.

As expected on the basis of the earlier qualitative analysis of the tensile tests, the stress-strain response during the first loading is different from that for the subsequent reloadings. In fact, at a stress level of 4.5 MPa during the first loading, the specimen experiences about $4 \times 10^{-4}\ m/m$ more strain (four times the experimental error) than it does for any reloading. As for the second, third and fourth loadings, the responses are identical up to $8 \times 10^{-4}\ m/m$.

The trend in the strain gauge data seems to corroborate the analysis of the surface of the PVC specimens in section 5.3 and, based on those results, one may attempt an explanation for the observations at both the macroscopic and microscopic size scales. In the virgin PVC the polymer chains are in equilibrium with each other, but not necessarily

in a minimum energy state. As the material is strained for the first time, these chains rearrange, altering locally the initial partition of free volume and energy (occasionally) creating topographic changes on the specimen surface. Therefore, the strain recorded on the surface of the specimen reflects not only the elastic response of the material but also the permanent readjustments of the polymer chains. These rearrangements are likely to be irreversible. In subsequent reloadings to previous load levels, there are no more or fewer local molecular adjustments in the material and only the elastic response of the reordered PVC structure is reflected in the strain, so that the material appears stiffer. If the stress increases above the maximum stress which the specimen experienced in its previous history, some more rearrangement of the polymer chains takes place, and the stiffness decreases further. Abiding by this rationale, one can, perhaps, view the topographic changes on the surface as a measure of the free volume being redistributed locally. One can estimate the number of sites at which (molecular) readjustment occurs from the present results; assuming that this reorganization is an indication of the statistically distributed sites throughout the bulk and that the measured size of these sites is indicative of the extent of the (polymer chains) rearrangment, one can approximate the volume change associated with the apparition of the new topographic features. This change turns out to be in the range of 0.05 to 0.2% for this PVC, a number that is close to what is a typical content of free volume in polymers.[52]

While one might argue that there is really insufficient experimental evidence to assert the validity of this reasoning, it is nevertheless consistent with the available data and is possibly reasonable for bridging the gap between the macroscopic and microscopic behavior of PVC under uniaxial tension.

5.4.2 Computation of the Displacement Fields

To conclude this investigation of the deformation mechanisms in PVC, unloading

tests were performed according to the procedure laid out in section 5.1.2 and displacement were extracted by comparing with Digital Image Correlation (DIC) STM scans of PVC specimens at various load levels. The motivation for such experiments are twofold. First, the qualitative analysis of topographies of deforming PVC samples suggested that, at the $100 - 200\ nm$ scale, the deformation of the specimen might be inhomogeneous. Second, earlier work[47,50,51] had shown that at the 3 μm scale continuum mechanics concepts appeared applicable. Therefore the computed displacement fields averaged over the scan area should reflect the macroscopic properties of PVC, thus offering a final validation for the STM-DIC scheme as a displacement measurement tool at the submicron level.

Nine *in-situ* tensile tests of PVC specimens were performed under the STM. In each experiment, three scans of the sample surface were acquired at three or four different load levels. Every image recorded was compared to the remaining two of the same specimen area at the same load through Digital Image Correlation (DIC) in order to evaluate the drift characteristics of the scan. Finally the three topographies acquired at the initial and therefore highest load were correlated by DIC to all the scans recorded at subsequent loads, yielding the displacement response of the PVC specimens to load decrements.

The analysis of the displacement fields resulting from images acquired at the same load yielded very good results, consistent with those obtained during the translation experiments. The drift was found to be insignificant and no hysteresis type distortion was recorded - see Figure 5.6. However, even though extreme care was given to unload the specimens as smoothly and slowly as possible, in more than 50% of the cases, the comparison between images acquired before a load decrement and a scan recorded after that would yield a displacement field tainted by hysteresis noise. Usually, such a field could be clearly recognized as being the superposition of the expected (relative) compression response[n] of the material and the hysteresis induced displacement field of the hydrostatic

[n] Recall that these experiments involve unloading.

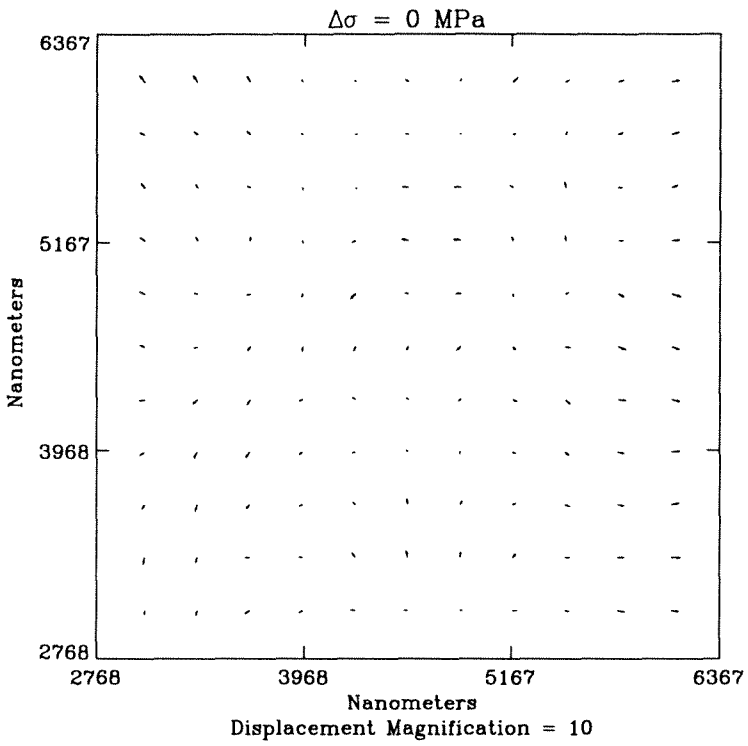

FIGURE 5.6 Typical Displacement Field Obtained From STM Scans Acquired at the Same Load.

compression type. In other words, the displacement along the compression direction ($\tilde{\theta} = 99.5°$) is overestimated, while its transverse component, which should reflect the extensional Poisson effect, may actually become compressive, as can be seen in Figure 5.7. Such corrupted displacement fields are obviously not suited for the characterization of the PVC specimens responses during tensile testing. Therefore, all displacement fields exhibiting hysteresis distortion, *i.e.*, symmetric compressive patterns were disregarded in the data anlysis. However, if the displacement pattern showed significant signs of asymmetry between the u and v components, the field was retained for further analysis.

Even for the retained the displacements fields, there was no guarantee that they are noise-free. It is therefore necessary at this stage to check the anticipation that the average strains extracted from the experimental displacement fields reflect the macroscopic behavior of the PVC specimen as measured by the strain gauges. To obtain a strain mea-

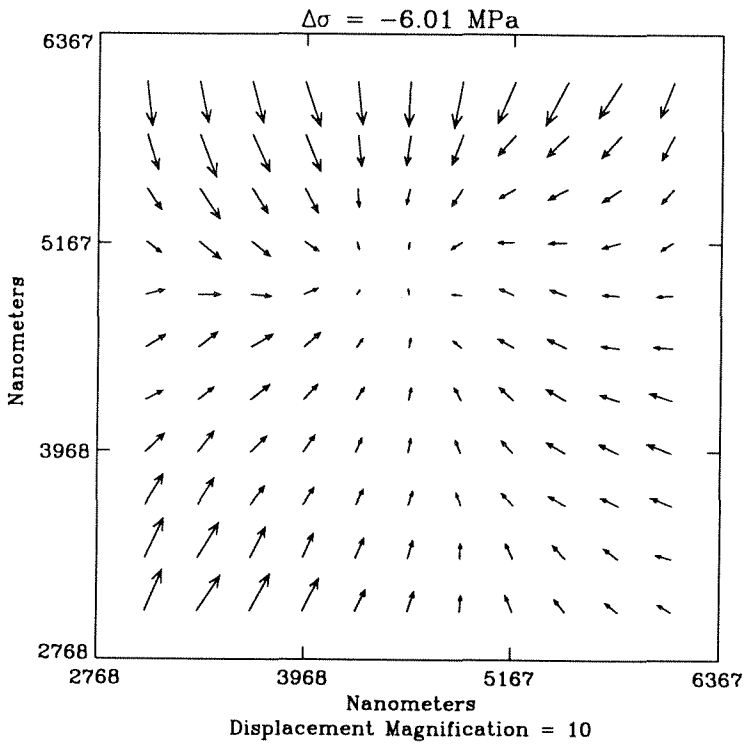

FIGURE 5.7 Hysteresis Distorted Displacement Measurement.

surement, all the scans acquired before and after a given load decrement were compared in pairs through DIC. The subsequent displacement fields were then analyzed according to the procedure outlined in section 5.1.3 and the resulting strains and principal directions were averaged. Finally, since the STM experiments involve unloading, all the strain data are relative to the highest strain to which the specimen was subjected, the absolute value of which is not known. In order to compare the STM data to the strain gauge readings, the microscope results were therefore translated along the strain axis so as to match a single STM strain measurement for each experiment to the strain gauge data. The results are shown in Figure 5.8.

The agreement between the macroscopic and average microscopic strain is surprisingly good, especially at low strain levels ($< 0.01\ m/m$). For higher strains or higher loads, the STM results tend to underestimate the strain gauge readings. This trend is con-

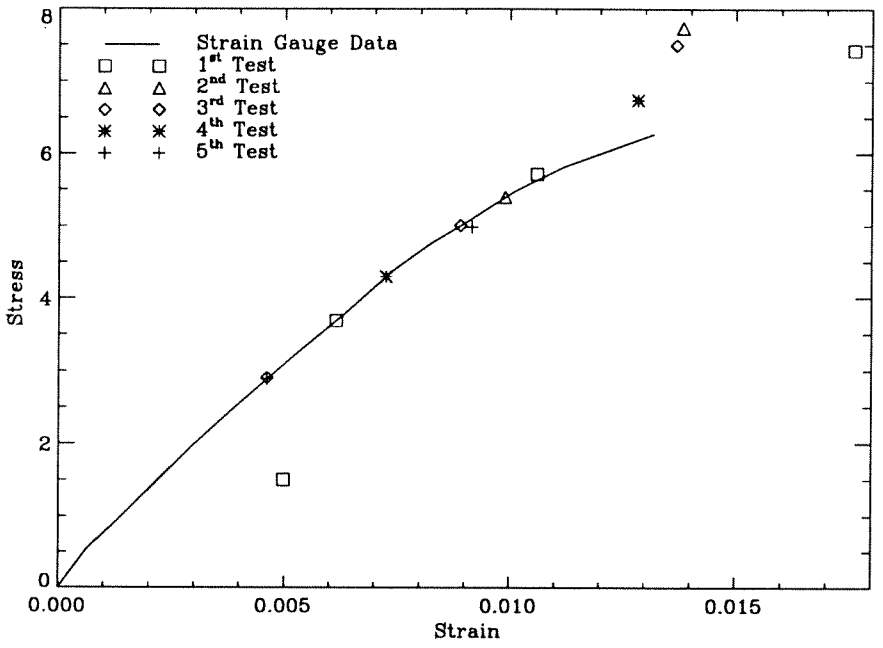

FIGURE 5.8 STM Strain Measurements Compared to Strain Gauges Results.

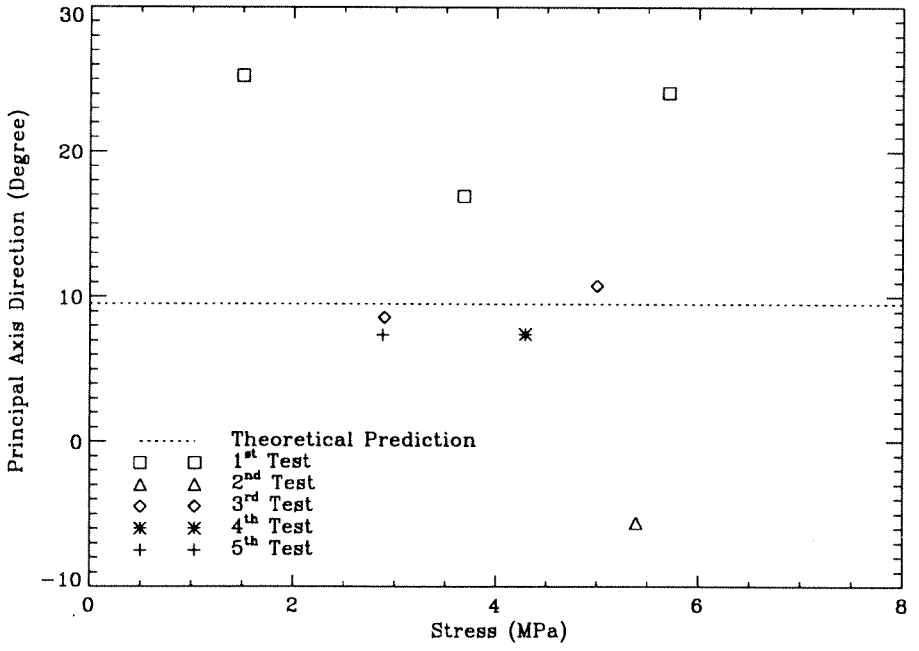

FIGURE 5.9 Experimentally Determined Direction of Principal Axis.

sistent with the "molecular model" discussed previously concerning the submicroscopic deformation mechanisms in PVC (section 5.4.1). The specimen to which the strain gauge was attached had been prestretched to only 0.008 m/m or submitted to a maximum stress level of 4.5 MPa prior to recording the strain readings to which the STM results are compared. Therefore, from 4.5 MPa onward, new polymer chain readjustment is taking place, yielding an apparently more compliant behavior than upon unloading when no such rearrangement occurs any more. It is also obvious from this comparison that among the displacement fields which were considered for this analysis, some exhibit significant spreads in their strain results. This scatter is especially pronounced when one examines the data for the principal direction presented in Figure 5.9. The principal direction should make an angle of $\theta = 9.5°$ with the Y axis. By comparison the experiments involving the largest discrepancies in strain, the principal axis direction amounts to more than 25° which provides strong indication that the latter fields are distorted.

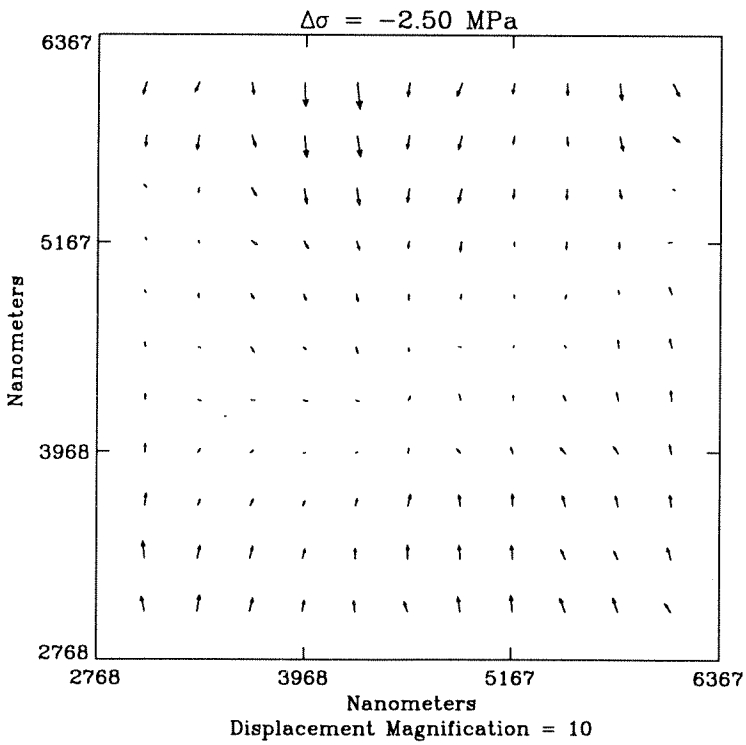

FIGURE 5.10 Measured Displacement Field of a PVC Specimen upon Unloading.

To summarize then, it appears from the nine initial tensile tests that three seem to conform in both strain and principal axis direction to the expected macroscopic behavior. Because of the inconsistency of the STM-DIC scheme in measuring the response of PVC specimens under tension, it is difficult to draw any definite conclusions from the local trends in the computed displacement fields, even for the three supposedly noise free experiments. However in none of them could any displacement inhomogeneity be readily identified. Those fields were found to be fairly smooth and very similar to the expected macroscopic response of the material, as can be seen in Figure 5.10. These results would seem to indicate that once the rearrangement of polymer chains has occurred, a continuum type constitutive model applies. This fact is also reaffirmed by the lack of any significant relative out-of-plane displacements. The specimens were indeed found to deform exclusively in the plane of their surface, their topographies remaining unchanged to within the 1.5 nm resolution of the STM-DIC scheme along the Z axis.

Conclusion

The investigation of micromechanical system responses to load excitation at the submicron scale is intended to bridge the gap between the atomistic/molecular properties of materials and their macroscopic behavior. Scanning Tunneling Microscopy is a useful tool in that regard since its resolution can range from below an angstrom to several tens of nanometers with only slight hardware modifications. The experiments performed thus far have concentrated on the $10 - 30$ nm size scale and did identified various problems associated with the use of STMs. The main source of error in acquiring surface topographies at such a small scale is part of the technology which renders these scales accessible, namely the piezoceramic tube actuator controlling the scanning motion of the microscope probe.

Although the present STM design was found flexible enough to accommodate *in-situ* tensile loading of large specimen (3 cm $\times$ 2 mm) without undue tip-specimen contacts, the hysteresis coupling between the in-plane motion of the probe and its out-of-plane measurement capabilities is difficult to control. The existence or absence of the resulting hysteresis induced distortion in scans acquired after a loading step can at this stage only be assessed *a posteriori* and therefore the consistency of the STM as a high accuracy displacement measurement tool is impaired. In all the cases where the hysteresis distortion could be avoided, that is for most of the translation tests and some of the tensile experiments, the Digital Image Correlation code, written specifically to process STM scans, has exhibited very robust convergence properties and was able to accurately compute the 3-D displacement field characterizing the specimen response to a

change in boundary loading. The roughness of the surface topographies was not found to have a direct influence on the resolution of DIC but the rougher the specimens, the less likely it is for local irregularities of the scan grid, due to the eventual and intermittent drift of the specimen under the microscope, to affect the outcome of the computations. Overall, the very good suitability of STM scans to DIC processing has demonstrated the high potential of this displacement measuring method.

Specifically, the STM-DIC scheme has proven very useful in investigating the deformation mechanism of a polymer (PolyVinylChloride) under tensile loading. Evidence was gathered which points to the limitation of the formulation of a continuum type constitutive description at the 100 nm scale (upon initial loading of a virgin specimen). Tensile tests of prestretched specimens did not exhibit inhomogeneous displacement fields at the submicron level, indicating that the polymer chains rearrangement responsible for topographic and presumably internal changes upon first loading are irreversible and therefore the reloading response is well described by the macroscopic and continuum properties of the material.

Even though the STM has already proven to be useful for investigating material systems at the micromechanical size scale, the consistency of its measurements deserves improvement. Obviously the various electronic components could be upgraded and the feedback loop correction changed to accommodate in a more efficient way the exponential dependence of the tunneling current to the gap distance. However, future refinements in the apparatus should first focus on solving the coupling problem between the in-plane and out-of-plane motion of the piezoceramic tube actuator. Actually, a new design, presented in Figure 6.1, is currently being finalized which would eliminate this major cause of scan distortion. This improved scanning system consists of not one but two piezoceramic tubes. The first, similar to that used in the present STM, will be dedicated exclusively to the scanning motion of the tip. The second tube will accommodate only the out-of-plane

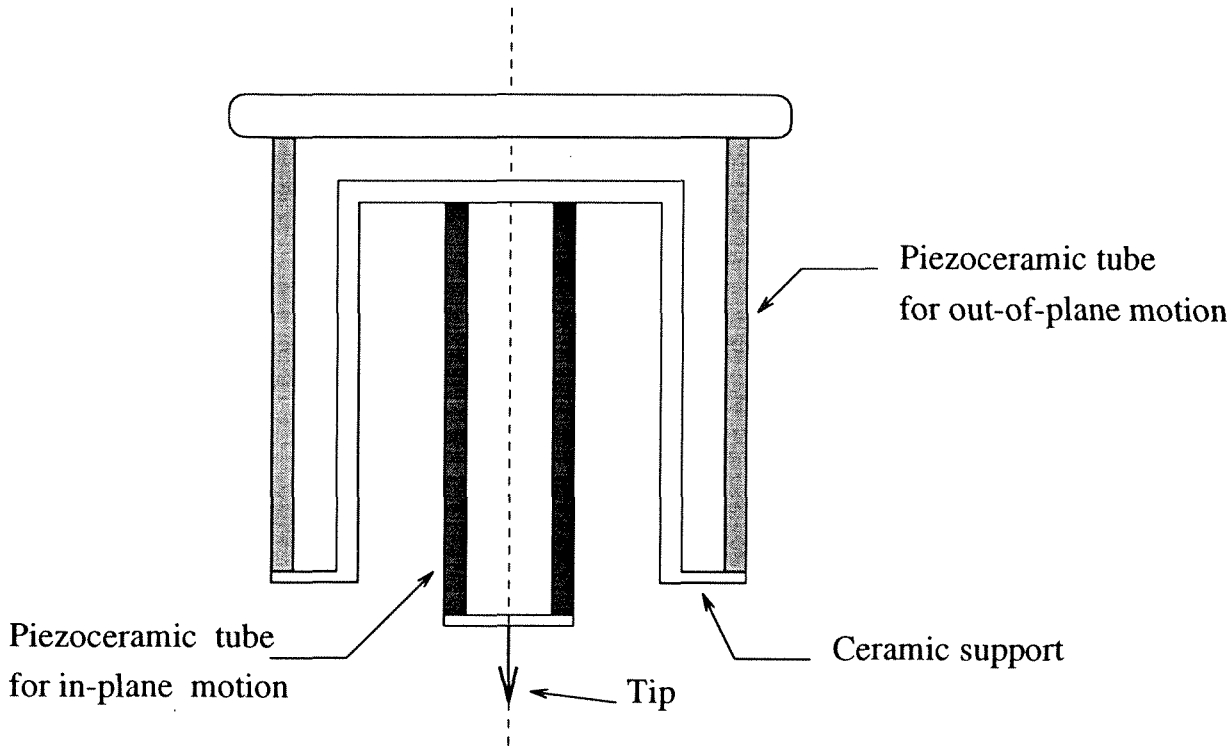

FIGURE 6.1 Schematic of a Proposed New STM Actuator.

motion of the probe.

With this new design, a wide range of micromechanical problems are be experimentally accessible such as the constitutive modeling of interphase regions in adhesive specimens or composite materials, the controversial issue of crack tip oscillations in interfacial fracture or even the direct evaluation of the time dependent characteristics of Poisson ratio in viscoelastic materials, to name a few. If some questions remain regarding the final resolution in displacement measurement of this method or the smallest size scale at which quantitative observations can be performed, it is hoped that this work will help reach the full potential of the STM-DIC scheme as a unique tool in experimental micromechanical investigations.

References

1. R.H. Fowler and L. Nordheim, Proc. R. Soc London, **A119**, 173 (1928)
2. G. Binnig, H. Rohrer, Ch. Gerber and E. Weibel, Appl. Phys. Lett., **40**, 178 (1982)
3. G. Binnig, H. Rohrer, Ch. Gerber and E. Weibel, Appl. Phys. Lett., **49**, 57 (1982)
4. G. Binnig, H. Rohrer, Ch. Gerber and E. Weibel, Physica **109/110b**, 2075, (1982)
5. J.G Simmons, J. Appl. Phys, **34**, 1973 (1963)
6. Y. Kuk and P.J. Silverman, Rev. Sci. Instrum., **60(2)**, 165 (1989)
7. G. Binnig and D.P.E. Smith, Rev Sci Instrum., **57(8)**, 1688 (1986)
8. S.-I. Park and C.F. Quate, Rev Sci Instrum., **58(11)**, 2004 (1987)
9. S.-I. Park and C.F. Quate, Rev Sci Instrum., **58(11)**, 2010 (1987)
10. D.W. Pohl, IBM J. Res. Develop., **30(4)**, 417 (1986)
11. D.P. DiLella, J.H. Wandass, R.J. Colton, C.R.K. Marrian, Rev. Sci Instrum., **60(6)**, 997 (1989)
12. G.W. Stupian and M.S. Leung, Rev. Sci. Instrum., **60(2)**, 181 (1989)
13. Guide to Modern Piezo-electric Ceramics, Vernitron Corporation (21)
14. EBL Product Line, Staveley Sensors Inc.
15. Integrated Data Book, 33, Burr Brown
16. The TTL Data Book, **2**, Texas Instrument
17. DSP56000ADS Application Development System User's Manual, Motorola
18. DSP56ADC16 Evaluation Board User's Manual, Motorola
19. Integrated Circuit Data Book, **1**, Analog Device
20. Hybrid and IC Handbook, Apex Microtechnology
21. Modules Subsystem Data Book, **2**, Analog Device
22. Data Acquisition and Control, **24**, Keithley Metrabyte.
23. Invar 36, Technical Data Sheet, Carpenter Technology Corporation
24. Micropositioning Systems, Burleigh Instrument, Inc.
25. Sensotec catalog #7000-989, Model 31, Sensotec.

26. Linear Motion System, catalog #100-1AE,model RSR12W, THK.

27. DSP56000/DSP56001 Digital Signal Processor User's Manual, Motorola

28. Diffraction Product Inc., Woodstock, IL 60098

29. D. Post, Opt. Eng. 24 pp.663-667.

30. H.V. Tippur, SM Report 89-1 CALTECH

31. W.H. Peters, W.F. Ranson, Opt. Eng. 21 (3) pp.427-431 (1982)

32. W.H. Peters, W.F. Ranson, M.A. Sutton, Opt. Eng. 22 (6) pp.738-742 (1983)

33. M.A. Sutton, W.J. Wolters, W.H. Peters, Image Vision Comput. 1 (3) pp.133-139 (1983)

34. T.C. Chu, W.F. Ranson, M.A. Sutton, Exp. Mech. Sept.85 pp.232-244

35. M.A. Sutton, M. Cheng, W.H. Peters, Image Vision Comput. 4 (3) pp.143-150 (1986)

36. M.A. Sutton, S.R. McNeil, J. Jang, Opt. Eng. 27 (10) pp.870-877 (1988)

37. H.A. Bruck, S.R. McNeil, M.A. Sutton, Exp. Mech. Sept.89 pp.261-267 (1989)

38. W.H. Peters, W.F. Ranson, J.F. Kalthoff, Journal de Physique Colloque C5 (46) pp.631-638 (1985)

39. C. Lee, W.H. Peters, Y.J. Chao, Image Vision Comput. 4 (14) pp.203 -207 (1986)

40. C. Lee, W.H Peters, M.A. Sutton, Int. Jour. Plast. 3 pp.129-142 (1987)

41. S.R. McNeil, W.H. Peters, M.A. Sutton, Eng. Fract. Mech. 28 (1) pp. 101-112 (1987)

42. M.A. Sutton, Y.J. Chao, Tappi journal March 88 pp.173-175

43. Y.J. Chao, M.A. Sutton, Tappi journal March 89 pp.58-62

44. W.H. Peters, M.A. Sutton, Exp. Mech. March 89 pp.58-62

45. Z.L. Kahn-Jetter, T.C Chu, Exp. Mech. March 90 pp.10-16 (1990)

46. M.R. James, W.L Morris, B.N. Cox, Symposium for exp. mech. in micro-mechanics ASME San Francisco Dec. 14 1989

47. M.R. James, W.L Morris, B.N. Cox, Exp. Mech. March 90 pp.60-67

48. P. Jayakumar, Ph.D thesis, Report EERL 87-01 CALTECH pp.146-149

49. G. Vendroux, Report SM 90-19, California Institute of Technology, (1990)

50. C.R. Schultheisz, Doctoral Thesis, California Institute of Technology (1991)

51. R. Pfaff, Doctoral Thesis, California Institute of Technology (1991)

52. G.U. Losi, Doctoral Thesis, California Institute of Technology, (1990)

APPENDIX A

STM Electronic Schematics

A.1 12 bit Analog-to-Digital Converter

The circuit is split into two separate parts. The converter side, presented in Figure A.1, provides the digital coding of the input signal V_{in}. The timing side, in Figure A.2, controls the conversion frequency and ensures the synchronization of the different chips. The information carried in each of the 16 output lines of the converter is presented below.

Pin 1 to Pin 12 = Most Significant to Least Significant Bit,

Pin 13 = Not Connected (NC),

Pin 14 = Transfer flag,

Pin 15-16 = Ground.

Finally the input and output ranges are as follows,

Input = $0 \; - \; 1 \; V$,

Output = $0 \; - \; 4096 \; binary$.

A.2 High Voltage Amplifier for the Z Channel

The Z channel of the piezoceramic driver is a two-stage amplifier. The gain of the second stage is hard-wired at 2, but the amplification of the first stage can be set digitally through a nine pin connector which configuration is

Pin 1 = Connected to pin 3 (EN) of AD7502,

Pin 2 = Connected to pin 16 (A0) of AD7502,

Pin 3 = Connected to pin 1 (A1) of AD7502,

Pin 4-8 = Not Connected (NC),

Pin 9 = Ground.

The coding of the gain on these three lines is presented in Table 4.

1^{st} Stage Gain	EN	A0	A1	Total Gain
1	0	0	0	2
1.56	1	0	0	3.12
2.14	1	0	1	4.28
2.66	1	1	0	5.32
3.2	1	1	1	6.4

Table 4 Gain Truth Table for the Z Channel.

The various input and output ranges are presented below.

Inputs, $V_{in} = -3,\ 3\ V$

$V_{PC} = -2.5,\ 2.5\ V$

Output, $V_{out} = -225,\ 225\ V$

A.3 High Voltage Amplifier for the X-Y Channels

Also designed as a two-stage amplifier, as depicted in Figure A.4, this device produces two equal and opposite outputs for a single input. The total gain is hardware-set at 94. The input and output ranges are defined as follows:

Inputs, $V_{in} = -2.5,\ 2.5\ V$

Output, $V_{out}^{\pm} = \mp 235,\ \pm 235\ V$

A.4 Inchworm - PC interface

Every Inchworm is connected to a dedicated controller, manufactured by Burleigh.[24]The unit provides the high voltage signals that are required by the various piezoelectric components in the actuator. Each controller can manage as many as three different Inchworms. It possesses a 25 pin port which allows for the remote controlling of every connected actuator by TTL level signals. The controller connector pinout is as follows:

1) +5 Volts
2) Ground
3) -12 Volts
4) Port OFF/ON
5) Not Connected (NC)
6) HALT/RUN Axis 1
7) Clock axis 1
8) NC
9) HALT/RUN Axis 2
10) Clock Axis 2
11) NC
12) HALT/RUN Axis 3
13) Clock Axis 3
14) +5 Volts
15) Ground
16) +12 Volts
17) NC
18) Enable Axis 1
19) FWD/REV Axis 1
20) NC
21) Enable 2
22) FWD/REV Axis 2
23) NC
24) Enable Axis 3
25) FWD/REV Axis 3

Only two pins per axis are critical in issuing commands : "FWD/REV" and "Clock." Upon one clock pulse (square wave), the Inchworm moves one step ($\approx$ 10 nm) in the direction set by the FWD/REV pin. The clock pulse rate determines the translation speed. Two different interfaces were built, one dual speed to accomodate three actuators and a multi-speed for only one Inchworm.

A.4.1 Three-Axis Dual Speed Interface

Commands are issued from the PC to the controller by a 9 pin connector the pinout of which is as follows :

1) Controller Pin 4
2) Controller pin 19
3) Controller pin 22
4) Controller pin 25
5) AD7502-1 pin 16
6) AD7502-2 pin 16
7) AD7502-2 pin 1
8) AD7502-1 pin 4
9) Ground

Speed selection is achieved through PC pin 5 (pin5 = 1, fast). Axis selection is encoded in PC pin 6 and 7 as presented in Table 5.

Axis	PC Pin 6	PC pin 7
1	1	0
2	0	1
3	1	1

Table 5 Axis Truth Table for the Inchworm Controller.

In the slow mode, 0.1 μms^{-1}, the clock pulse for each axis is provided by the PC upon depression of a specific keyboard key - see Figure A.5. In the fast mode, 100 μms^{-1}, the 555 oscillator takes over and outputs clock pulses to the controller.

A.4.2 Single Axis Multi-Speed Interface

This interface is conceptually the same as that presented above but the user may choose among four different speeds, 0.1 μms^{-1}, 5 μms^{-1}, 20 μms^{-1} and 100 μms^{-1} - see Figure A.6. The PC pinout and speed truth tables are presented below.

1) Controller Pin 4
2) Controller pin 19
6) NC
7) NC

3) CD4051 pin 11

4) CD4051 pin 10

5) 74LS74-1 pin 3

8) NC

9) Ground

Speed	PC Pin 3	PC pin 4
0.1 μms^{-1}	0	0
5 μms^{-1}	1	0
20 μms^{-1}	0	1
100 μms^{-1}	1	1

Table 6 Speed Truth Table for the Single Axis Multi-Speed Interface.

A.5 Load Cell Amplifier

Figure A.7 shows the load cell amplifier circuit. Its connected to the load cell by a 9 pin connector with the pinout arrangement

1) component 2B31 pin 12

2) Ground

3) Ground

4) component 2B31 pin 23

5) NC

6) component 2B31 pin 15

7) component 2B31 pin 18

8) component 2B31 pin 20

9) NC

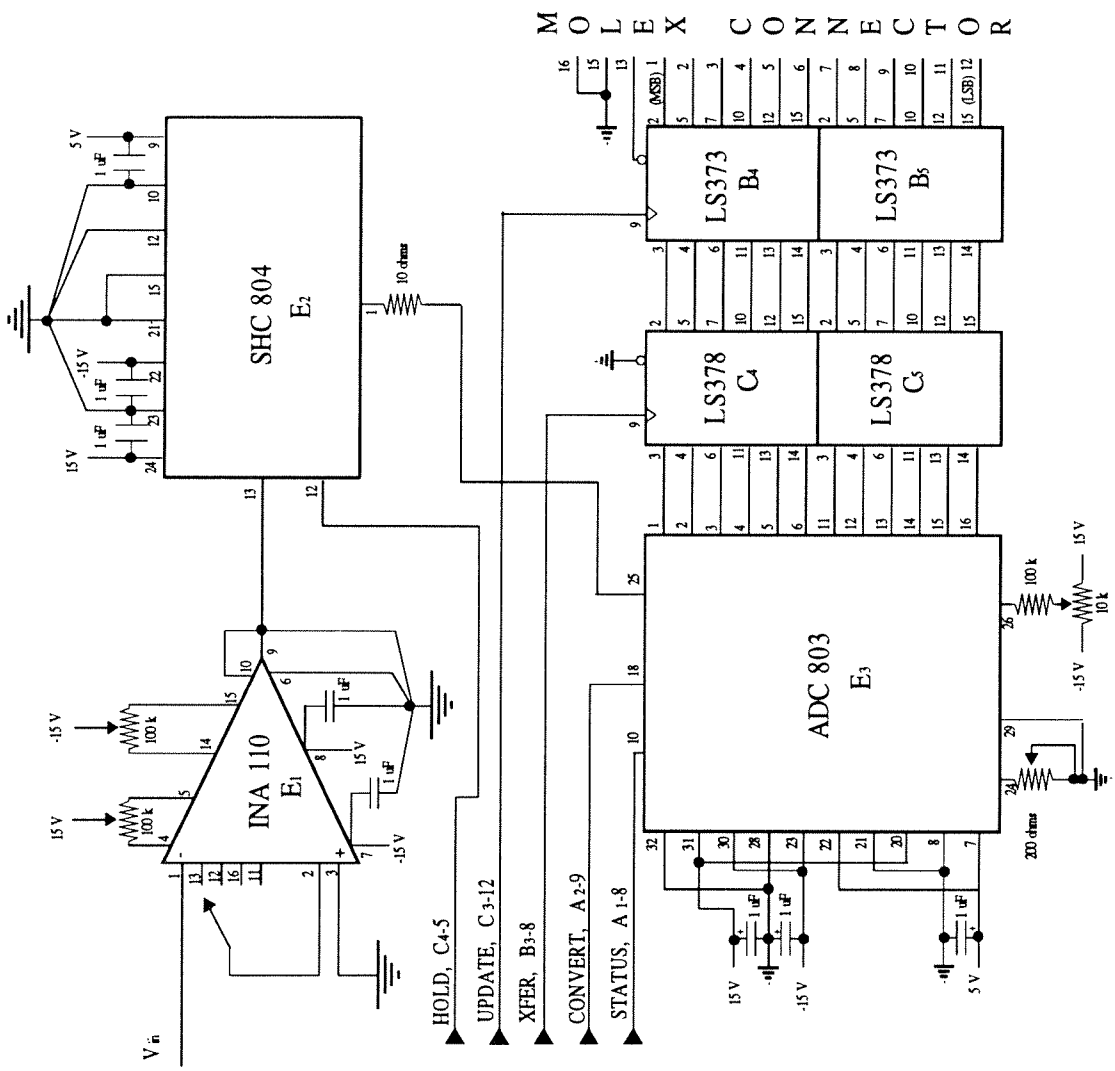

FIGURE A.1 12 bit Analog-to-Digital Converter.

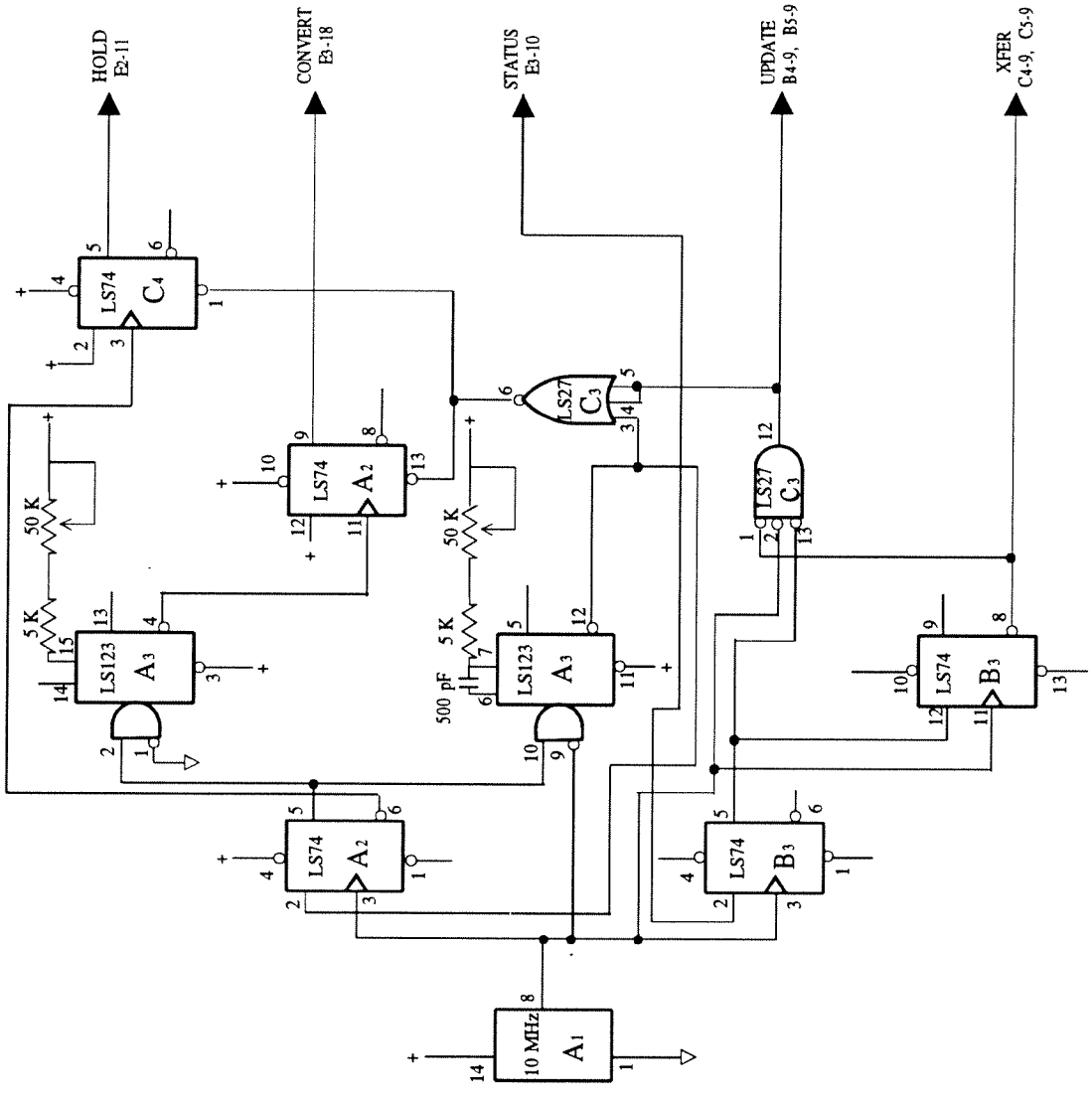

FIGURE A.2 12 bit Analog-to-Digital Converter Timing.

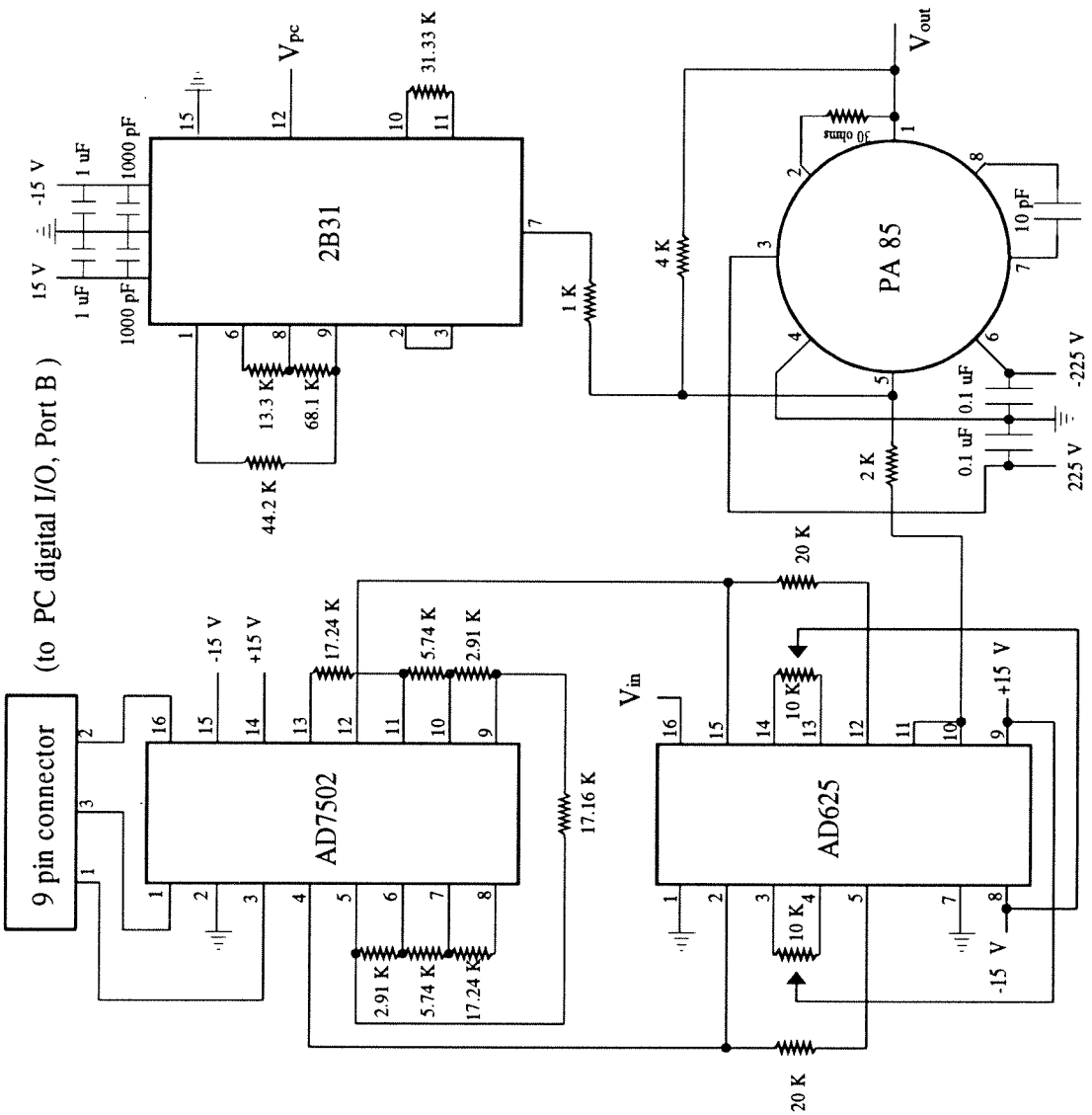

FIGURE A.3 High Voltage Amplifier for the Z Channel.

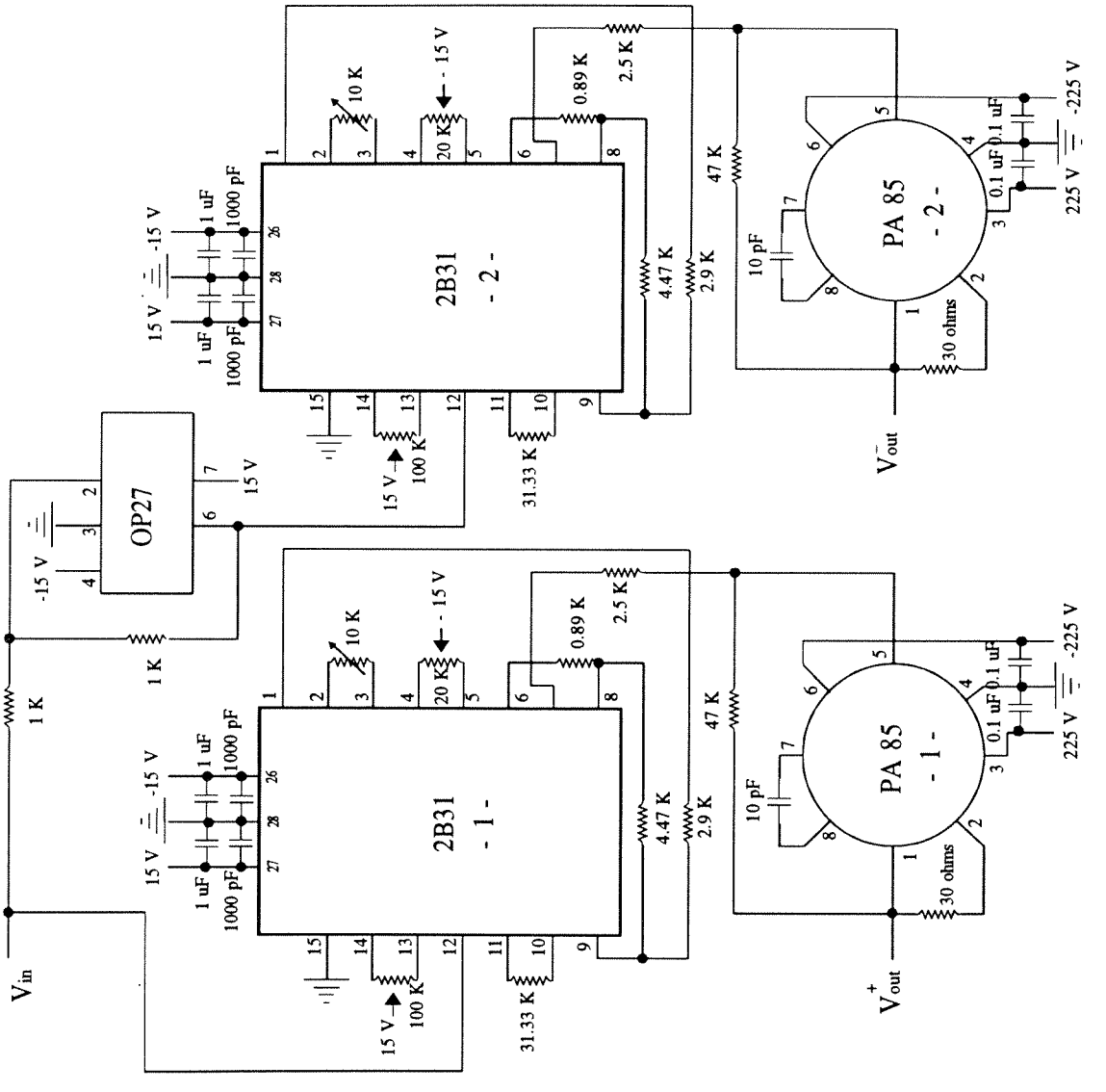

FIGURE A.4 High Voltage Amplifier for the X-Y Channels.

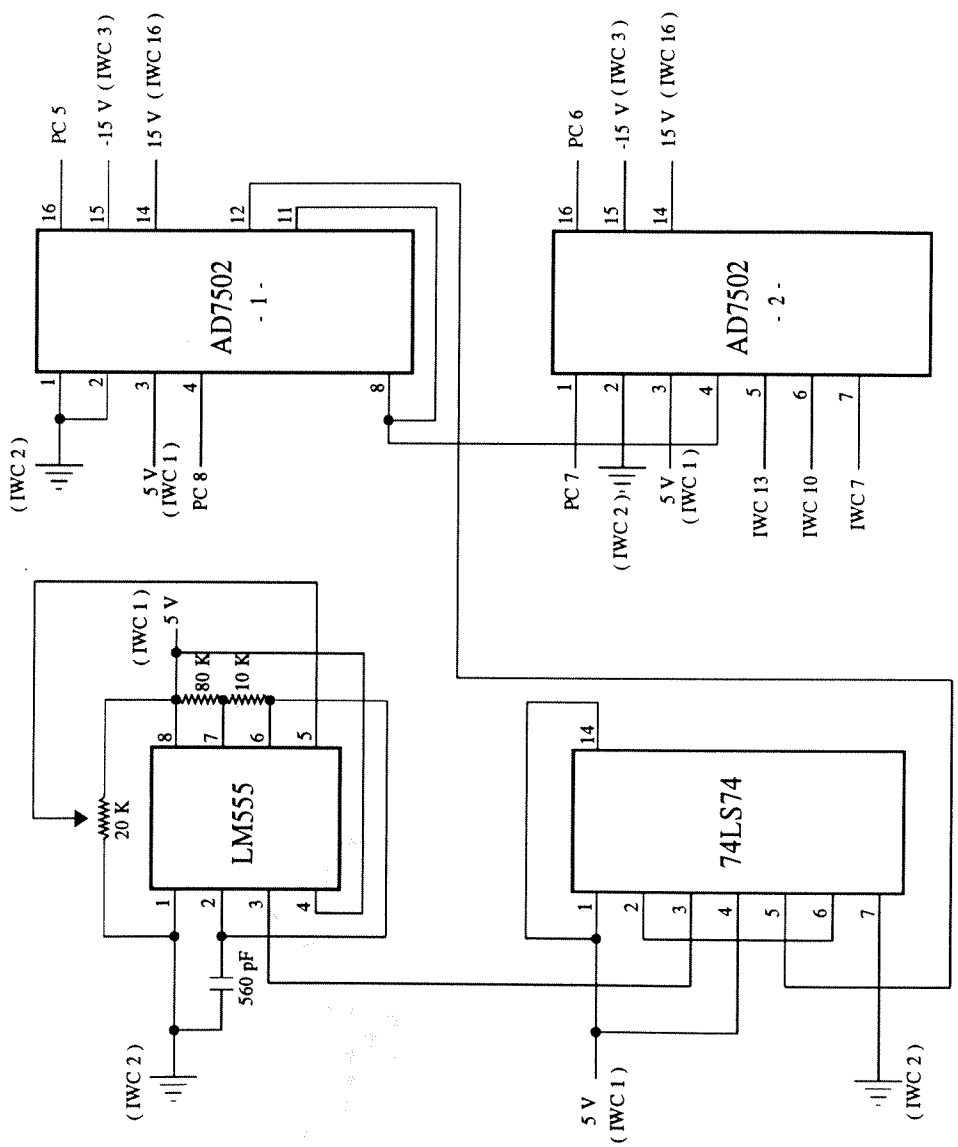

FIGURE A.5 3 Axes Dual Speed Inchworm Controller - PC Interface.

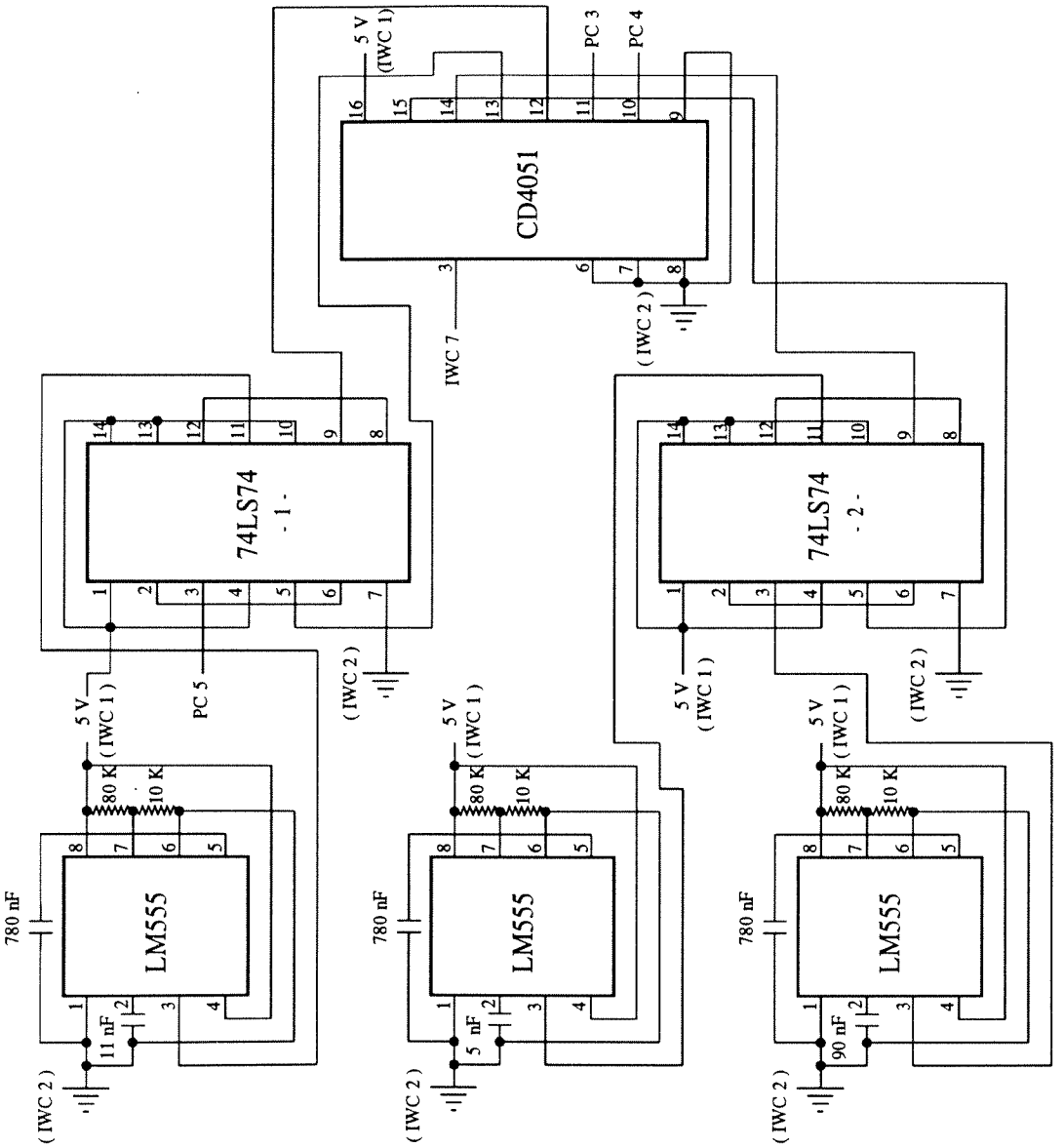

FIGURE A.6 Single Axis Multi-Speed Inchworm Controller - PC Interface.

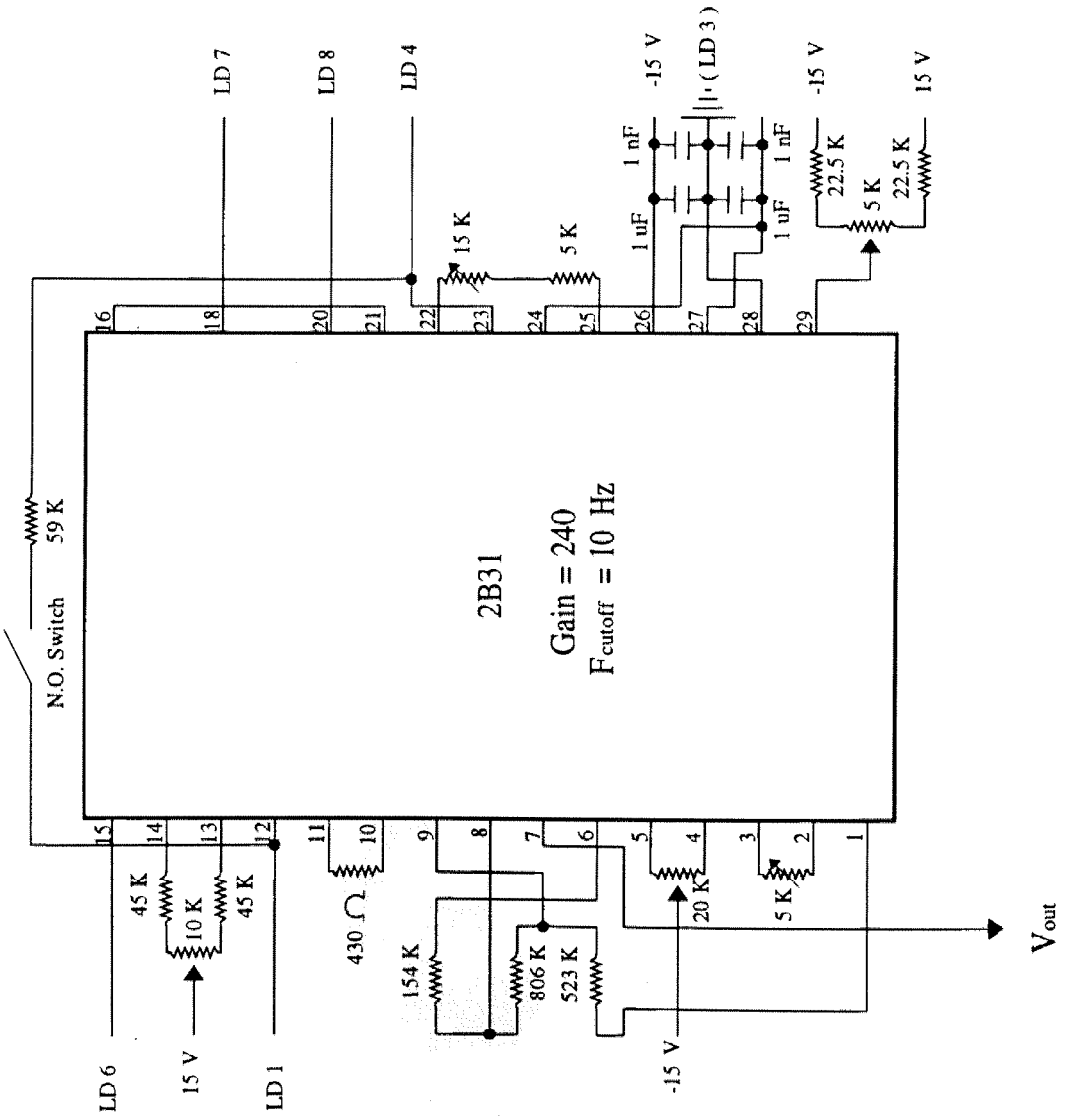

FIGURE A.7 Load Cell Amplifier.